

Modeling biological water diffusion in complex tissues

Facoltà di Scienze Matematiche, Fisiche e Naturali
Corso di Laurea Magistrale in Fisica

Candidate

Tiago Monteiro Cardoso
ID number 1670982

Thesis advisor
Prof. Silvia Capuani

Academic year 2017/2018

to Maria,

Sedes Sapientiae

Contents

Introduction	iii
1 Molecular diffusion	1
1.1 The diffusion equation	1
1.2 Solution: derivation and properties	4
1.3 Einstein's derivation: random walk	5
1.4 Anomalous diffusion and the CTRW model	7
1.4.1 Anomalous processes	7
1.4.2 The Continuous-Time Random Walk model	8
1.4.3 The fractional diffusion equation and its solution	10
2 The NMR orchestra	14
2.1 Semi-classical description	14
2.1.1 The rotating frame	14
2.1.2 Relaxation	16
2.2 Signal detection	18
2.3 NMR applied to diffusion	20
2.3.1 Spin density and k-space	20
2.3.2 Simple (Hahn) spin echo	21
2.3.3 Diffusion in the presence of a gradient	22
2.3.4 Pulsed Gradient Spin Echo	26
2.3.5 The q-space	28
2.4 Susceptibility effects	29
3 The simulation apparatus	31
3.1 The program	31
3.1.1 The Geometry block	32
3.1.2 The Random Walk block	34
3.1.3 The Signal Calculation block	36
3.2 Validation	41
4. Simulations of mono-dispersed spheres	43
4.1 The models	43
4.1.1 The mittag-Leffler	43
4.1.2 The Stretched Exponential	44
4.2 The 'big picture': first simulations and the Mittag-Leffler model	46
4.2.1 Simulation setup	46
4.2.2 Results	47
4.2.3 Discussion	51

4.3 Detailed analysis of a limited range: model comparison	53
4.3.1 Simulation setup	53
4.3.2 Mittag-Leffler results and comments	54
4.3.3 Stretched-Exponential results and comments	61
4.3.4 Conclusions and model comparison	64
5. Application: detecting demyelination of white matter tracts	67
5.1 Multiple Sclerosis	68
5.2 Model for the axons and the demyelination process	70
5.2.1 Preliminaries	70
5.2.2 Modelling axons	73
5.2.3 Modelling demyelination	76
5.3 NMR simulations and results	81
5.3.1 Simulation setup	81
5.3.2 Results	82
5.4 k-means clustering analysis	87
5.4.1 Groups of healthy and 60%-demyelinated axons: results	87
5.4.2 Groups of healthy and 30%-demyelinated axons: results	90
5.4.3 Conclusions and limitations	92
6. Conclusions	94
Bibliography	95

Introduction

You do not see much in a glass of tasteless, colorless, still water. Physicists do. Trillions of trillions of microscopic constituents - water molecules - which are permanently moving in an erratic fashion. To be more precise, they are not exactly moving, they are mostly being agitated around their initial positions. This agitation (or diffusion) was termed Brownian motion after Robert Brown, the Scottish botanist who in 1827 observed that pollen particles suspended in water move constantly in an irregular fashion. Later, in 1905, Einstein showed that this movement is due to the thermal energy of the water molecules, that makes them collide constantly and in huge quantities against the suspended particles.

Now 70% of our body is composed of water. Some of its most vital organs - like the brain - are not readily accessible to direct examination. Suppose however you could follow water molecules along the path of their movement: you would be able to watch as some molecules get entrapped inside a cavity, or some others have to contour obstacles like cells, and still others diffuse easily along the parallel "tubes" formed by neurons' axons. The paths followed by the molecules reflect the microstructure of their environment. This is the idea behind magnetic resonance diffusion imaging: to use our own body water as contrast, that is, as a non invasive means of gaining insight about microscopic tissues.

Diffusion-weighted magnetic resonance imaging (DW-MRI) is a method that relies on the measurement of the diffusion of water molecules inside a tissue. Thanks to the microscopically smallness of a molecule's path, that method is able to resolve microscopic structures to an extent unattainable by other methods like conventional magnetic resonance imaging. However we cannot track individual molecules' paths. What DW-MRI measures is the dynamical characteristics of huge ensembles. Being eminently a statistical method, it must necessarily rely on assumptions about the movement of individual molecules. Such assumptions, embodied in mathematical models, are very useful in some domains, while not in others. For instance, DW-MRI assumes that molecules follow a regular pattern of diffusion (called "Gaussian") within each imaging voxel, an assumption which, at least for the brain in general, does not hold.

This thesis has four goals: 1) the development of a Matlab program to simulate water diffusion inside different kinds of geometries and to simulate the corresponding signal acquired by nuclear magnetic resonance (NMR). As a special feature, the program includes a routine for the computation of internal magnetic gradients due to differences of magnetic susceptibility between water and surrounding tissue; 2) the simulations of systems comprising microscopic spheres of different diameters and in different packing ratios and the study of the generated NMR signal at high gradients using the framework of the Continuous Time Random Walk - CTRW; 3) a comparison of the performance of two common mathematical models used to implement the CTRW: the Mittag-Leffler and the

Stretched Exponential; and 4) the investigation of a possible application of either model to the identification of white matter demyelination.

The presentation is organized as follows. On the first chapter I review the theory of molecular diffusion, show how diffusion in complex systems, like the human brain, deviates from the classical paradigm (theory of anomalous diffusion), and explain how to cope with it using a powerful mathematical tool (the Continuous Time Random Walk model). On the second chapter I deal with the basic concepts of the theory of nuclear magnetic resonance and explain how diffusion is experimentally measured. On the third chapter I describe the Matlab program that was developed. On the fourth chapter the results for the microscopic spheres are presented. On the fifth chapter I display a second series of simulation results that suggest a possible new application for the Diffusion-weighted magnetic resonance imaging in the early diagnosis of demyelinating diseases. On the sixth chapter the results obtained in the thesis are summarized.

Chapter 1

Molecular diffusion

Dispersal is a ubiquitous phenomenon in nature and as such is the subject of sciences as diverse as physics, biology and sociology. Water molecules disperse inside test tubes; animals disperse on their natural habitats as they search for food; humans daily disperse within the big metropoles. It is important to distinguish dispersal from (coherent) movement. While an ensemble of individuals may collectively move or remain fixed in position, the individuals themselves are always oscillating around their mean positions: dispersal, being mainly due to temporal and/or local heterogeneity in the concentration of individuals, is superposed to coherent movement. Turning our attention specifically to the phenomenon of dispersion (it is what we shall henceforth call "diffusion") and to its physical characteristics, it is no surprising that the eminent measurable magnitude should be the number of individuals per unit of length, area or volume, or rather, the concentration. The concentration (or equivalently the probability to find a particle in a certain region in a certain time interval) and its variation in time and space are the magnitudes that the mathematical models quantify. Of these models the simplest is the diffusion equation. As we shall see in the following, the diffusion equation is obtained after taking the time and space macroscopic limit. Thus, it is a model that, while forcefully overlooking the microscopic details, provides us with a neat description of the system based on a probability density function. Later in this chapter we will show how the suspension of one of our assumptions - according to which the processes studied should be regarded as memoryless - will lead us to a more general class of description ("anomalous processes").

1.1 The diffusion equation

I follow closely the macroscopic derivation of the diffusion equation as proposed in (1). Since it is macroscopic, we are not dealing with single trajectories, but with ensemble properties, specifically the density. So we consider a spatial domain Ω comprising a density $\varrho(x,t)$ in a volume V . $\varrho(x,t)$ may represent the probability of finding a particle in a region of space $x + dx$ in the time

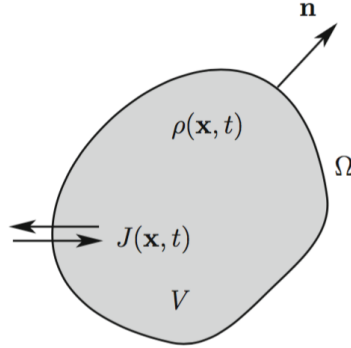


Figure 1: a volume V , delimited by boundary Ω , density $\rho(\mathbf{x}, t)$ and flux $J(\mathbf{x}, t)$ through the boundary (adapted from (1)).

interval $t + dt$ or, equivalently, it may simply represent the density of individuals, i.e., the number of individuals in the region $\mathbf{x} + d\mathbf{x}$ in the time $t + dt$. The other magnitude represented in figure 1 is the particle flux $J(\mathbf{x}, t)$, a vector representing the net flux of particles inward or outward per unit of time and per unit length. Assuming the number of particles is fixed, the rate of change of $\rho(\mathbf{x}, t)$ is solely dependent on the net flux of particles flowing through Ω . Putting it in equation form (and assuming that the density and the flux are continuous and differentiable functions of space and time), we can write:

$$\frac{\partial}{\partial t} \int_V \rho(\mathbf{x}, t) dV = - \int_{\Omega} \mathbf{J}(\mathbf{x}, t) \cdot \mathbf{n} dS , \quad (1.1)$$

S being the surface enclosing the volume V and \mathbf{n} a unit normal vector of Ω . Applying the divergence theorem to the right side of equation 1.1

$$\int_{\Omega} \mathbf{J}(\mathbf{x}, t) \cdot \mathbf{n} dS = \int_V \nabla \cdot \mathbf{J}(\mathbf{x}, t) dV , \quad (1.2)$$

we can derive

$$\int_V \left[\frac{\partial \rho(\mathbf{x}, t)}{\partial t} + \nabla \cdot \mathbf{J}(\mathbf{x}, t) \right] dV = 0 . \quad (1.3)$$

Since the integration volume is arbitrary, we can rewrite 1.3 as the continuity equation:

$$\frac{\partial \rho(\mathbf{x}, t)}{\partial t} + \nabla \cdot \mathbf{J}(\mathbf{x}, t) = 0 . \quad (1.4)$$

At this point, we could rewrite the continuity equation exclusively in terms of $\rho(\mathbf{x}, t)$ if we could ascertain the dependency of the flux $\mathbf{J}(\mathbf{x}, t)$ on the density. This functional dependency is called a "constitutive equation" and is derived from observational data or by assumption. The classical and perhaps simplest constitutive equation is known as Fick's law:

$$\mathbf{J}(\mathbf{x}, t) = -D \nabla \rho(\mathbf{x}, t) , \quad (1.5)$$

where D is the so called "diffusion coefficient". If we insert 1.5 in 1.4 and if the diffusion coefficient is independent of spatial coordinates, we obtain the diffusion equation:

$$\frac{\partial \rho(x,t)}{\partial t} = D \nabla^2 \rho(x, t) , \quad (1.6)$$

1.2 Solution: derivation and properties

For simplicity let us consider the diffusion equation in one dimension:

$$\frac{\partial \rho(x,t)}{\partial t} = D \frac{\partial^2 \rho(x,t)}{\partial x^2}. \quad (1.7)$$

If we Fourier-transform it, we get:

$$\frac{\partial \tilde{\rho}(k,t)}{\partial t} = -D k^2 \frac{\partial^2 \tilde{\rho}(k,t)}{\partial x^2}. \quad (1.8)$$

Integrating (1.8) we obtain:

$$\tilde{\rho}(k,t) = \tilde{\rho}(k,0)e^{-Dk^2t}. \quad (1.9)$$

Let us consider as the initial probability $\rho(x,0) = \delta(x-x_0)$. Inserting its Fourier-transform ($\tilde{\rho}(k,0) = \exp(-ikx_0)$) into 1.9, we obtain:

$$\rho(x,t) = \int_{-\infty}^{\infty} e^{ikx} \tilde{\rho}(k,t) dk = \int_{-\infty}^{\infty} e^{ik(x-x_0)-Dk^2t} dk = \frac{1}{\sqrt{4\pi Dt}} e^{-\frac{(x-x_0)^2}{4Dt}}. \quad (1.10)$$

$\rho(x,t)$ is called the propagator and, as we see, it assumes the form of a gaussian function. From it we can compute ordinary statistics like the mean position

$$\langle x(t) \rangle = \int_{-\infty}^{\infty} x \rho(x,t) dx = x_0 \quad (1.11)$$

and the mean square displacement (MSD):

$$\langle x^2(t) \rangle = \int_{-\infty}^{\infty} x^2 \rho(x,t) dx = x_0^2 + 2Dt. \quad (1.12)$$

The above results allow us to make two important remarks:

1) The solution of the diffusion equation (1.6) (one-dimensional and subject to initial condition $\rho(x,0) = \delta(x-x_0)$) is of the form of a Gaussian function with mean x_0 and variance $2Dt$.

2) In the large time limit, 1.12 indicates that we can expect the mean square displacement to follow the scaling

$$\langle x^2(t) \rangle \sim t \quad (1.13)$$

The above relation is an essential feature of normal (or Gaussian) diffusion processes. We will be specially interested in the study of systems - called "anomalous" - where this relation does not hold.

1.3 Einstein's derivation: random walk

The definitive explanation for brownian motion was proposed by Albert Einstein in 1905. "Brownian motion" was so named in honour of Robert Brown, the Scottish botanist who was one of the first to report the phenomenon. In 1827 he observed that small pollen grains suspended in water presented an incessant and irregular movement that could not be explained by a vegetative or animic principle (since mineral particles like coal fragments were also shown to behave similarly). Einstein was able to show that the thermal energy present in the substratum of water molecules keeps them in a state of permanent agitation. The molecules have microscopic dimensions but are orders of magnitude more numerous than the suspended particles. It is the frequent collisions of the water molecules with the suspended particles that causes the latter's observable random movement.

As we will see in the following, the beauty of Einstein's theory lies in the fact that, departing from this microscopic description, he was able to derive the diffusion equation, which, as we saw on 1.1, is a mathematical model based on a macroscopic description. He thus succeeded in joining the phenomenological description to the microscopic explanation. The aim of revisiting Einstein's work however is more than historical. For the derivation of the diffusion equation he used the conceptual framework of the random walk. This is of interest for us to the extent that it makes explicit some assumptions which are subjacent to normal diffusion. Later in this chapter we will see that a modification of the random walk approach will enable us to arrive at a generalized theory of diffusion that incorporates the so-called "anomalous" processes.

Einstein considered the motion of the water particles as composed of jumps of arbitrary length z (for simplicity let us restrict ourselves to the one-dimensional case). Each particle waits the same amount of time τ to move (it is called "waiting time" but can also be construed as the time taken for the particle to travel between two adjacent positions) and then jumps to its new position. The probability that the particle will make a jump of length z is given by a PDF $\Phi(z)$. Assuming that the jumps of all particles are identically distributed, it is clear that the density of particles located at a specific position x is equal to the density of individuals that in a time τ before were located on a point $x-z$ and made a jump of length z . Since the point of departure can have any value, m must integrate over all possible values of z :

$$\rho(x, t + \tau) = \int_{-\infty}^{\infty} \rho(x - z, t) \Phi(z) dz . \quad (1.14)$$

The equation above is a balance equation linking the densities of two points. We will now use the mathematical expedient of substituting Taylor series expansions for their expressions. However the expedient is valid only if we can consider τ and z to be infinitesimally small. In other words, we take the macroscopic limit and write:

$$\rho(x, t + \tau) = \sum_{n=0}^{\infty} \frac{t^n}{n!} \frac{\partial^n \rho}{\partial t^n} \quad (1.15)$$

and

$$\rho(x - z, t) = \sum_{n=0}^{\infty} \frac{(-z)^n}{n!} \frac{\partial^n \rho}{\partial x^n} \quad (1.16)$$

Rewriting 1.14 with 1.15 and 1.16, we obtain:

$$\rho(x, t) + \tau \frac{\partial \rho(x, t)}{\partial t} + \dots = \rho(x, t) \int_{-\infty}^{\infty} \Phi(z) dz - \frac{\partial \rho(x, t)}{\partial x} \int_{-\infty}^{\infty} z \Phi(z) dz + \frac{\partial^2 \rho(x, t)}{\partial x^2} \int_{-\infty}^{\infty} \frac{z^2}{2!} \Phi(z) dz + \dots \quad (1.17)$$

Since $\Phi(z)$ is a pdf, it must be normalized, that is, $\int_{-\infty}^{\infty} \Phi(z) dz = 1$. Moreover, the isotropy condition imposes that $\Phi(z) = \Phi(-z)$. For that reason, $\int_{-\infty}^{\infty} z^n \Phi(z) dz = 0$ whenever n is odd. With that in mind we can rewrite 1.17 to get:

$$\rho(x, t) + \tau \frac{\partial \rho(x, t)}{\partial t} + O(t^2) = \rho(x, t) + \frac{\partial^2 \rho(x, t)}{\partial x^2} \int_{-\infty}^{\infty} \frac{z^2}{2} \Phi(z) dz + O(z^4). \quad (1.18)$$

And after dividing by τ :

$$\frac{\partial \rho(x, t)}{\partial t} = \frac{\partial^2 \rho(x, t)}{\partial x^2} \int_{-\infty}^{\infty} \frac{z^2}{2\tau} \Phi(z) dz + O(z^4/\tau). \quad (1.19)$$

As the final step, we take the macroscopic limit $z \rightarrow 0$ and $\tau \rightarrow 0$ but do so in a way that z^2/τ remains finite:

$$\frac{\partial \rho(x, t)}{\partial t} = D \frac{\partial^2 \rho(x, t)}{\partial x^2}, \quad (1.20)$$

which is the well-known diffusion equation with

$$D = \frac{1}{2\tau} \int_{-\infty}^{\infty} z^2 \Phi(z) dz = \frac{\langle z^2 \rangle}{2\tau}. \quad (1.21)$$

The above derivation underlines two important facts which otherwise could have been overlooked:

1) In 1.21 $\langle z^2 \rangle$ is the second moment of the jump length PDF $\Phi(z)$. We have obtained the diffusion equation (1.20) independently of the form of $\Phi(z)$. This means we need not assume that the jump lengths are Gaussian distributed: in the macroscopic limit the diffusion approximation is valid as long as the second moment of $\Phi(z)$ exists and the diffusion coefficient D is well-defined.

2) The macroscopic limit involves a loss of information whereby a non-local equation (1.14, connecting two different points) is transformed in the local equation 1.20, with the implication that any eventual memory effects are necessarily removed.

1.4 Anomalous diffusion and the CTRW model

According to Metzler and Klafter (2), "the stochastic formulation of transport phenomena in terms of a random walk process, as well as the description through the deterministic diffusion equation are the two fundamental concepts in the theory of both normal and anomalous diffusion." The random walk framework, as we have just seen, provides a neat link between microscopic description and macroscopic mathematical model. Moreover, it sheds light over some of the assumptions we make in order to derive the diffusion equation. The diffusion equation, by its turn, has become such an ubiquitous model due to the fact that a wide variety of transport processes can be described by a Gaussian distribution. Here in this section we shall see that there are some processes which do not follow a statistics determined by the normal distribution (called for that reason "anomalous"). Thus we shall have to look for a more general diffusion equation - a result that will be readily obtained by a generalization of the random walk framework.

1.4.1 Anomalous processes

As we saw above (section 1.2), if a system of diffusing particles is governed by the diffusion equation, then we can expect their mean square displacement - MSD to depend linearly on time in the asymptotic limit ($\langle x^2(t) \rangle \sim t$). This scaling law is a commonly observable phenomenon and a direct result of the Central Limit Theorem - CLT: the total displacement made by a particle executing a trajectory composed of an elevated number n of independent displacements will approximate a Gaussian distribution of the type e^{-x^2/σ^2} , where σ , according to the theorem, is proportional to n . Since n , by its turn, is proportional to time, we have (assuming a Gaussian distribution with zero mean): $\sigma = \langle x^2(t) \rangle \sim t$.

Thanks to the CLT, we do not need to assume that the displacements are Gaussian distributed in order to obtain a Gaussian distributed total displacement. This fact was highlighted by the derivation of the diffusion equation in the last section. This explains why the diffusion equation is so useful to model diffusion processes and why the time-linear scaling relation is so pervasive in nature.

However, the CLT is validly applicable only if the diffusion process obey three conditions:

- 1) The displacements composing the trajectory must be independent, i.e., the process is memoryless.

- 2) The displacements have the same PDF, i.e., the process is stationary.
- 3) The PDF of the individual displacements has finite mean and variance.

It is already well known that many processes in nature violate one or more of the above conditions. In those cases the mean square displacement in the limit $t \rightarrow \infty$ no longer depends linearly on time. We call "anomalous" the diffusion processes that display the scaling $\langle x^2(t) \rangle \sim t^\nu$, and particularly "subdiffusive processes" those for which $\nu < 1$ and "superdiffusive processes" those for which $\nu > 1$.

1.4.2 The Continuous-Time Random Walk model

We are especially interested in the third condition above. According to the Generalized Central Limit Theorem - GCLT, proposed by Paul Lévy, if conditions 1 and 2 hold, that is, the random variables (i.e. the n individual displacements) are independent and identically distributed, then the process composed of the sum of those random variables (i.e. the total displacement) tends to a Lévy distribution in the limit $t \rightarrow \infty$. The Lévy distributions, which are a more general class of stable distributions - the Gaussian being recovered in the special case in which the random variables have finite mean and variance - decay asymptotically like $x^{-(1+\nu)}$. Since the MSD diverges for $\nu < 2$, this poses a problem, for arbitrarily large displacements will be allowed with arbitrarily high frequencies. In order to apply the generalized version of the CLT to real physical systems, in which a larger displacement usually implies that the particle spends more time between the successive positions, we will also generalize our model: in the Continuous-Time Random Walks model - CTRW not only the jump length of each move of the particle is treated as a random variable, but also the waiting time necessary to perform it too. Here I follow closely the derivation of the model presented by Méndez et al. (1).

If a random walker starts at position $X_0 = 0$ and jumps n times (each with length Z_n), then, after n jumps, its position will be:

$$X_n = \sum_{j=1}^n Z_j. \quad (1.22)$$

Let us assume the variables $\{Z_j\}$ are independent and follow the same PDF, $\Phi(z)$. We can write that, for any step n and position x ,

$$\rho_n(x) = \int \rho_{n-1}(x - z)\Phi(z)dz. \quad (1.23)$$

The former equation can be written as a spatial convolution:

$$\rho_n = \rho_0 * \Phi * \dots (\text{n times}) \dots * \Phi. \quad (1.24)$$

Let us consider for simplicity the one-dimensional case. Since $z \in \mathbb{R}$ and thanks to the spatial convolution theorem, we can use the Fourier transform of (1.24) to get:

$$\rho_n(k) = \rho_0(k) \Phi(k)^n. \quad (1.25)$$

Turning our attention now to the waiting times, we depart from their PDF, $\varphi(t)$, and try to determine the probability that a particle jumps n times during a time t . First, we can write the probability that no jump has occurred up to time $t - \phi(t)$ - as a function of the waiting time PDF:

$$\phi(t) = \int_t^\infty \varphi(u) du = 1 - \int_0^t \varphi(u) du. \quad (1.26)$$

If $P_n(t)$ is the probability that n jumps be performed in time t , then $P_0(t) = \phi(t)$. The probability that there is a first jump at time u and no further jumps up to time t is $\varphi(u)\phi(t-u)$. If we integrate over u , we get:

$$P_1(t) = \int_0^t \varphi(u)\phi(t-u) du = \phi^*\varphi, \quad (1.27)$$

the asterisk now standing for time convolution. By induction, we have for n jumps:

$$P_n(t) = \phi^* \varphi^* \dots (\text{n times}) \dots^* \varphi. \quad (1.28)$$

Using the Laplace transform of 1.26 and 1.28, and applying the time convolution theorem, we get:

$$P_n(s) = \phi(s) \varphi(s)^n = \varphi(s)^n \frac{1-\varphi(s)}{s}. \quad (1.29)$$

The results obtained thus far depend on the number of steps n . We must reformulate them in terms of the time t . Let $N(t)$ be the number of steps taken. Then we can rewrite 1.22 to indicate $X(t)$, the position of a particle at time t :

$$X(t) = \sum_{j=1}^{N(t)} Z_j. \quad (1.30)$$

If $Q_n(x)$ is the density of particles able to reach the point x in n jumps, the density of particles located at position x at time t - $Q(x,t)$ - will be the expected value of $Q_n(x)$ over all possible values of n :

$$Q(x,t) = \sum_{n=0}^{\infty} \rho_n(x) P_n(t). \quad (1.31)$$

Using 1.25 and 1.29, and taking the Fourier-Laplace transform of 1.31, we get:

$$Q(k,s) = \sum_{n=0}^{\infty} \rho_n(k) P_n(s) = Q(k,0) \frac{1-\varphi(s)}{s} \sum_{n=0}^{\infty} [\Phi(k)\varphi(s)]^n : \quad (1.32)$$

$$Q(k,s) = Q(k,0) \frac{1-\varphi(s)}{s} \frac{1}{1-\Phi(k)\varphi(s)}. \quad (1.33)$$

1.33 is known as the Montroll-Weiss equation and is valid only if the waiting times and the jump lengths are independent variables. Otherwise, we would have to make use of a joint PDF, that a particle makes a displacement of x after a waiting time $t - \Psi(x,t)$. From the joint PDF, $\Phi(x)$ and $\varphi(t)$ could be obtained after integration over the other variable:

$$\Phi(x) = \int_0^\infty \Psi(x,t) dt, \quad \varphi(t) = \int_{-\infty}^\infty \Psi(x,t) dx, \quad (1.34)$$

and the Montroll-Weiss equation would read:

$$Q(k,s) = Q(k,0) \frac{1-\varphi(s)}{s} \frac{1}{1-\Psi(k,s)}. \quad (1.35)$$

1.4.3 The fractional diffusion equation and its solution

We seek to study the Montroll-Weiss equation in the asymptotical limit and when either large waiting times or jump lengths or both of them are allowed.

a) Large waiting times

We consider a symmetric jump length distribution with finite variance. The waiting time PDF has a divergent first moment and behaves like a power law in the asymptotic limit of large times:

$$\varphi(t) \simeq \frac{\alpha}{\Gamma(1-\alpha)} \frac{\tau^\alpha}{t^{1+\alpha}} \text{ as } t \rightarrow \infty \quad (0 < \alpha < 1). \quad (1.36)$$

Its Laplace transform, thanks to the Tauberian theorems, can be written in the form $\varphi(s) \simeq 1 - (\tau s)^\alpha$ as $s \rightarrow 0$. If we use this result along with the expression for the Fourier transform of the jump length PDF ($\Phi(k) \simeq 1 - \langle x^2 \rangle k^2 / 2$) along with the Montroll-Weiss equation (1.33) written in the form

$$\frac{1-\varphi(s)}{s\varphi(s)} [sQ(k,s) - Q(k,0)] = [\Phi(k) - 1] Q(k,s), \quad (1.37)$$

and disregard terms of higher order than s^α and k^2 , we get:

$$\tau^\alpha [s^\alpha Q(k,s) - s^{\alpha-1} Q(k,0)] = -\frac{\langle x^2 \rangle k^2}{2} Q(k,s). \quad (1.38)$$

Now if we define a generalized diffusion coefficient in the form $D_\alpha = \langle x^2 \rangle / 2\tau^\alpha$ and make use of the Caputo fractional derivative, defined as

$$\frac{\partial^\alpha \rho(x,t)}{\partial t^\alpha} = \frac{1}{\Gamma(1-\alpha)} \frac{\partial}{\partial t} \int_0^t \frac{\rho(x,u)}{(t-u)^\alpha} du, \quad (1.39)$$

and whose Laplace transform is

$$\mathcal{L}[\partial^\alpha \rho(x, t) / \partial t^\alpha] = s^\alpha \varrho(x, s) - s^{\alpha-1} \varrho(x, 0), \quad (1.40)$$

we can Fourier-Laplace invert 1.38 and find a diffusion equation of fractional kind:

$$\frac{\partial^\alpha \rho}{\partial t^\alpha} = D_\alpha \frac{\partial^2 \rho}{\partial x^2}. \quad (1.41)$$

If we compute the MSD via the relation

$$\langle x^2(s) \rangle = \int_{-\infty}^{\infty} x^2 \rho(x, s) dx = - \left[\frac{d^2 \rho(k, s)}{dk^2} \right]_{k=0}, \quad (1.42)$$

using 1.33, we get:

$$\langle x^2(s) \rangle \simeq \frac{1}{\tau^\alpha s^{\alpha+1}} \langle x^2 \rangle, \quad (1.43)$$

which after Laplace-inversion yields:

$$\langle x^2(t) \rangle \sim t^\alpha. \quad (1.44)$$

Since $0 < \alpha < 1$, the MSD grows sublinearly with time. We can conclude that a system described by a symmetric jump length distribution, with finite moments, and a waiting time PDF with divergent first moment can be macroscopically modelled by a diffusion equation with fractional time derivative (1.41) and displays anomalous behavior of the subdiffusive type.

b) Large distance jumps

This time we consider a jump length distribution with divergent variance. Let us model it in the macroscopic limit ($k \rightarrow 0$) as a Lévy distribution:

$$\Phi(k) = \exp(-a |k|^\mu) \simeq 1 - a |k|^\mu, \text{ with } 0 < \mu < 2. \quad (1.45)$$

The waiting time PDF has finite moments:

$$\varphi(s) \simeq 1 - \langle t \rangle s \text{ (in the macroscopic limit, i.e., } s \rightarrow 0). \quad (1.46)$$

Inserting 1.45 and 1.46 into 1.33, rearranging terms, and disregarding terms of higher order than $|k|^\mu$ and s , we obtain:

$$\langle t \rangle [s \varphi(k, s) - \varphi(k, 0)] = -a |k|^\mu \varphi(k, s). \quad (1.47)$$

If we use the definition of the Riesz derivative,

$$\frac{\partial^\mu \rho(x,t)}{\partial |x|^\mu} = \frac{\Gamma(1+\mu)}{\pi} \sin\left(\frac{\mu\pi}{2}\right) \int_0^\infty [\rho(x-z,t) - 2\rho(x,t) + \rho(x+z,t)] z^{-1-\mu} dz, \quad (1.48)$$

and define a generalized diffusion coefficient as $D = a/\langle t \rangle$, we can Fourier-Laplace invert 1.47 to find:

$$\frac{\partial \rho(x,t)}{\partial t} = D \frac{\partial^\mu \rho(x,t)}{\partial |x|^\mu}. \quad (1.49)$$

Again, we can compute the MSD. It can be demonstrated (2) that, after the calculation of the fractional moments and its proper rescaling, we are able to define a pseudo mean square displacement

$$[x^2] \propto t^{2/\mu}, \quad (1.50)$$

which grows superlinearly with time, since $0 < \mu < 2$. We can conclude that a system described by a jump length distribution with divergent variance and a waiting time PDF with finite moments can be macroscopically modelled by a diffusion equation with fractional space derivative (1.49) and displays anomalous behavior of the superdiffusive type.

c) General case

In the general case - in which eventually both the jump length variance and the characteristic waiting time follow asymptotic power law distributions - the system can be described by a fractional diffusion equation in the form (3):

$$\frac{\partial^\alpha \rho}{\partial t^\alpha} = D_{\alpha,\mu} \frac{\partial^\mu \rho(x,t)}{\partial |x|^\mu}, \quad (1.51)$$

where a Caputo fractional time derivative (when $0 < \alpha < 1$) and a Reisz fractional space derivative (when $0 < \mu < 2$) are to be intended. In the case $\alpha \geq 1$ or $\mu \geq 2$, we have integer time or space derivatives with order 1 or 2, respectively. In the case $\alpha \geq 1$ and $\mu \geq 2$, we regain the classical equation (1.7) and diffusion is normal. The solution of 1.51 can be given in the form of the Fox's H function and its characteristic function, which will be especially useful in the course of this work, is (3):

$$\rho(k,t) = E_\alpha(-D_{\alpha,\mu}|k|^\mu t^\alpha), \quad (1.52)$$

where E_α is the single-parameter Mittag-Leffler function - MLF, defined as:

$$E_\alpha(z) = \sum_{i=1}^{\infty} \frac{(z)^i}{\Gamma(\alpha i + 1)}, \quad (1.53)$$

and $\Gamma(\cdot)$ stands for the gamma function.

It can be demonstrated (2) that a MSD can be defined - called the pseudo or imaginary mean square displacement - and that it displays a behavior dependent on the ratio α/μ :

$$[x^2] \propto t^{2\alpha/\mu}. \quad (1.54)$$

If either of the two conditions $0 < \alpha < 1$ or $0 < \mu < 2$ holds (not both), then we can state that if $2\alpha/\mu < 1$, the process is subdiffusive; if $2\alpha/\mu > 1$, the process is superdiffusive; and if $2\alpha/\mu = 1$, normal diffusion takes place. If both conditions hold, the process is a non-Markovian Lévy flight; if neither holds, we have again normal diffusion (2).

Chapter 2

The NMR orchestra

Nuclear Magnetic Resonance - NMR has a paramount importance in studies of molecular diffusion due to its non-destructive - it does not use any ionizing radiation - and its non-invasive characters - this second characteristic making it specially useful for medical applications.

Diffusion-Weighted Nuclear Magnetic Resonance - DW-NMR, in particular, is a method that adds a pair of dephasing/rephasing gradients to a Spin Echo - SE sequence, thus using the phase of transverse magnetization to "label" water molecules. The resultant signal produced by the transverse magnetization oscillation of an ensemble of molecules becomes in this way sensitized to diffusion ("diffusion-weighted"), since the loss of signal intensity due to imperfect rephasing enables us to measure the amount of diffusion (4).

In the following we will review the mathematical fundamentals of NMR along with the basics of signal detection and analysis. Also, we will describe how the applied magnetic field may be subject to artefacts produced by susceptibility differences present in heterogeneous media - the so-called internal gradients.

2.1 Semi-classical description

2.1.1 The rotating frame

The NMR signal is dominated by the hydrogen nuclei of water (^1H). Since they are 1/2-spin particles, each one constitutes a magnetic dipole $\vec{\mu}$. Moreover each spin is subject to an angular moment which is proportional to $\vec{\mu}/\gamma$, where γ is the gyromagnetic ratio ($\gamma = 267.513 \cdot 10^6 \text{ rad s}^{-1} \text{ T}^{-1}$). The application of a static magnetic field - \vec{B}_0 - will produce a torque $\vec{\tau}$ aiming to align the spins' moments with the field:

$$\vec{\tau} = \vec{\mu} \times \vec{B}_0. \quad (2.1)$$

As a result, the spins precess around \vec{B}_0 at a frequency proportional to the field magnitude. This is known as Larmor Frequency (ω_0) and has the value

$$\omega_0 = \gamma B_0, \quad (2.2)$$

The component of the magnetic dipole in the direction of \vec{B}_0 can be either parallel or anti-parallel to the field. In quantistic terms, these correspond to two stable energy states, the one with lesser, the other with higher energy - respectively the states with quantum numbers $s = +1/2$ and $s = -1/2$. Due to the population discrepancy between the two states - the one less energetic being the most populated - the vectorial sum of all the magnetic dipoles produces a non-zero resultant vector called the magnetization - \vec{M} . The rate of change of the angular momentum (\vec{M}/γ) equals the torque:

$$\frac{d\vec{M}}{dt} = \gamma \vec{M} \times \vec{B}, \quad (2.3)$$

whose solution, considering $|\vec{B}| = B_0$, corresponds to a precession of the magnetization around the field axis at the Larmor frequency ω_0 .

Now one of the most powerful tools of NMR concerns the use of a frame of reference that rotates about the main field \vec{B}_0 at resonance. Consider that the field \vec{B}_0 is oriented along the axis z:

$$\vec{B}_0 = B_0 \hat{k}, \quad (2.4)$$

and that we apply a second, transverse (i.e., oriented on the xy-plane), field \vec{B}_1 which oscillates at the rate ω_0 . The circularly polarized component of the transverse field can be written:

$$\vec{B}_1 = B_1 \cos(\omega_0 t) \hat{i} - B_1 \sin(\omega_0 t) \hat{j}, \quad (2.5)$$

\hat{i} , \hat{j} and \hat{k} being unit vectors in the directions x, y and z, respectively. Considering this equation, the initial condition $\vec{M}(t) = M_0 \hat{k}$ and the frequency of the oscillating transverse field $\omega_1 = \gamma B_1$, the solution of 2.3 is:

$$M_x = M_0 \sin(\omega_1 t) \sin(\omega_0 t)$$

$$M_x = M_0 \sin(\omega_1 t) \cos(\omega_0 t)$$

$$M_x = M_0 \cos(\omega_1 t). \quad (2.6)$$

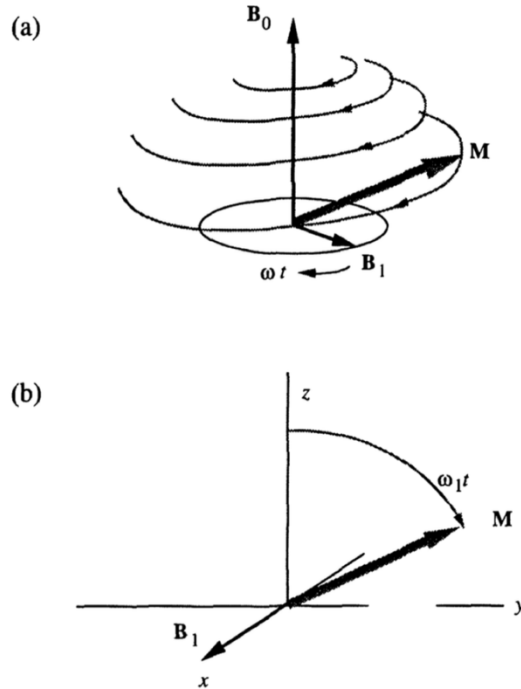


Figure 2: (a) Evolution of the magnetization vector in the laboratory frame. \vec{B}_0 is the main field and \vec{B}_1 is the transverse, rotating, field. Upon resonant condition ($\omega = \omega_0$), the magnetization simultaneously precesses about \vec{B}_0 at ω_0 and about \vec{B}_1 at ω_1 . (b) The view from the rotating frame: upon resonant condition, the effective field on the longitudinal direction is zero and there is only a precession about the now stationary field \vec{B}_1 (reproduced from 5).

Equation 2.6 means that, when we apply an oscillating field at the resonant frequency ω_0 , the magnetization simultaneously precesses about the main field B_0 at ω_0 and about the radio-frequency field B_1 at ω_1 (figure 2). As a result, in the rotating frame, the spin is simply precessing about B_1 .

2.1.2 Relaxation

We call spin-lattice or longitudinal relaxation the process by which the spin system recovers the thermal equilibrium state that had been disturbed by the resonant radio-frequency pulse. The equilibrium is characterized by a magnetization vector \vec{M}_0 directed along the main (longitudinal) field \vec{B}_0 and the relaxation process depends on the exchange of energy between the spin system and the surrounding thermal reservoir (the "lattice"). We can describe the process by the equation:

$$\frac{dM_z}{dt} = -(M_z - M_0)/T_1 , \quad (2.7)$$

with solution

$$M_z(t) = M_z(0) \exp(-t/T_1) + M_0 (1 - \exp(-t/T_1)) , \quad (2.8)$$

where T_1 is known as the spin-lattice relaxation time.

The relaxation of the transverse magnetization, on its turn, is governed by another constant, T_2 , the spin-spin relaxation time. As the name indicates, by this process the spins come to thermal equilibrium among themselves. Once the radio-frequency impulse is turned off, the nuclear spins no longer receive energy and therefore tend to return to their equilibrium state. The transversal magnetization due to the spin-spin relaxation T_2 decays to zero as the magnetization reconstitutes along the direction of the magnetic field with a time T_1 . Due to the fact that transverse relaxation may also come across via interaction with the lattice, but depends fundamentally on direct interaction among the spins, $T_2 \leq T_1$. While at room temperature T_1 is normally in the range 0.1 to 10 seconds, T_2 values are usually between 10 μ s to 10 s.

In the case of weak terms of interaction, a situation assumed by the Bloembergen, Purcell and Pound theory - BPP, transverse relaxation can be described by the phenomenological equation:

$$\frac{dM_{x,y}}{dt} = \frac{-M_{x,y}}{T_2}, \quad (2.9)$$

whose solution reads:

$$M_{x,y}(t) = M_{x,y}(0) \exp(-t/T_2). \quad (2.10)$$

Since many NMR applications deal with slowly relaxing spins residing in liquid state molecules, the phenomenological approach (equation 2.9) in those cases is entirely acceptable. From equations 2.3, 2.7 and 2.9 in the rotating frame, one is able to deduce a fundamental set of equations for the description of many relevant phenomena in NMR, the Bloch equations:

$$\begin{aligned} \frac{dM_x}{dt} &= \gamma(M_yB_0 + M_zB_1 \sin \omega t) - \frac{M_x}{T_2} \\ \frac{dM_y}{dt} &= \gamma(M_zB_1 \cos \omega t - M_xB_0) - \frac{M_y}{T_2} \\ \frac{dM_z}{dt} &= \gamma(-M_xB_1 \sin \omega t - M_yB_1 \cos \omega t) - \frac{(M_z - M_0)}{T_1}. \end{aligned} \quad (2.11)$$

2.2 Signal detection

The correct treatment of the detection process demands a quantum-mechanical description through the proper detection operator. Notwithstanding, we shall use the semi-classical magnetization approach, which, for our purposes, will suffice.

Let us consider that the system is surrounded by a coil whose symmetry axis lies transverse to the main field \vec{B}_0 . If a transverse magnetization is made to precess at the Larmor frequency, an oscillatory electromagnetic field will be induced at frequency ω_0 . The precessing transverse magnetization is fundamentally necessary, for the detection principle is based on Faraday's law and on the motion of the magnetizing vector.

Next we separately mix the electromagnetic field with two heterodyne references, each 90° out of phase, thus obtaining separate in-phase and quadrature phase output signals, that can be interpreted as M_x and M_y . The signal is represented with complex numbers whose real part stands for the x -component in the rotating frame and the imaginary part for the y -component.

Let us consider a simple experiment, in which a 90° radio-frequency pulse is applied to the equilibrium magnetization vector $M_0\hat{k}$ (figure 3).

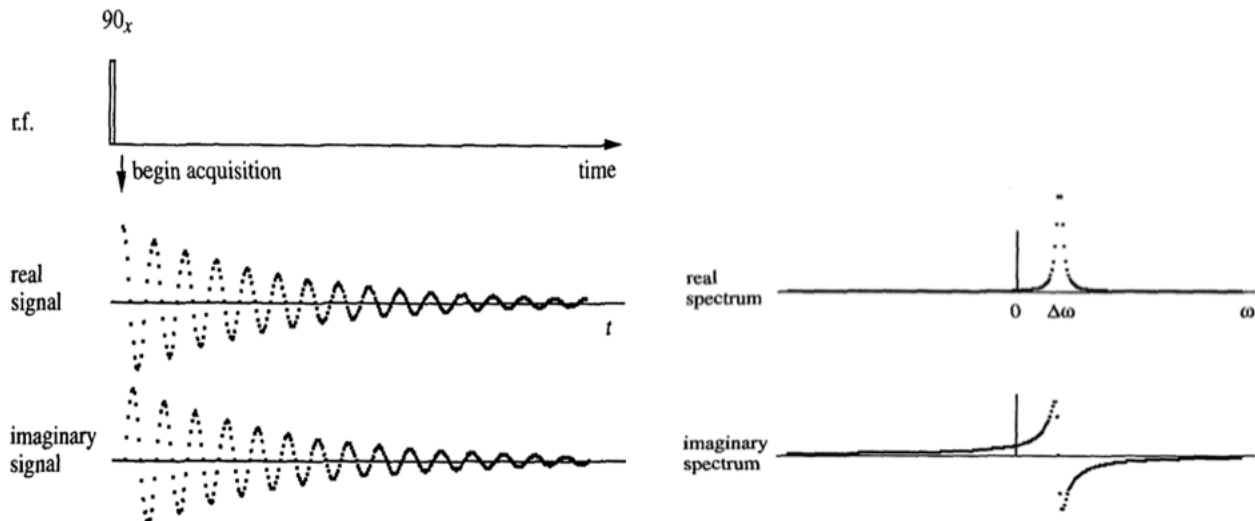


Figure 3: Free Induction Decay (FID) following a single 90° radio-frequency pulse. The real and imaginary parts of the signal correspond to the in-phase and quadrature receiver outputs. Real and imaginary dispersion spectra are depicted at the offset frequency $\Delta\omega = \omega_0 - \omega$ (reproduced from (5)).

The magnetization at time t after the pulse in the laboratory frame is given by:

$$\vec{M}(t) = [M_0 \cos(\omega_0 t) \hat{i} + M_0 \sin(\omega_0 t) \hat{j}] \exp(-t/T_2), \quad (2.12)$$

which can be written with complex numbers as:

$$M_+(t) = M_0 \exp(i\omega_0 t) \exp(-t/T_2). \quad (2.13)$$

Finally, the heterodyne signal at offset $\Delta\omega$ will be:

$$S(t) = S_0 \exp(i\phi) \exp(i\Delta\omega t) \exp(-t/T_2), \quad (2.14)$$

ϕ being the absolute receiver phase and S_0 the initial signal amplitude after the pulse (which is proportional to M_0). The oscillating, decaying signal, which is induced by the magnetization in free precession, is therefore named the Free Induction Decay - FID. The FID is Fourier transformed into the frequency domain, so we can study the real and imaginary parts of the transform, the so-called absorption and dispersion spectra, respectively (figure 3).

2.3 NMR applied to Diffusion

Thanks to its capability of encoding spatial information, the NMR signal enables us to study a multitude of otherwise inaccessible microscopic media. The application of a linearly varying magnetic field across the investigated sample has the effect of ascribing a spatial dependence to the spins' Larmor frequencies, thereby allowing us to obtain "images" of the sample, i.e., 3-d maps in which the voxels values are proportional to the desired NMR parameter. In the present section we review the hallmarks of NMR imaging. First, we demonstrate the fundamental conjugate relationship between the NMR signal and the spin density. In the remainder subsections, we explain the basic tools of diffusion-weighting: the Hahn spin echo, the addition of a proper gradient pulse sequence and the q-space formalism.

2.3.1 Spin density and k-space

A linearly varying field, known as a field gradient, is applied in addition to the much larger static field (\vec{B}_0) by means of specially shaped coils. Since the magnitude of any additional fields produced by the gradient are much smaller than B_0 , the Larmor frequency is only affected by the component parallel to \vec{B}_0 . For that reason, the Larmor frequency at point \vec{r} is given by

$$\omega(\vec{r}) = \gamma B_0 + \gamma \vec{G} \cdot \vec{r}, \quad (2.15)$$

where \vec{G} is the gradient of the pulsed gradient field component in the direction of \vec{B}_0 . Thanks to this linear relation between Larmor frequency and spin coordinate \vec{r} we can use the NMR signal to construct an image of the spin density.

Let us consider the nuclear spins that occupy the infinitesimal element of volume dV centered at position \vec{r} . According to 2.14, the NMR signal from this element is

$$dS(\vec{G}, t) \propto \rho(\vec{r}) dV \exp[i\omega(\vec{r})t]. \quad (2.16)$$

Using 2.15 and neglecting for simplicity the constant of proportionality, we obtain:

$$dS(\vec{G}, t) = \rho(\vec{r}) dV \exp[i(\gamma B_0 + \gamma \vec{G} \cdot \vec{r})t]. \quad (2.17)$$

Equation 2.17 assumes that our gradient is sufficiently large so we can disregard the signal decay due to transverse relaxation. The detected signal is then submitted to the

process called "heterodyne mixing": it is mixed with a reference oscillation, which is chosen to be γB_0 - the "on-resonance" condition. As the resultant signal oscillates at $\gamma \vec{G} \cdot \vec{r}$, we can neglect the term γB_0 and write the integrated signal amplitude as

$$S(t) = \iiint \rho(\vec{r}) \exp[i \gamma \vec{G} \cdot \vec{r} t] d\vec{r}. \quad (2.18)$$

At this point, we introduce the concept of a reciprocal space vector, \vec{k} , which is expressed in units of reciprocal space (m^{-1}) and equals:

$$\vec{k} = (2\pi)^{-1} \gamma \vec{G} t. \quad (2.19)$$

Using the k-space formalism and recalling the definition of Fourier transform, 2.18 yields:

$$S(\vec{k}) = \iiint \rho(\vec{r}) \exp[i 2\pi \vec{k} \cdot \vec{r}] d\vec{r} \quad (2.20a)$$

$$\rho(\vec{r}) = \iiint S(\vec{k}) \exp[-i 2\pi \vec{k} \cdot \vec{r}] d\vec{k}. \quad (2.20b)$$

Equations 2.20 express the fundamental relationship of NMR imaging: the acquired signal, in the frequency domain, is the Fourier transform of the spin density.

2.3.2 Simple (Hahn) spin echo

It is not always possible to have a completely homogeneous static field. Even in conventional NMR, where no magnetic field gradient is applied, the polarizing magnet frequently produces field perturbations, which impair different Larmor precession frequencies to the spins. This inhomogeneity results in a field spread across the sample of ΔB_0 . This spread causes a dephasing of transverse magnetization after the 90° r.f. pulse. The coherence of the transverse magnetization therefore lasts for a time of order $(\gamma \Delta B_0)^{-1}$, which would theoretically put a limit on the time over which the magnetization could be manipulated.

E. Hahn (6) proposed a natural solution to deal with this phase decoherence: if we apply a second 180° r.f. pulse a time τ after the first pulse, the signal will refocus at time 2τ (figure 4), this resulting phase coincidence being known as a spin echo.

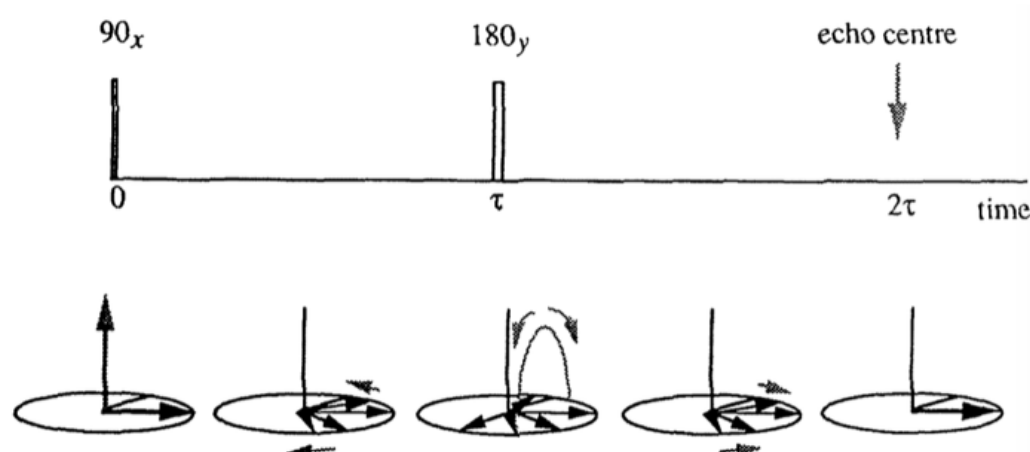


Figure 4: spin echo pulse sequence showing the evolution of the magnetization. The 180_y pulse inverts the phase of each spin isochromat so that perfect refocusing occurs at time $t=2\tau$ (adapted from (5)).

In systems described only by Zeeman Hamiltonians, the spin echo sequence corrects all dephasing due to inhomogeneous broadening, chemical shift and heteronuclear scalar spin-spin interactions. Since homonuclear scalar spin-spin interactions are not refocused and residual attenuation due to spin-spin relaxation is to be accounted for, we can plot a number of echo amplitudes obtained from different values of τ to obtain T_2 according to the equation

$$M_y(2\tau) = M_0 \exp(-2\tau/T_2). \quad (2.21)$$

2.3.3 Diffusion in the presence of a gradient

An echo, as we just saw, will ensue only if the nuclei experience the same local Larmor frequency during the dephasing and rephasing parts of the cycle. Once a gradient field is applied, different positions along the sample will experience different local magnetic fields and therefore different Larmor frequencies. Perfect refocusing would only occur in the case the nuclei did not move in the direction of the applied gradient. Far from being a disadvantage, it is precisely the imperfect refocusing of the echo signal due to molecular movement that will allow us to quantify diffusion.

We model diffusion molecular self-diffusion as a succession of discrete steps in one dimension, the direction of the field gradient. Let τ_s be the mean time between steps and ξ be the root mean square displacement in one dimension. The distance travelled in the z-axis by a molecule after n jumps, considering that left and right jumps are equiprobable, is:

$$Z(n\tau_s) = \sum_{i=1}^n \xi a_i, \quad (2.22)$$

where a_i is a random number equal to ± 1 . Therefore the ensemble mean square displacement - MSD after n jumps can be written:

$$\overline{Z^2(n\tau_s)} = \sum_{i=1}^n \sum_{j=1}^n \xi^2 \overline{a_i a_j} , \quad (2.23)$$

where the horizontal bar stands for ensemble average. Since a_i can assume randomly the values +1 or -1, $\overline{a_i a_j} = 0$ unless $i = j$. Thus:

$$\overline{Z^2(n\tau_s)} = \sum_{i=1}^n \xi^2 \overline{a_i^2} = \xi^2 \sum_{i=1}^n 1 = n\xi^2 . \quad (2.24)$$

If we define the self-diffusion coefficient as

$$D = \xi^2 / 2\tau_s , \quad (2.25)$$

then the ensemble MSD in one dimension will be:

$$\overline{Z^2(t)} = 2Dt , \quad (2.26)$$

which is equivalent to the result obtained on section 1.2 above (equation 1.12)

Let us now consider that a magnetic field gradient is applied. We want to compute how much diffusion influences the signal coherence. The approach follows the classical treatment of Carr and Purcell (7).

Considering for convenience that the spins are placed at $z = 0$, the local Larmor frequency is

$$\omega(n\tau_s) = \gamma B_0 + \gamma G \sum_{i=1}^n \xi a_i \quad (2.27)$$

and the cumulative phase after time $n\tau_s$ is

$$\phi(t) = \gamma B_0 n\tau_s + \sum_{m=1}^n \gamma G \tau_s \sum_{i=1}^m \xi a_i . \quad (2.28)$$

Dephasing is caused only by the second term on the above equation, the phase deviation, since it varies randomly across the sample. We can write it

$$\Delta\phi(t) = \gamma G \tau_s \xi \sum_{i=1}^n (n+1-i) a_i , \quad (2.29)$$

a relationship that is illustrated by figure 5.

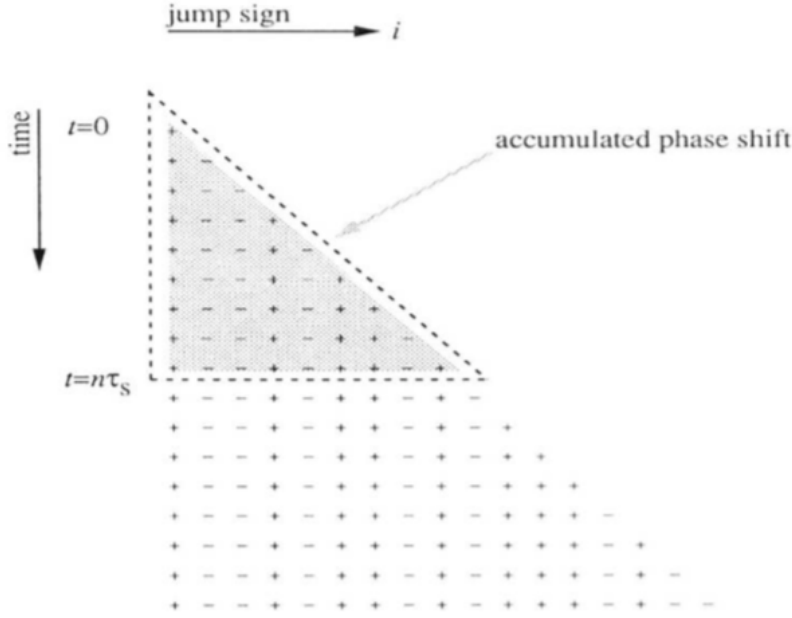


Figure 5: Cumulative phase diagram in which the sign at the end of each row indicates whether the jumps in the current τ_s interval are positive or negative with respect to the gradient direction. The precessional phase shift which results during that interval is determined by the net position in the gradient and is therefore calculated by summing jumps along the row. The cumulative shift at time t is given by the sum within the shaded triangle (reproduced from (5)).

$\Delta\phi(t)$ varies randomly across the sample and as a consequence of the diffusion process, the ensemble-averaged transverse magnetization will be phase modulated by the term $\exp(i\Delta\phi)$. Thanks to the fact that the central limit theorem is usually applicable to systems consisting of a huge number of particles (like the present case), we can generally assume that the dephasing is distributed according to a Gaussian PDF (let us call it $P(\Delta\phi)$). So we can write

$$\overline{\exp(i\Delta\phi)} = \int_{-\infty}^{\infty} P(\Delta\phi) \exp(i\Delta\phi) d(\Delta\phi). \quad (2.30)$$

Recalling that $P(\Delta\phi)$ is a normalized Gaussian distribution, the solution to the above integral is well known:

$$\overline{\exp(i\Delta\phi)} = \exp(-\overline{\Delta\phi^2}/2). \quad (2.31)$$

Next we take the ensemble average of the square eq. 2.29 so that we can evaluate $\overline{\Delta\phi^2}$ (noting again that cross-terms vanish and that n is assumed large):

$$\begin{aligned} \overline{\Delta\phi^2} &= \gamma^2 G^2 \tau_s^2 \xi^2 \sum_{i=1}^n (n+1-i)^2 \\ &= \gamma^2 G^2 \tau_s^2 \xi^2 \sum_{j=1}^n j^2 \\ &= \frac{1}{3} \gamma^2 G^2 \tau_s^2 \xi^2 n^3. \end{aligned} \quad (2.32)$$

If we substitute eq. 2.25, we find the expression for the signal attenuation caused by diffusion:

$$\overline{\exp(i\Delta\phi)} = \exp(-\frac{1}{3}\gamma^2 G^2 D t^3). \quad (2.33)$$

We turn again to the spin echo sequence and recall that the 180° r.f. pulse applied at time t reverses all the phase shifts which existed before t . The phase step diagram is displayed on figure 6.

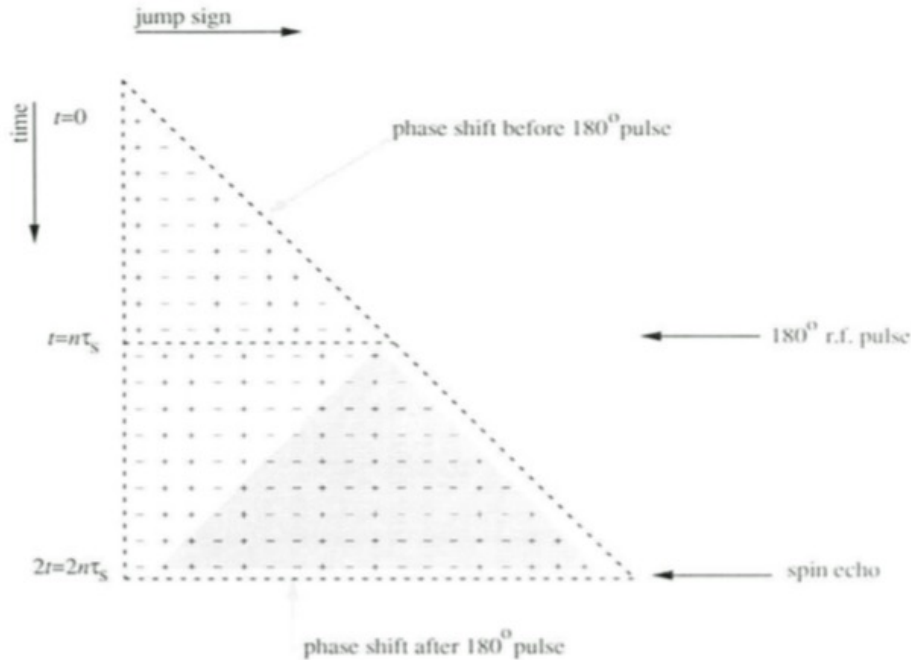


Figure 6: Cumulative phase diagram for spin echo formation in a steady magnetic field gradient. The net phase shift is the sum of that occurring before and after the 180° r.f. pulse and corresponds to the shaded region (reproduced from (5)).

The net phase shift which occurred before the 180° r.f. pulse is completely cancelled by a section of the second evolution period. The remaining, shaded section corresponds to the residual phase shift at the time of the echo. The value of $\overline{\Delta\phi^2}$ which applies in the case of the echo is twice the value calculated in figure 5. Thus, the following relationship is valid for the echo at $2t$:

$$\begin{aligned} \overline{\exp(i\Delta\phi)} &= \exp(-\frac{2}{3}\gamma^2 G^2 D(2t)^3) \\ &= \exp(-\frac{1}{12}\gamma^2 G^2 D(2t)^3), \end{aligned} \quad (2.34)$$

the second form expressing the attenuation in terms of the time from the first r.f. pulse to the echo.

2.3.4 Pulsed Gradient Spin Echo

The diffusion of the sample molecules under the application of a steady gradient leads to the attenuation of the echo signal. As we saw, it is thanks to that phenomena that we are able measure the self-diffusion coefficient. The method, however, is not applicable when the motion is slow, for steady gradients spread the Larmor spectrum also during r.f. pulse transmission and signal detection, and for that reason the transmitter and receiver bandwidths impose a limit on the maximum possible gradient.

The Pulsed Gradient Spin Echo - PGSE sequence, first demonstrated by Stejskal and Tanner in 1965 (8), contours this problem by limiting the gradient application to rectangular pulses inserted in the dephasing and rephasing parts of the echo sequence (figure 7).

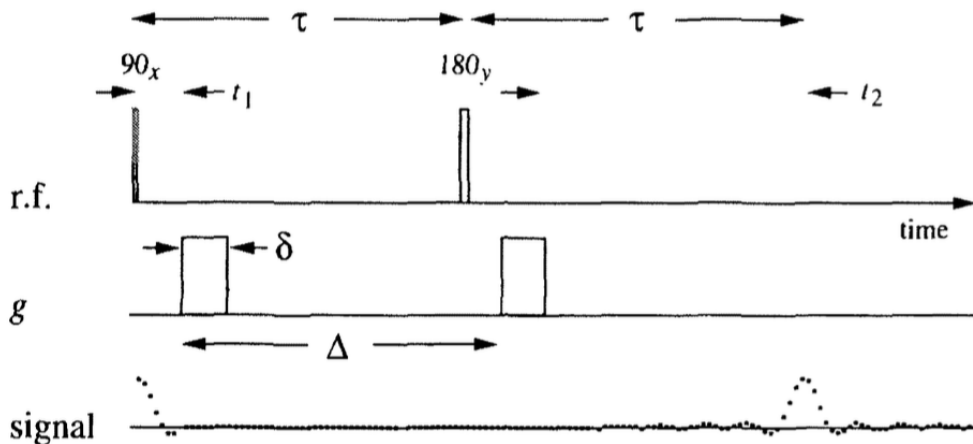


Figure 7: Pulsed Gradient Spin Echo (PGSE) sequence with gradient amplitude, g , gradient pulse duration, δ , and gradient pulse spacing, Δ . τ is the time between the 90_x and 180_y r.f. pulses and corresponds to half the spin echo formation time, T_E (reproduced from (5)).

We refer to the phase step diagram in figure 8 for the following calculation. Let us consider that the pulses have duration δ and separation Δ . Noting that the phase shifts cancel on the unshaded areas, we compute the net phase shift by summing two triangular areas, each having mean square phase shift $\frac{1}{3}\gamma^2 g^2 \tau_s^2 \xi^2 n^3$, and a rectangle with mean square phase shift $\gamma^2 g^2 \tau_s^2 \xi^2 n^2(p - n)$. We can thus write the net mean square phase shift as

$$\begin{aligned} \overline{\Delta\phi^2} &= \gamma^2 g^2 \tau_s^2 \xi^2 n^2(p - n + \frac{2}{3}n) \\ &= 2 \gamma^2 g^2 \delta^2 D(\Delta - \delta/3). \end{aligned} \quad (2.35)$$

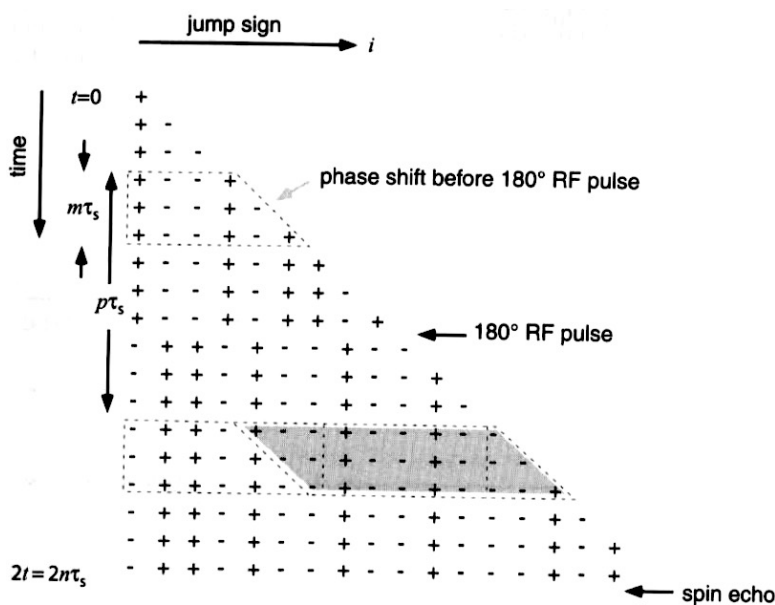


Figure 8: cumulative phase diagram for spin echo formation in the PGSE experiment. The net phase shift is the sum of that occurring before and after the 180° r.f. pulse and corresponds to the shaded region. Note that $\delta = m\tau_s$ and $\Delta = p\tau_s$ (reproduced from (9)).

Using eq. 2.31 we obtain the classical expression for the echo amplitude attenuation, the Stejskal-Tanner equation:

$$S(g) / S(0) = \exp [-\gamma^2 g^2 \delta^2 D (\Delta - \delta/3)] . \quad (2.36)$$

If we use the b-factor, a well-known NMR parameter,

$$b = \gamma^2 g^2 \delta^2 (\Delta - \delta/3) , \quad (2.37)$$

the equation 2.36 can be rewritten in the common form

$$S(g) = S(0) \exp (-bD) . \quad (2.38)$$

The PGSE sequence is the experimental setting assumed by the Monte Carlo simulations in the present study.

2.3.5 The q-space

The PGSE method gives us information about the self-correlation function, P_s ¹. We will calculate the resultant signal, assuming the narrow-pulse approximation ($\delta \ll \Delta$). The gradient pulse imparts a phase shift $\gamma\delta\vec{g} \cdot \vec{r}$ to a spin located at \vec{r} . If the spin subsequently moves to a position \vec{r}' , the net phase shift will be $\gamma\delta\vec{g} \cdot (\vec{r}' - \vec{r})$. In order to arrive at the total signal, we need to calculate the ensemble average of the individual net phase shift $\exp(i\gamma\delta\vec{g} \cdot (\vec{r}' - \vec{r}))$, weighted by the probability for a spin to be initially at \vec{r} and then to move from \vec{r} to \vec{r}' during the diffusion time (Δ), i.e., $\rho(\vec{r}) P_s(\vec{r}|\vec{r}', \Delta)$:

$$S_\Delta(\vec{g}) = \int \rho(\vec{r}) \int P_s(\vec{r}|\vec{r}', \Delta) \exp[i\gamma\delta\vec{g} \cdot (\vec{r}' - \vec{r})] d\vec{r} d\vec{r}' . \quad (2.39)$$

A reciprocal space \vec{q} can be defined as

$$\vec{q} = (2\pi)^{-1}\gamma\delta\vec{g} , \quad (2.40)$$

thereby allowing us to rewrite eq. 2.39 as

$$S_\Delta(\vec{q}) = \int P_s(\vec{R}, \Delta) \exp(i2\pi\vec{q} \cdot \vec{R}) d\vec{R} , \quad (2.41)$$

in which \vec{R} stands for the displacement between initial and final positions. According to eq. 2.41, we can see that $S_\Delta(\vec{q})$ and $P_s(\vec{R}, \Delta)$ are Fourier conjugates. Therefore it is possible to estimate the self-diffusion propagator of a molecular system by means of the signal obtained in a PGSE experiment performed in the sample.

¹ The self-correlation function $P_s(\vec{r}|\vec{r}', t)$ gives the probability that a molecule initially at \vec{r} moves to \vec{r}' after a time t and is therefore to the propagator defined on section 1.2 above.

2.4 Susceptibility effects

There are a number of gradient artifacts, called "background gradients", that introduce subtle perturbations to the Stejskal-Tanner relation. Those background gradients may arise: (1) out of intentional application, (ii) as a result of an imperfect static field or (iii) due to the heterogeneities in the sample's magnetic constitution (10). Here we are especially concerned with internal magnetic field gradients. They arise in heterogeneous samples out of the susceptibility difference between the pore matrix and the diffusing liquid and perturb the magnetic field near the interface between the two elements. This perturbation affects the Larmor frequencies near the interfaces by a factor

$$\sqrt{\Delta\omega^2} \sim \gamma\Delta\chi B_0, \quad (2.42)$$

in which $\Delta\chi$ is the susceptibility difference between the media. As we can see, the effect increases linearly with the magnitude of the static magnetic field, B_0 .

Far from being an unavoidable annoyance, internal gradients add information to the acquired signal that can help us better discern the sample's microscopic features.

The effect of background gradients can be readily evaluated for the case of a steady background gradient (figure 9).

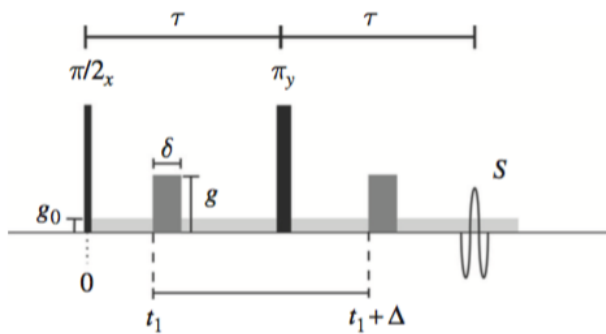


Figure 9: the Hahn spin echo based PGSE sequence including a background gradient \vec{g}_0 . For simplicity the background gradient is assumed uniform in magnitude and direction throughout the entire sample during the sequence (reproduced from (10)).

Considering a uniform, constant background gradient \vec{g}_0 (the applied gradient is \vec{g}) and neglecting relaxation effects, the PGSE signal of the Hahn spin echo sequence is given by (10)

$$S(2\tau) = S_0 \exp\left(-\underbrace{\gamma^2 g^2 \delta^2 D(\Delta - \delta/3)}_{g \text{ term}} + \underbrace{\gamma^2 \vec{g} \cdot \vec{g}_0 D \delta [t_1^2 + t_2^2 + \delta(t_1 + t_2) + \frac{2}{3}\delta^2 - 2\tau^2]}_{\vec{g} \cdot \vec{g}_0 \text{ cross-term}} - \underbrace{\gamma^2 g_0^2 D \frac{2}{3} \tau^3}_{g_0 \text{ term}}\right), \quad (2.43)$$

where $t_2 = 2\tau - (t_1 + \Delta + \delta)$.

In eq. 2.43 two terms are added to the basic Stejskal-Tanner relation (the "g term"). The term g_0 can usually be disregarded through normalization. The cross-term, however, cannot be neglected². Due to the cross-term, the echo attenuation may depend not only on δ and Δ , but also on the other delays in the sequence.

In any case, the present treatment - in which we deal only with steady background gradients - is a simplification. The internal gradients found in porous media are highly inhomogeneous. Except perhaps for special cases involving particular geometries, we will not have at our disposal a working analytical expression analogous to eq. 2.43. In those cases a numerical method can be used to estimate the effect of internal gradients. In the next chapter, we will explain the method employed to compute internal gradients in the present simulations - the Finite Perturber Method.

² Unless specific conditions hold: either $g\delta \gg g_0\tau$ or, if \vec{g}_0 is not constant, $g\delta \gg \langle g_0^2 \rangle^{1/2} \tau$.

Chapter 3

The simulation apparatus

The fundamental objective of my thesis is to simulate and study the Nuclear Magnetic Resonance - NMR signal attenuation for samples with specific geometry. A specific goal was to devise a program that could calculate the contribution of internal gradients due to susceptibility differences to the total signal attenuation. A similar idea was recently advanced by a fellow colleague from University of Rome (11). However, while his study was limited to two-dimensional systems of specific geometries for which the internal gradients calculation was abbreviated by known analytical solutions, my approach intended to extend the analysis to three-dimensional systems and arbitrary geometries. To accomplish that goal, I employ a recently proposed method of numerical calculation - the Finite Perturber Method.

3.1 The program

In order to make simulations on NMR experiments I wrote a program in MATLAB[®] (R2016b, the MathWorks, Inc., Natick, MA, USA). The program is composed of three blocks: "Geometry", "Random Walk" and "Signal Calculation". The Geometry block creates the simulation space, i.e., a "box" containing virtual 3-D objects. These simulation spaces / 3D-objects represent the solid matrix in whose interstices (the "pores") the simulations of diffusing water molecules will take place. In the present work I studied diffusion in two types of simulation spaces, or geometries: 1) spheres of equal diameter randomly dispersed inside the box; and 2) a bundle of randomly disposed parallel cylinders of different diameters. There are small variations that were introduced in the program so it could run the two types of simulation. These variations will be explained in the relevant subsections. In any case I stress that the program's possible applications are open-ended: due to its modular format it can be extended to simulate any arbitrary geometry. The next block, "Random Walk", is responsible for simulating trajectories of molecules inside the previously created simulation spaces. Finally, the third block, "Signal Calculation", is the one which simulates signal acquisition through a PGSE sequence. It includes a sub-routine that calculates the contribution of internal gradients to the signal attenuation. The three blocks will be explained in the following.

3.1.1 The Geometry block

The Geometry block deals with the construction of the simulation space. The block was built in modular form: in order to construct a new kind of simulation space it suffices to add the corresponding subroutine. Presently it contains two of these changeable subroutines - "Monospheres" and "Axons" - along with a fixed one, called "Burning_algo", that I now describe.

a) Monospheres. The first group of simulations seek to emulate the experimental setting described in (12) i.e., random packings of spheres of equal diameter (see Chapter 4 below for description of these simulations). Therefore the first subroutine of the Geometry block, called "Monospheres", creates a virtual "box" where spheres with same radius are disposed randomly and in different packing ratios. The inputs for "Monospheres" are: number of spheres (N , maximum: 1000), fraction of occupancy (packing ratio) (PHI) and resolution (RES).

First, the script uses the three inputs to calculate the radius of the spheres. It is constrained by two conditions: 1) that the spheres should be impenetrable; and 2) that the N spheres are completely contained in the volume³, that is, the container's boundaries are hard (not periodical). When discussing the second block (Random Walk) I will comment on a possible disadvantage of such condition and show how I managed to eliminate it.

The script then assigns the N spheres to random positions inside the $\text{RES} \times \text{RES} \times \text{RES}$ voxel. Next, it gradually adjusts the positions of the spheres until arriving at a configuration of minimum or no overlap. In order to do that, the algorithm uses a soft potential function similar to the one defined in (13). The potential function is the sum of a potential, calculated for each pair, and dependent on the center-to-center distance (r_{ij}) and the spheres' diameter (d_{ij} , always the same, since the spheres are equal):

$$V(r_{ij}) = \alpha (1 - (r_{ij}/d_{ij})^\beta)^\gamma \Theta(1 - r_{ij}/d_{ij}). \quad (3.1)$$

In order to calibrate the potential function to the present problem, I changed the article's original parameters ($\alpha = 0.5$; $\beta = 1$; $\gamma = 2$). Optimal results were achieved with $\alpha = 10.000$; $\beta = 2$ and $\gamma = 4$.

Next, the routine minimizes the above defined potential in order to arrive at the final positions of the spheres. It is an optimization problem subject to constraints to which a non-linear method is applied ("Interior-point algorithm"). A demonstration of the routine can be seen in the figure below, which was made for 100 spheres, 62% packing ratio and a $80 \times 80 \times 80$ -cell box (figure 10):

³ Since the simulation space represents a NMR imaging unit, henceforth the words "simulation space", "volume" and "voxel" are all intended to be synonyms.

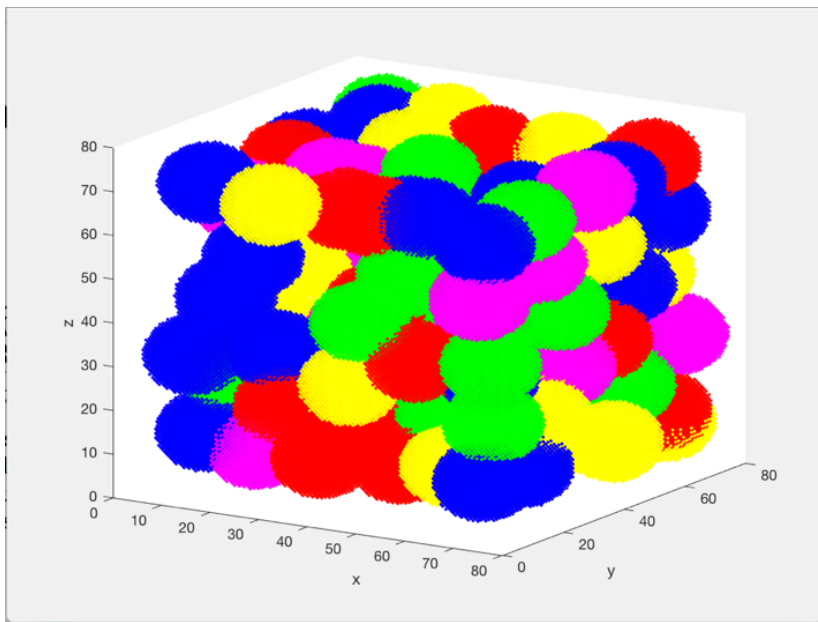


Figure 10: Simulation space consisting of 100 spheres in a 62% packing ratio. The "box" is divided in $80 \times 80 \times 80$ volumetric units.

Three remarks are necessary: first, this is not a mere illustration: it is a plot of the true output of the program to which five colors were added just to help the visualization. Second, in order to speed up image generation, a low resolution - $80 \times 80 \times 80$ - was chosen (that is why the image quality of this figure is poor). The resolution used in the simulations is much finer ($256 \times 256 \times 256$). Third, the simulations also use more spheres: 500.

The last step of the Monospheres subroutine is the digitalization of the volume. That is, for every one of the RESxRESxRES cells, a number is assigned: 0 (zero) for cells whose center lies outside all spheres; and the number "n" if the cell center lies inside the nth sphere. The subroutine's output is thus a RESxRESxRES matrix of integers representing occupied/pore spaces.

b) Axons. The second group of simulations (see Chapter 5) seek to emulate water diffusion in particular white matter tracts of the brain, namely the axonal bundles. The corresponding routine of the Geometry block - "Axons" - creates a virtual "box" where cylinders with different radii are randomly disposed. In fact each created cylinder is a coaxial pair, of which the innermost cylinder represents the axon body and the outermost cylinder represents its myelin sheath. The routine allows us to set their degree of myelination ("DEG", a real number between 0 and 1). This means that, whenever this parameter is set lower than 1, say 0.7, the program outputs a simulation space with cylinders whose "sheaths" are randomly degraded by a corresponding factor - in the present example, 30% ($1 - 0.7$). "Axons" takes one parameter as input: precisely the parameter "DEG" which we have just introduced. Since the details of this subroutine's architecture are intricately linked to the microscopic description and modellization of neuronal tracts I postpone the presentation of these details until Chapter 5, when we will have the opportunity to dwell on biomedical data.

c) Burning Algo. This is the third subroutine of the geometry block and it takes as input the digital matrix representation of the volume, produced by the Monospheres subroutine. The aim here is to determine pore connectivity for the entire space. To achieve that, the subroutine must classify each one of the pore cells (which initially are all set to zero) with a new number so that any pair of connected pore cells shall share the same number and any pair of unconnected pore cells shall have different numbers. The applied algorithm is of the type "burning forest". For its implementation I took inspiration from the brief description included in (14).

Burning Algo outputs a matrix of integers whose cells represent either the occupied spaces (numbers 1 to N) or the pore spaces (numbers counting from 1001 and depending on connectivity). I called it the "connected matrix".

3.1.2 The Random Walk block

The next block concerns the simulations of molecules' trajectories to be run in the space created by the first block. Due to the particularities of the axons' modellization, a number of variants were introduced in the case of their simulations. I shall comment on these variants later on (Chapter 5). Here, I discuss the features of the Random Walk block as they were used for the spheres' simulations. First of all, the script imports a file generated by the Geometry block. The file contains the connected matrix, that is, the digitalized version of the simulation space indicating occupied and pore spaces and a variable containing the value of the spheres' diameter in coordinate units⁴. The other parameters are: the number of spins⁵, the length (in meters) of the average jump that each spin will make in a given simulation step, the diameter (in meters) that we wish to attribute to the spheres⁶ and total simulation time (in seconds). A further parameter, always fixed, is the diffusion constant, set to the value of free water diffusion, $2.30 \times 10^{-9} \text{ m}^2\text{s}^{-1}$.

Next, the routine calculates the parameters that control the random walk. In addition, the program needs to convert the step length to coordinate units. As we have seen in the previous paragraph, the step length is in SI units. The simulations, however, use coordinate units. The parameters are calculated by the Random Walk block in this way:

⁴ Remember that the Geometry block digitalizes the simulation space according to the chosen resolution, RES. The coordinate unit is defined as $1/\text{RES}$ of the side of the simulation space.

⁵ The words "spins" and "molecules" are here used interchangeably.

⁶ In this manner, the same file generated by the Geometry block can be used to simulate dispersed spheres of any physical diameter.

- from the step length, the diffusion constant and total simulation time it calculates the number of simulation steps;
- from the diameter of the spheres in coordinate units (provided by the Geometry block) and the diameter in meters (chosen by the user) it calculates the conversion factor coordinate/meter.
- from the step length in meters (chosen by the user) and the conversion factor it calculates the step in coordinate units.

The routine then assigns random initial positions to each spin. An algorithm guarantees that all initial positions are located in void spaces (i.e., cells whose value is greater than 1000). Next, the script runs the simulation of every spin's trajectory. In order to create realistic trajectories the program obeys a protocol with the following characteristics:

- **Avoidance of wall effects.** As stated in the Geometry block (3.1.1), the spheres are randomly placed inside a "box" whose boundaries are hard (not periodical). The spheres near the container wall form more ordered structures than those in the internal region of a random packing (15). We wish to study random configurations, thus in order to avoid wall effects, the trajectories were limited to a central region of the "box" comprising 60% of the total volume.
- **Avoidance of surface effects.** Surface effects are undesirable alterations of the ensemble dynamics due to the limited size of our simulation space and the comparatively huge number of molecules that will tend to interact with the containing walls (16). The classic way of overcoming this problem is by the introduction of periodical boundary conditions. Thus, since we saw in the former paragraph that the trajectories must remain in a central region comprising 60% of the total volume, whenever a molecule leaves this central region, it reenters the region through the opposing face.
- **Normal step.** To calculate each new position (X_i , Y_i , Z_i) for a given spin, in every simulation step the algorithm randomly picks 3 numbers sorted out of a normal distribution:

$$X_i = X_{i-1} + \text{step} \times N$$

$$Y_i = Y_{i-1} + \text{step} \times N$$

$$Z_i = Z_{i-1} + \text{step} \times N , \quad (3.2)$$

where N stands for a number sorted out of a standard normal distribution. The above equation guarantees that each simulation step length will be drawn from a Gaussian distribution with mean = zero and standard deviation = step, i.e., the mean step length in coordinate units as calculated by the Random Walk block (see above).

- **Reflecting wall condition.** The spins' trajectories shall respect the confining geometry, i.e., they can neither penetrate a region of space occupied by a sphere nor transit between pores that are not connected. The program implements these two constraints by allowing particle displacements only if the cells corresponding to the initial and final positions have been ascribed a number > 1000 (thus guaranteeing that they are located inside a pore) AND if both numbers are equal (which guarantees that both pore positions are connected).
- **Movement retrial.** If the two conditions described in the last paragraph are not met, the script recalculates the displacement (using the relations described in "Normal step" above) and again checks whether the move is acceptable. The script repeats this procedure 10 times at most. If no acceptable move is found, the particle remains in the same position. This guarantees that the script will not enter an infinite loop.

The idea behind the simulation protocol just described is not only to prevent physically impossible moves, but also to create more realistic trajectories overall. The fact that this random walk algorithm uses not a fixed but a normal step and the fact that the script retries unaccepted moves both contribute to make the particles explore the pore geometry maximally (e.g., by entering tapered regions, narrow passages etc.) This protocol is an improvement over schemes that employ same-length steps and all-or-nothing move decisions (where, in a single try, either the particle moves - the displacement being always the same length - or the particle does not move).

Every run of the routine simulates the movement of the chosen number of spins and produces as output a matrix containing, for every spin, the three coordinates of each simulation step.

3.1.3 The Signal Calculation block

The third and final block is concerned with the calculation of the NMR signal attenuation (S/S_0) with and without the addition of the internal magnetic gradient contribution. It takes as input the "connected matrix" calculated by the Geometry block (see 3.1.1), the main field intensity (B_0), the direction of the applied gradient (\vec{k} , a 3-D vector), the magnetic susceptibility difference between water and the confining tissue ($\Delta\chi$), the gradient pulse duration - δ , the interval between the two pulses (Δ) and a vector containing n different b-values to be used (b). All parameters are entered in SI units.

Naturally an additional input is the simulated trajectories - a tabular listing of the particles' x, y and z coordinates for each simulated step - provided by the Random Walk block.

The script calculates signal attenuation first without the internal gradient contribution. After the calculation, a plot of the signal decay as a function of the b-values is produced. Remark however that in all experiments the gradient strength was the only varying quantity. The script works backwardly, departing from the input vector of b-values and calculating for each one the corresponding gradient magnitude (g), using eq. 2.37:

$$b = \gamma^2 g^2 \delta^2 (\Delta - \delta/3), \quad (3.3)$$

where γ is the gyromagnetic ratio ($\gamma = 267.513 \cdot 10^6 \text{ rad s}^{-1} \text{ T}^{-1}$). Each cycle of the routine corresponds to one "experiment" in which signal decay is computed for a particular value of "b", that is, for a particular gradient. The routine halts after the computation for the n b-values from the input vector has been completed.

In each cycle the routine uses the respective gradient magnitude (g), the direction of gradient application (the unitary vector \hat{k} calculated from the input \vec{k}) and the positions produced by the random walk (a 3-D vector \vec{r} for each simulated step) to update the accumulated phase of each spin using the formula

$$\Delta\phi = \gamma dt \sum_{j=1}^{numsteps} g \hat{k} \cdot \vec{r}(j), \quad (3.4)$$

where the total number of simulated steps ("numsteps"), the time length of each step (dt) and the spin's positions (the vectors \vec{r}) are variables passed by the Random Walk block to the Signal Calculation block. Having calculated the phase accumulation ($\Delta\phi$) for each spin, the script then computes signal attenuation S/S_0 as the ensemble average $S/S_0 = \frac{1}{N} \sum_{n=1}^N \cos(\Delta\phi_n)$, where N is the number of simulated particles (17). The routine repeats the above steps for each cycle, i.e., for each b-value.

So far, the script has calculated signal attenuation without considering the internal gradient contribution. To compute the effect due to internal gradients, the script uses a subroutine called "Internal Gradient", to which we turn our attention.

Internal Gradient. The subroutine computes signal attenuation in the presence of internal gradients. It takes as input the spin position (x, y and z coordinate), the file containing the geometry, $\Delta\chi$ and B_0 (all passed by the Signal Calculation block main), and outputs the internal magnetic field shift for that position ($\Delta B_{int}(x,y,z)$). The computation of

the internal magnetic gradient follows the method called the Finite Perturber Method - FPM⁷, which we here briefly summarize.

Let us recall that the original simulation space is divided in RES x RES x RES cells that were digitalized, i.e., they were attributed a number indicating whether they are occupied or void. The algorithm calculates the perturbation of the local field (B_0 is the applied field) that the solid matrix induces on a given point by summing the contribution from each of the circumscribing occupied cells⁸ to the field deviation on the point. The field perturbation induced by one occupied cell on a point (x,y,z) is given by the formula

$$\Delta B_{cell}(x, y, z) = \left(\frac{6}{\pi}\right) \frac{\Delta x}{3} \frac{a^3}{r^3} (3 \cos^2 \theta - 1) B_0 , \quad (3.5)$$

where ' $\Delta B_{cell}(x, y, z)$ ' is the local perturbation of the field on the point (x,y,z) induced by the cell, 'a' is one-half the side length of the cell, 'r' is the magnitude of the vector from the cell center to the point (x,y,z) and θ is the angle between that vector and \vec{B}_0 (figure 11). As can be seen, the field is calculated as if each perturbing cell were a little sphere (for which an analytical solution to the field equations is well known) to which the correction factor ($6/\pi$) is added since the cells are in reality cubical, not spherical.

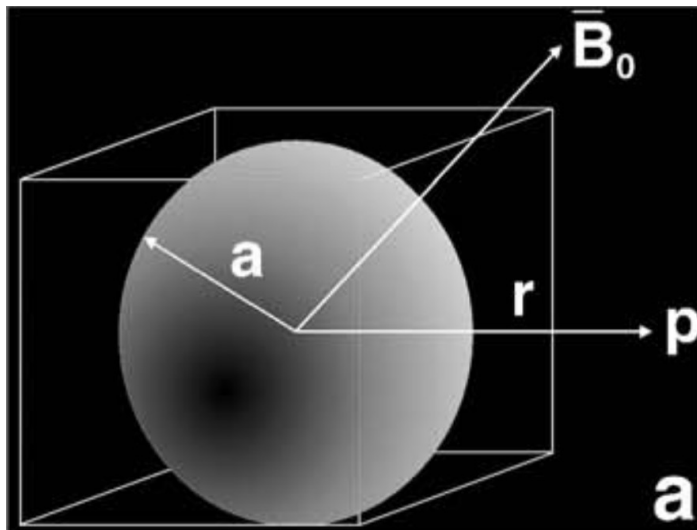


Figure 11: The geometry for the calculation of the magnetic field perturbation due to a tiny cube ("the finite perturber"). The field induced around the cube is estimated by considering a sphere of radius 'a' embedded in the cube (of radius '2a'). We wish to calculate the perturbation on point $p(x, y, z)$, which is located at a distance 'r' from the center of the perturber placed in field B_0 (reproduced from (18)).

The Finite Perturber Method relies on a fundamental approximation, which is considering the total perturbation as the sum of the perturbers' individual contributions,

⁷ For FPM's main reference, the original paper and two articles in which it is employed, see Bibliography, items 18, 19, 20 and 21 respectively.

⁸ An occupied cell is one whose center lies inside one of the volumes created by the geometry block (e.g. the monospheres). So, an occupied cell not necessarily lies completely inside a volume.

without coupling terms. Since the typical main magnetic field strengths (B_0) range in the order 1-10 T whereas susceptibility-induced magnetic field shifts are on the order 10^{-6} T, the effect of any inter-perturber interactions is negligible.

In my implementation two further approximations were made. The first one was to disregard any cross terms between the internal field and the applied gradient field. It means that to calculate the internal field (cf. formula above) only B_0 , without considering the local gradient, was used. The cross terms are negligible since the applied gradients are comparatively small. Considering the worst case, i.e., the strongest gradient used in the simulations ($g = 0.6843 \text{ T/m}$) and the largest simulation space (side length (L) = 0.28 mm), we can estimate that we are ignoring terms of order $\sim L \times g = 1.90e^{-4} \text{ T}$ or $o(10^{-3}) \Delta B_{\text{int}}$. The second approximation was to restrict the internal field calculation to a $9 \times 9 \times 9$ cells cubical region centered on the position for which the computation is being required⁹. This is justified by the fact that, according to eq. 3.5, the perturbation falls with the distance as $1/r^3$. For that reason the cells contained in the first shell of ignored cells contribute each with terms equivalent to $1/125$ or $o(10^{-2})$ the value of the nearest cells. Both approximations were done to simplify calculations and reduce computation time.

As stated above, the total variation of the local magnetic field on a point (x, y, z) is the sum of the perturbations (eq. 3.5) induced by the 728 ($9^3 - 1$) circumscribing cells:

$$\Delta B_{\text{int}}(x, y, z) = \sum_{\text{circumscribing cells}} \Delta B_{\text{cell}}(x, y, z). \quad (3.6)$$

This is the value returned by the subroutine Internal Gradient to the Signal Calculation main.

Finally, the Signal Calculation block calculates signal attenuation with internal gradient computing. The accumulated phase of each spin is numerically calculated according to the numerical formula (cf. relation 3.4):

$$\Delta\phi = \gamma dt \sum_{j=1}^{\text{numsteps}} (g \hat{k} \cdot \vec{r}(j) + \Delta B_{\text{int}}(\vec{r}(j))). \quad (3.7)$$

The script then computes the attenuation signal S/S_0 as the ensemble average $S/S_0 = \frac{1}{N} \sum_{n=1}^N \cos(\Delta\phi_n)$ (where N is the number of simulated particles) as before. In the end the program displays graphics of the signal attenuation (with and without internal gradient computing) and fits both results to a one-parameter Mittag-Leffler function of the form (more on this on the next chapter):

$$S/S_0 = E_\alpha(-(bD)^\gamma). \quad (3.8)$$

⁹ Instead of calculating the field shift due to all the $256 \times 256 \times 256$ cells (when resolution is set to 256). This is an adaptation I introduced in the algorithm. In the original FPM method the calculation is accomplished through the use of a Fast Fourier Transform.

The program uses the algorithm (22) for the computation of the Mittag-Leffler function and Matlab's built-in nonlinear least-squares solver "lsqcurvefit" with the Levenberg-Marquardt algorithm for all fitting procedures.

3.2 Validation

Two tests were run in order to verify that the Matlab program works as projected.

The first test consisted in a simulation of free diffusion. The aim was to check whether the Random Walk and Signal Calculation blocks were able to correctly reproduce and measure the expected parameters. For this test I simulated a random walk of 10.000 particles diffusing freely inside a blank box. The dimensions of the box were chosen large enough ($L = 1000 \mu\text{m}$) to provide that the particles, initially placed in its middle, would not "feel" the walls.

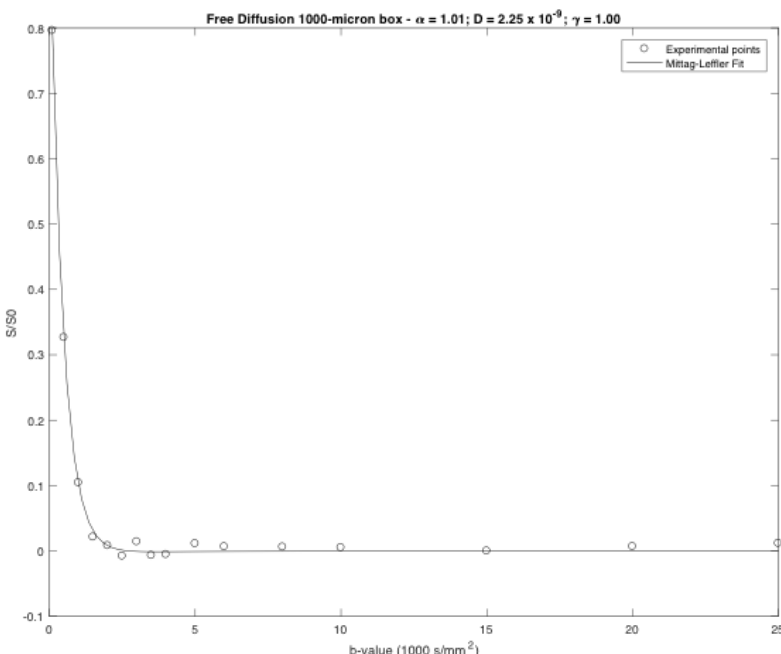


Figure 12: First test of the program: simulation of free diffusion.

The above graph shows that the program correctly simulated the free random walk and correctly calculated the signal decay (fitted here with the Mittag-Leffler relation eq. 3.8). Indeed, the fitted parameters ($\alpha = 1.01$, $\gamma = 1.00$ and $D = 2.25 \times 10^{-9}$) match almost perfectly the expected ones ($\alpha = 1.00$, $\gamma = 1.00$ and $D = 2.30 \times 10^{-9}$).

The second test concerned the simulation of restricted diffusion. The idea was to use a reasonably small box ($L = 50 \mu\text{m}$) and long diffusion time (124.4 ms) to check whether the Random Walk and Signal Calculation blocks were able to reproduce the expected diffraction patterns.

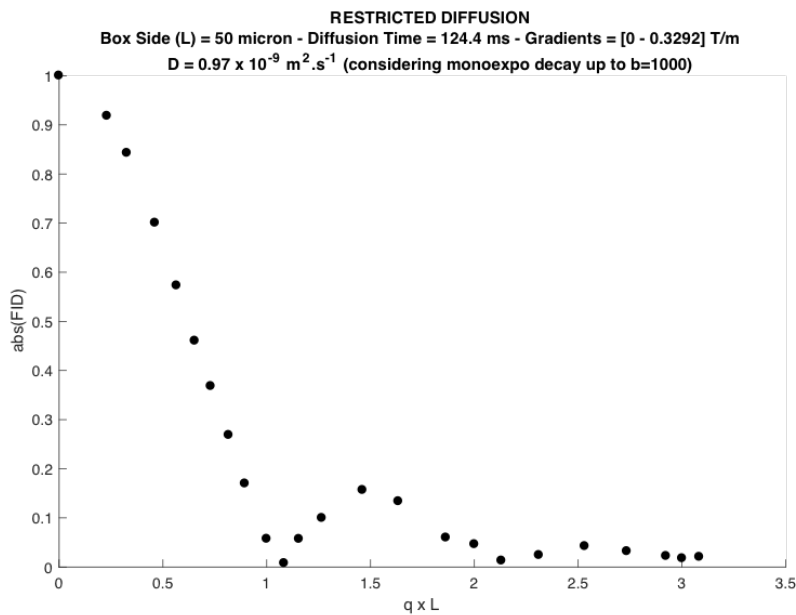


Figure 13: Second test of the program: simulation of restricted diffusion.

Using 24 gradients in the range [0 - 0.3292] T/m, I plotted the absolute value of the FID signal as dependent on the dimensionless quantity $q \times L$ (that is, the magnitude of the vector $\vec{q} = \gamma \delta \vec{g}/2\pi$ times the relevant length, i.e., the box side L). As can be seen above, the graph neatly reproduces the diffraction pattern with minima on integers values of qL (for comparison, similar examples can be found on (9) (page 311) and (23)).

The results of the tests reassure us that the program works as projected.

Chapter 4

Simulation of mono-dispersed spheres

This chapter concerns the simulation of diffusion in systems consisting of randomly dispersed microscopic spheres. The main motivation for this part of the thesis was to deepen the understanding of the experimental results found in similar physical systems studied by the NMR group from the University of Rome (12). Naturally, the simulated parameters were chosen to be as close as possible to the experimental ones. As for the mathematical model used to study signal decay, however, I did not restrict myself to the one most often employed by the group, namely, the Stretched Exponential model. Thus, a second motivation for the present simulations was to make a comparison between it and another one - the Mittag-Leffler model.

4.1 The models

Two models are employed in the simulations: the Mittag-Leffler and the Stretched Exponential. In the next two subsections both are explained.

4.1.1 The Mittag-Leffler

The CTRW theory predicts that the solution (Fourier transformed in q-space) of the fractional diffusion equation with time and space coefficients respectively α and β is in the form of a 1-parameter Mittag-Leffler function (cf. eq. 1.52):

$$p(q,t) = E_\alpha(-D_{\alpha,\beta} |q|^\beta t^\alpha), \quad (4.1)$$

where E_α stands for the 1-parameter Mittag-Leffler function of the form

$$E_\alpha(z) = \sum_{k=1}^{\infty} \frac{(z)^k}{\Gamma(\alpha k + 1)}, \quad (4.2)$$

q is the magnitude of the vector $\gamma\delta\vec{g}/2\pi$, and t is the diffusion time, here defined as $t = \Delta - \delta/3$.

In order to fit the experimental points to this equation, I used a transformed expression of the equation 4.1. As we will see, the advantage of using the new form is that

the diffusion coefficient D is expressed in integer units in it. Its derivation was done in (24), from which I quote extensively in the following.

Equation 4.1 can be written as

$$p(q,t) = E_\alpha \left(-D_{1,2} \frac{\tau^{1-\alpha}}{\mu^{2-2\gamma}} |q|^{2\gamma} t^\alpha \right), \quad (4.3)$$

where $D_{1,2}$ is the nominal diffusion coefficient (in m^2/s), and μ and τ are spatial and temporal parameters that are needed to preserve the nominal units of the diffusion coefficient. By substituting q^2 with b/t ($b = q^2(\Delta-\delta/3) = q^2t$), equation 4.3 can be written as

$$p(q,t) = E_\alpha \left(-D_{1,2} \frac{\tau^{1-\alpha}}{\mu^{2-2\gamma}} b^\gamma t^{(\alpha-\gamma)} \right). \quad (4.4)$$

If we define the γ^{th} power of a newly defined diffusion coefficient as

$$D^\gamma = D_{1,2} \frac{\tau^{1-\alpha}}{\mu^{2-2\gamma}} t^{(\alpha-\gamma)}, \quad (4.5)$$

then we can further simplify eq. 4.4:

$$p(q,t) = E_\alpha \left(- (b D)^\gamma \right). \quad (4.6)$$

This is the equation I used to fit the signal decay and to estimate the three parameters (α , γ and D). The advantage of this new form lies on the fact that it retains integer units for the diffusion coefficient, thereby making it apt for comparison with the analogous coefficient obtained in mono-exponential fits. However, it also bears the disadvantage that only one of the relevant parameters (gradient or time) can be varied at a time. I used this equation with variation of the gradient strength and kept the diffusion time fixed in all simulations¹⁰.

4.1.2 The Stretched Exponential

The second model used to fit the simulated signal decay can also be said to have the CTRW theory as a fundament. We depart from the same expression for the fractional diffusion equation, eq. 4.1, but assume that $\alpha = 1$. In this case eq. 4.6 turns into an exponential function of the form¹¹

¹⁰ Since one of the goals was to compare the models and since the Stretched Exponential model only has the parameters D and γ , the present study was less concerned with α .

¹¹ Equations 4.6 and 4.7 assume the probability $p(q,t)$ to be normalized.

$$p(q,t) = e^{-(bD)^{\gamma}}. \quad (4.7)$$

This is the model equation and as can be seen it has two parameters (D and γ). The assumption on which it is based, namely that $\alpha = 1$, is justified as long as we can assume the diffusion process to be characterized by a finite mean waiting time (see 1.4.2 above). This seems to hold in the case of the present group of simulations, i.e., systems comprising spheres of equal diameter ("mono-dispersed spheres"), since equal diameters would produce a narrow distribution of pore sizes and this in turn would imply that residence times - i.e. waiting times - are narrowly distributed (12). Again, we see that the equation is written in terms of the b -value and that the diffusion coefficient is in integer units.

4.2 The 'big picture': first simulations and the Mittag-Leffler model

The simulations on this chapter aimed at emulating the physical systems studied in a number of papers from the University of Rome Group and eminently in (12). The systems consist of microscopic spheres of equal diameter randomly dispersed in water at different concentrations. On the present section I specifically report the results from experiments with spheres of 5 different diameters (6, 10, 15, 20 and 30 μm) and in 4 packing ratios (40, 50, 60 and 70%), totalizing 20 different configurations. The results allow us some first, general conclusions and, for that reason, I call it "the big picture". Remark that only the Mittag-Leffler model is used on this section. Afterwards, on section 4.3 we will restrict our analysis to only two sphere-diameters in order to pin-point differences between the two mathematical models (see 4.1).

4.2.1 Simulation setup

The simulations on this section comprise systems of microscopic spheres of equal diameter randomly placed inside a cubic space ("the box"). The Random Walk Block of the program simulates water diffusion in the interstices between the spheres¹². Each simulated configuration comprised spheres of one of 5 different diameters (6, 10, 15, 20 and 30 μm) and in one of 4 packing ratios, or densities (40, 50, 60 and 70%). There were thus 20 different configurations.

As seen on 3.1.2, the Random Walk Block creates trajectories restricted to a central area comprising 60% of the box volume, thereby avoiding simulating trajectories in regions subject to wall effects on the packing. Since I did not use the entire volume, but only that central region, I had to calculate the effective packing on the volume available for the trajectories. As a result, there are slight differences between the nominal packings and the effective packings that were used. So, when reference is made to the 40, 50, 60 and 70% configurations, it should be borne in mind that the effective packings were in fact 39, 49, 60 and 72%.

As for the NMR parameters, the simulations use in principle the exact settings of (12), that is, a PGSE sequence with parameters $\Delta/\delta = 80/4.4$ ms and $B_0 = 9.4$ T. However, I deliberately decided to use very high diffusion-weighting gradients in order to take full advantage of the ability of the Mittag-Leffler model to fit high b-values (more on this on 4.3.4). As already commented, in all simulation in this thesis, the gradient is the only quantity in the b-value that is varied (diffusion time is constant). Each simulated experiment

¹² The spheres comprise the so-called "solid matrix".

was carried out with 16 b-values (100, 500, 1.000, 1.500, 2.000, 2.500, 3.000, 3.500, 4.000, 5.000, 6.000, 8.000, 10.000, 15.000, 20.000 and 25.000 s/mm²) and the respective NMR signal was calculated for a number of trajectories $\sim O(10^4)$.

Simulated experiments were carried out for every one of the 20 configurations of spheres (5 diameters \times 4 packing ratios) and for every one of the three gradient directions (x , y and z). For every experiment signal decay was computed with and without the contribution of internal gradients due to the difference of susceptibility ($\Delta\chi$) between water and the solid matrix (set to 0.1 ppm in all simulations) and the corresponding parameters D , α and γ were then obtained after the fitting routine described on 4.1.1. Having obtained the values of the parameters for the three directions (e.g., α_x , α_y and α_z), I then calculated their mean ($\alpha = 1/3 \sum_{i=x,y,z} \alpha_i$). On the next subsection I report those mean values, discriminated by packing ratio and sphere diameter.

4.2.2 Results¹³

Table 4.1: Parameters without internal gradient computation

φ (%)	Diameter (μm)	D ($\times 10^{-9} \text{ m}^2/\text{s}$)	α	γ
70	6	0.66	1.22	1.06
70	10	0.93	0.80	1.08
70	15	0.95	0.54	1.00
70	20	0.99	0.38	1.00
70	30	1.00	0.37	1.04

φ (%)	Diameter (μm)	D ($\times 10^{-9} \text{ m}^2/\text{s}$)	α	γ
60	6	0.85	1.25	1.09
60	10	1.32	1.01	1.04
60	15	1.35	0.83	1.03
60	20	1.35	0.65	1.03
60	30	1.15	0.80	0.92

¹³ The error estimates reported for next section's data refer to the sample standard deviation calculated over 6 experiments for each parameter. The present section's data however concerns a much larger set of configurations. In order to reduce total simulation time and since we are only interested here in grasping general tendencies displayed by the material, in particular, in face of the presence or absence of internal gradients, I ran only one experiment for each configuration and gradient direction. This is the reason why only in this section error estimates are not provided (see 4.3.2 and 4.3.3 below for further details)

φ (%)	Diameter (μm)	D ($\times 10^{-9} \text{ m}^2/\text{s}$)	α	γ
50	6	0.93	1.20	1.10
50	10	1.47	0.91	1.06
50	15	1.53	0.92	1.00
50	20	1.57	0.95	0.98
50	30	1.71	0.94	1.01

φ (%)	Diameter (μm)	D ($\times 10^{-9} \text{ m}^2/\text{s}$)	α	γ
40	6	1.13	1.24	1.10
40	10	1.71	1.00	1.06
40	15	1.76	0.94	1.02
40	20	1.75	0.92	1.01
40	30	1.79	0.93	1.01

Table 4.2: Parameters with internal gradient computation

φ (%)	Diameter (μm)	D ($\times 10^{-9} \text{ m}^2/\text{s}$)	α	γ
70	6	0.67	1.22	1.05
70	10	0.97	0.84	0.99
70	15	1.03	0.68	0.84
70	20	1.13	0.58	0.78
70	30	1.06	0.88	0.61

φ (%)	Diameter (μm)	D ($\times 10^{-9} \text{ m}^2/\text{s}$)	α	γ
60	6	0.86	1.25	1.08
60	10	1.37	1.02	0.98
60	15	1.46	0.88	0.91
60	20	1.52	0.77	0.82
60	30	1.43	0.93	0.64

φ (%)	Diameter (μm)	D ($\times 10^{-9} \text{ m}^2/\text{s}$)	α	γ
50	6	0.94	1.20	1.09
50	10	1.49	0.93	1.02
50	15	1.57	0.95	0.94
50	20	1.66	0.98	0.90
50	30	1.88	0.97	0.89

φ (%)	Diameter (μm)	D ($\times 10^{-9} \text{ m}^2/\text{s}$)	α	γ
40	6	1.13	1.24	1.09
40	10	1.74	1.00	1.04
40	15	1.82	0.95	0.97
40	20	1.85	0.95	0.92
40	30	1.98	0.97	0.85

The data for alpha and gamma are gathered on the four pictures bellow - the first two for the values of alpha (without and with internal gradient computation) and the other two for the values of gamma (without and with internal gradient).

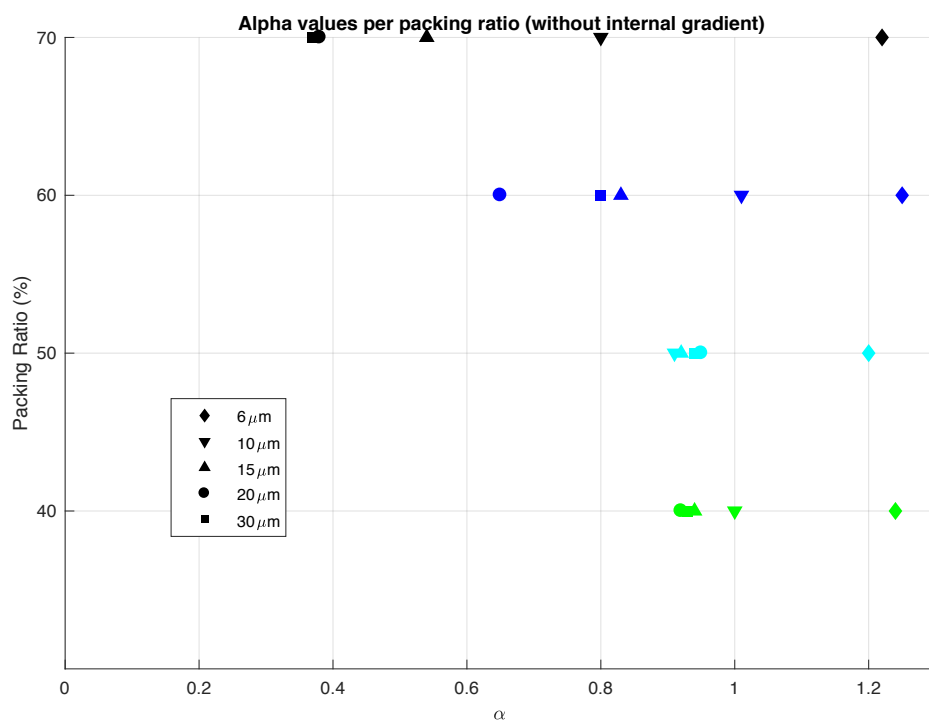


Figure 14: ALPHA (without internal gradient)

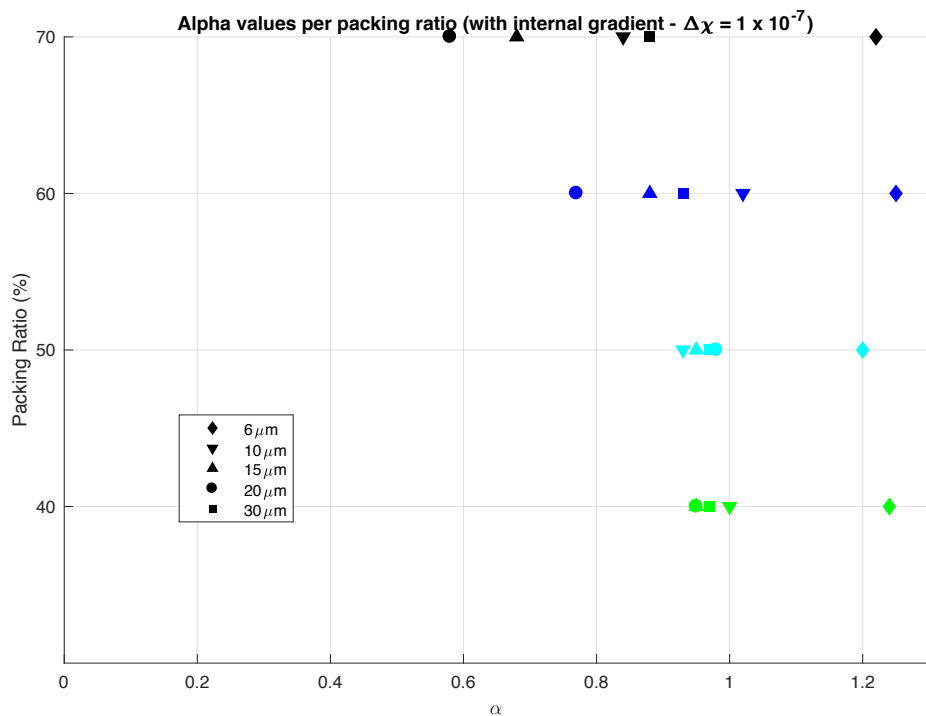


Figure 15: ALPHA (with internal gradient)

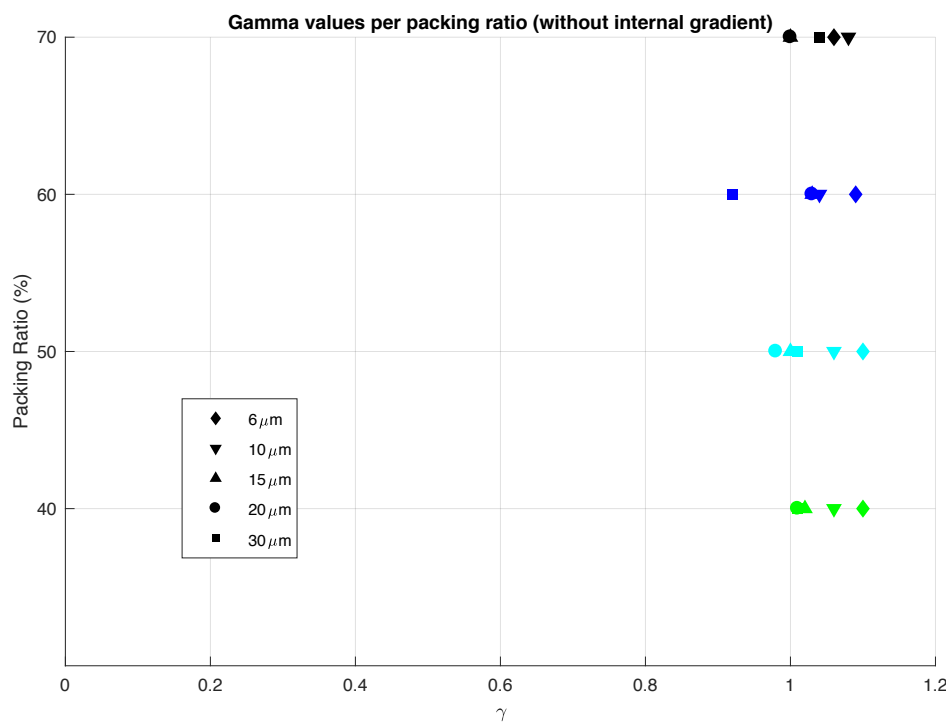


Figure 16: GAMMA (without internal gradient)

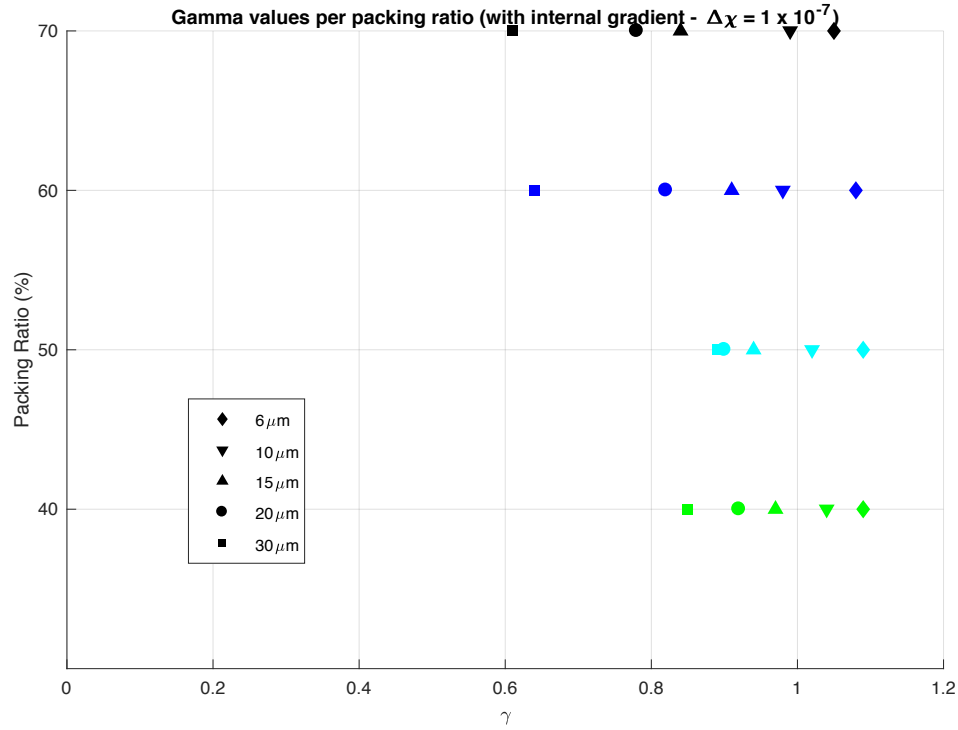


Figure 17: GAMMA (with internal gradient)

4.2.3 Discussion

We intend to use the CTRW apparatus to study anomalous diffusion. According to that model, one of the anomalous diffusion regimes (sub- or superdiffusive) is to be expected when $0 < \alpha < 1$ and/or $0 < \gamma < 1$. As is readily seen on the graphs, values of alpha and gamma above unity were not uncommon. But, with the exception of the 6 μm -spheres' alphas, the parameters were never more than 10% above unity. Since 1) those higher values may convey specific information about a given geometry; 2) limiting beforehand the values may introduce bias in the fitting routine; and 3) it is, in any case, the ratio α/γ that determines the diffusive regime, I decided that the fitting routine should not put any cap on the parameters

The parameter α is barely affected by the presence of internal gradients as can be especially appreciated on the two less dense configurations (40 and 50%). This result is in agreement with the experimental evidence reported on (12).

Instead, the effect of internal gradients on the parameter γ is remarkable. Overall, when no internal gradient is computed, all configurations display gammas in the interval of -10% / +10% around unity, which makes them practically indistinct as far as the gamma coefficient is concerned. However, when the effect of internal gradients is computed, there is an overall decrease in the values of gamma, the decrease ranging from less than 1% in configurations with smaller spheres and lower packings, and up to 40% in configurations with larger spheres and in the highest packings. Two important conclusions can be ascertained. First, the anomaly of the space parameter (i.e., $\gamma < 1$) is in practice completely due to the effect of internal gradients. This conclusion is in full agreement with the experimental evidence reported on (12). Second, the internal gradients also have the effect of increasing the spread in the values of gamma among the different configurations with equal packing, thus enabling us to better discriminate between different configurations.

4.3 Detailed analysis of a limited range: model comparison

On section 4.2 we did a first, exploratory study of the spheres' configurations using b-values in the range [100 - 25.000 s/mm²] and a model that is especially suited for very high gradients - the Mittag-Leffler (see subsection 4.3.4 below). However, b-values above 10.000 s/mm² are not frequent in the scientific literature and are still rarer in the medical practice. That is why we turn our attention to experiments with lower gradients in this section and take the opportunity to compare the performance of the two models - the Mittag-Leffler and the Stretched Exponential - in this gradient range. Also, the idea is to restrict the analysis to only two sphere diameters - 5 and 10 micron - since these are the average diameters of brain cells that are presently the subject of research by the University of Rome's NMR group.

4.3.1 Simulation setup

In this second group of simulations we focus on only two sphere diameters: 5 and 10 μm . However we extend the previous analysis in two ways: by adding new packing ratios in the range [45 - 75%] and by taking the average over different sample spaces. As far as the packing ratios are concerned, I used the 7 values 45, 50, 55, 60, 65, 70 and 75%. As for the different samples, I did the following: for each packing ratio three sample spaces - i.e. boxes with 500 spheres randomly dispersed in the selected packing - were generated. For each configuration studied (i.e. a given sphere in a given packing) 6 experiments/simulations were done: two in each sample space. And after computation of the parameters' average for each sample space, the values for the three sample spaces were then averaged to provide the final values for the given configuration sphere/packing.

Like the precedent subsection's simulations, the present ones also use the NMR parameters of (12), that is, a PGSE sequence with parameters $\Delta/\delta = 80/4.4$ ms and $B_0 = 9.4$ T. Each simulated experiment was carried out with 17 b-values (10, 30, 60, 100, 200, 400, 700, 1.000, 1.500, 2.000, 3.000, 4.000, 5.000, 6.000, 8.000, 10.000 and 12.000 s/mm²). Again, the gradient is the only quantity in the b-value to be varied (diffusion time is kept constant). In each experiment the NMR signal was calculated for 1.000 trajectories.

Simulated experiments were carried out for every one of the 14 configurations of spheres (2 diameters \times 7 packing ratios) this time only for gradient direction x. For every experiment signal decay was computed with and without the contribution of internal gradients due to the difference of susceptibility ($\Delta\chi$) between water and the solid matrix (set again to 0.1 ppm in all simulations). The Mittag-Leffler parameters D, α and γ were obtained after the fitting routine described on 4.1.1 and the Stretched Exponential parameters D and γ were obtained after the fitting routine described on 4.1.2.

4.3.2 Mittag-Leffler results¹⁴ and comments

Table 4.3: Parameters for 5-micron-spheres

ALPHA		
Packing (%)	Without Int. Grad.	With Int. Grad.
75	1.18 ± 0.07	1.18 ± 0.07
70	1.23 ± 0.05	1.23 ± 0.05
65	1.26 ± 0.01	1.25 ± 0.01
60	1.28 ± 0.01	1.28 ± 0.01
55	1.27 ± 0.02	1.27 ± 0.02
50	1.28 ± 0.06	1.28 ± 0.06
45	1.25 ± 0.03	1.25 ± 0.03

GAMMA		
Packing (%)	Without Int. Grad.	With Int. Grad.
75	1.04 ± 0.03	1.03 ± 0.03
70	1.05 ± 0.01	1.04 ± 0.01
65	1.05 ± 0.03	1.04 ± 0.03
60	1.04 ± 0.01	1.04 ± 0.01
55	1.05 ± 0.02	1.04 ± 0.02
50	1.06 ± 0.02	1.05 ± 0.02
45	1.05 ± 0.02	1.05 ± 0.02

D ($10e-9 m^2 s^{-1}$)		
Packing (%)	Without Int. Grad.	With Int. Grad.
75	0.44 ± 0.01	0.45 ± 0.01
70	0.53 ± 0.02	0.53 ± 0.02
65	0.57 ± 0.05	0.57 ± 0.05
60	0.63 ± 0.02	0.64 ± 0.02
55	0.64 ± 0.01	0.65 ± 0.01
50	0.73 ± 0.06	0.73 ± 0.07
45	0.76 ± 0.03	0.77 ± 0.03

Ratio ALPHA / GAMMA		
Packing (%)	Without Int. Grad.	With Int. Grad.
75	1.13 ± 0.07	1.15 ± 0.08
70	1.17 ± 0.05	1.18 ± 0.05
65	1.20 ± 0.04	1.20 ± 0.04
60	1.23 ± 0.02	1.23 ± 0.02
55	1.21 ± 0.03	1.22 ± 0.03
50	1.21 ± 0.06	1.22 ± 0.06
45	1.19 ± 0.04	1.19 ± 0.04

¹⁴ A note about error estimates. For every configuration studied (i.e. a given diameter in a given packing), three simulation spaces were created and, in every space, two simulations were run. The results of these two runs were averaged to provide the values of alpha, gamma and D for the space. Finally, from the values for the three spaces, the mean and the sample standard deviation were computed to provide respectively the values and the error estimates here reported. As for the error estimates of the quantity alpha/gamma, having assumed that the individual errors of alpha and gamma are independent, I was able to use the formula: $\Delta R = R \sqrt{\left(\frac{\Delta\alpha}{\alpha}\right)^2 + \left(\frac{\Delta\gamma}{\gamma}\right)^2}$, where R is the quantity $\frac{\alpha}{\gamma}$ and $\Delta(\cdot)$ stands for the error associated to a given parameter.

Table 4.4: Parameters for 10-micron-spheres

ALPHA		
Packing (%)	Without Int. Grad.	With Int. Grad.
75	0.77 ± 0.04	0.83 ± 0.02
70	0.81 ± 0.09	0.85 ± 0.07
65	0.71 ± 0.12	0.75 ± 0.10
60	0.96 ± 0.07	0.98 ± 0.07
55	0.97 ± 0.05	0.98 ± 0.05
50	1.00 ± 0.08	1.01 ± 0.06
45	1.02 ± 0.02	1.03 ± 0.01

GAMMA		
Packing (%)	Without Int. Grad.	With Int. Grad.
75	1.06 ± 0.04	0.95 ± 0.05
70	1.03 ± 0.02	0.95 ± 0.04
65	1.09 ± 0.02	1.03 ± 0.02
60	1.05 ± 0.02	0.99 ± 0.05
55	1.06 ± 0.02	1.02 ± 0.02
50	1.04 ± 0.01	1.00 ± 0.01
45	1.02 ± 0.00	0.99 ± 0.01

D (10e-9 m^2s^-1)		
Packing (%)	Without Int. Grad.	With Int. Grad.
75	0.75 ± 0.08	0.74 ± 0.08
70	0.89 ± 0.15	0.88 ± 0.15
65	1.18 ± 0.03	1.18 ± 0.06
60	1.36 ± 0.08	1.39 ± 0.08
55	1.38 ± 0.04	1.40 ± 0.04
50	1.53 ± 0.14	1.55 ± 0.14
45	1.55 ± 0.09	1.56 ± 0.10

Ratio ALPHA / GAMMA		
Packing (%)	Without Int. Grad.	With Int. Grad.
75	0.73 ± 0.05	0.87 ± 0.05
70	0.79 ± 0.09	0.89 ± 0.08
65	0.65 ± 0.11	0.73 ± 0.10
60	0.91 ± 0.07	0.99 ± 0.09
55	0.92 ± 0.05	0.96 ± 0.05
50	0.96 ± 0.08	1.01 ± 0.06
45	1.00 ± 0.02	1.04 ± 0.01

Next, I highlight some relevant points about the results.

1) ALPHA

For 5-micron spheres, alpha remains practically at the same level (around 1.20^{15}) in all packing configurations. Also, comparing the values obtained with and without the

¹⁵ A note about fitting. Two relevant features of the protocol adopted for the fitting procedures in this thesis are: 1) there was no cap to the values that model parameters can assume. Doing otherwise would mean to presume an artificial range for the parameters. Thus, alpha and gamma may eventually be greater than one (as in the present case), a fact which is in no way in disagreement with the CTRW theory; 2) I did not use a specific routine to make the initial guesses at the parameters' values (a necessary input for the least squares fitting routine). Instead they were chosen to be the same for all configurations whenever possible. As a matter of fact I observed that even very

contribution of internal gradients, we note that the spread between those values was minimal (never above one percentage point), which shows that the parameter was barely affected by the presence of internal gradients (figure 18).

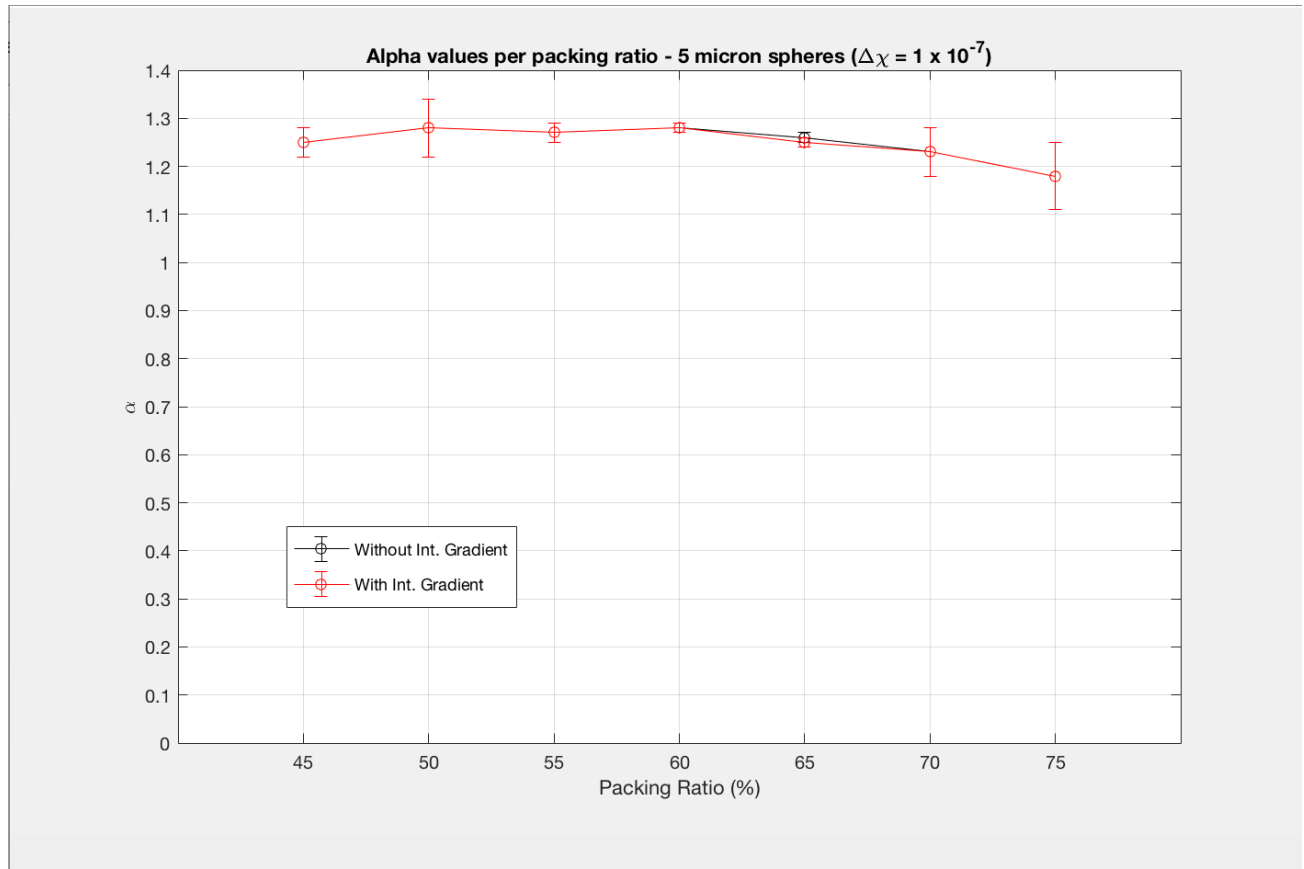


Figure 18: Parameter Alpha for 5-micron spheres

For 10-micron spheres, however, there is a marked difference in the parameter's behavior depending on packing ratio. Thus for packings in the range [45 - 60%] alpha's values display a slight decrease, if any, its values remaining very close to unity. In the densest range ([65 - 75%]), however, alpha falls abruptly to values decisively lower than 0.9 (considering error). Moreover, there seems to be a discontinuity at 65%. Another difference in relation to 5-micron spheres is that the effect of internal gradients is conspicuously felt. Alpha values are higher in the presence of internal gradients, the spread increasing, with increasing packing, from 1 to 6 percentage points (figure 19).

different choices of initial values produced identical results or almost. However the choice of initial values was not (and cannot be, for a fact) completely free. Usually the fitting routine converged only when the initial guesses were on the order of magnitude of the output values.

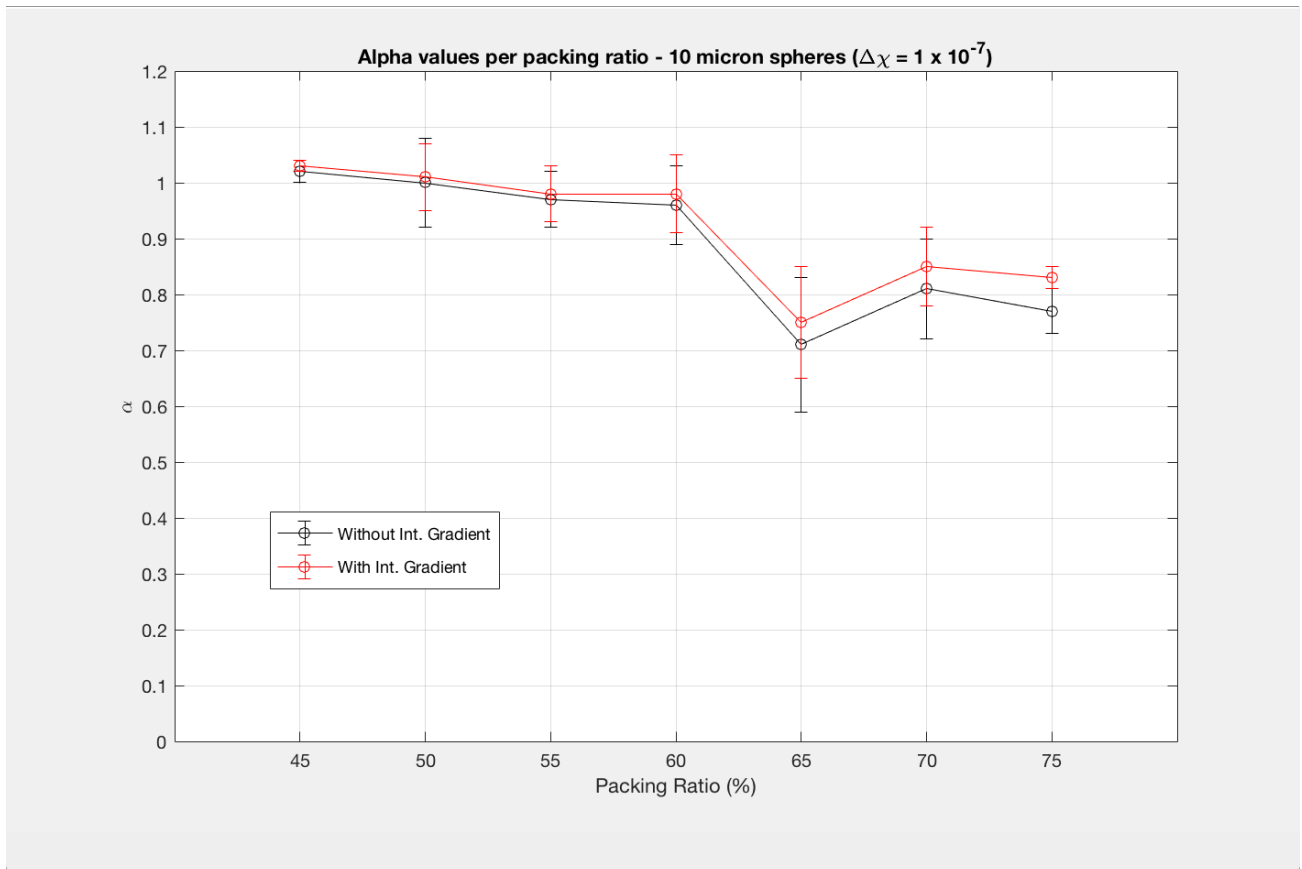


Figure 19: Parameter Alpha for 10- micron spheres

2) GAMMA

For 5-micron spheres, gamma remains practically at the same level (close to unity) in all packing configurations. Also, comparing the values obtained with and without the contribution of internal gradients, we note that the spread between those values was minimal (never above one percentage point), which shows that the parameter was barely affected by the presence of internal gradients (figure 20)

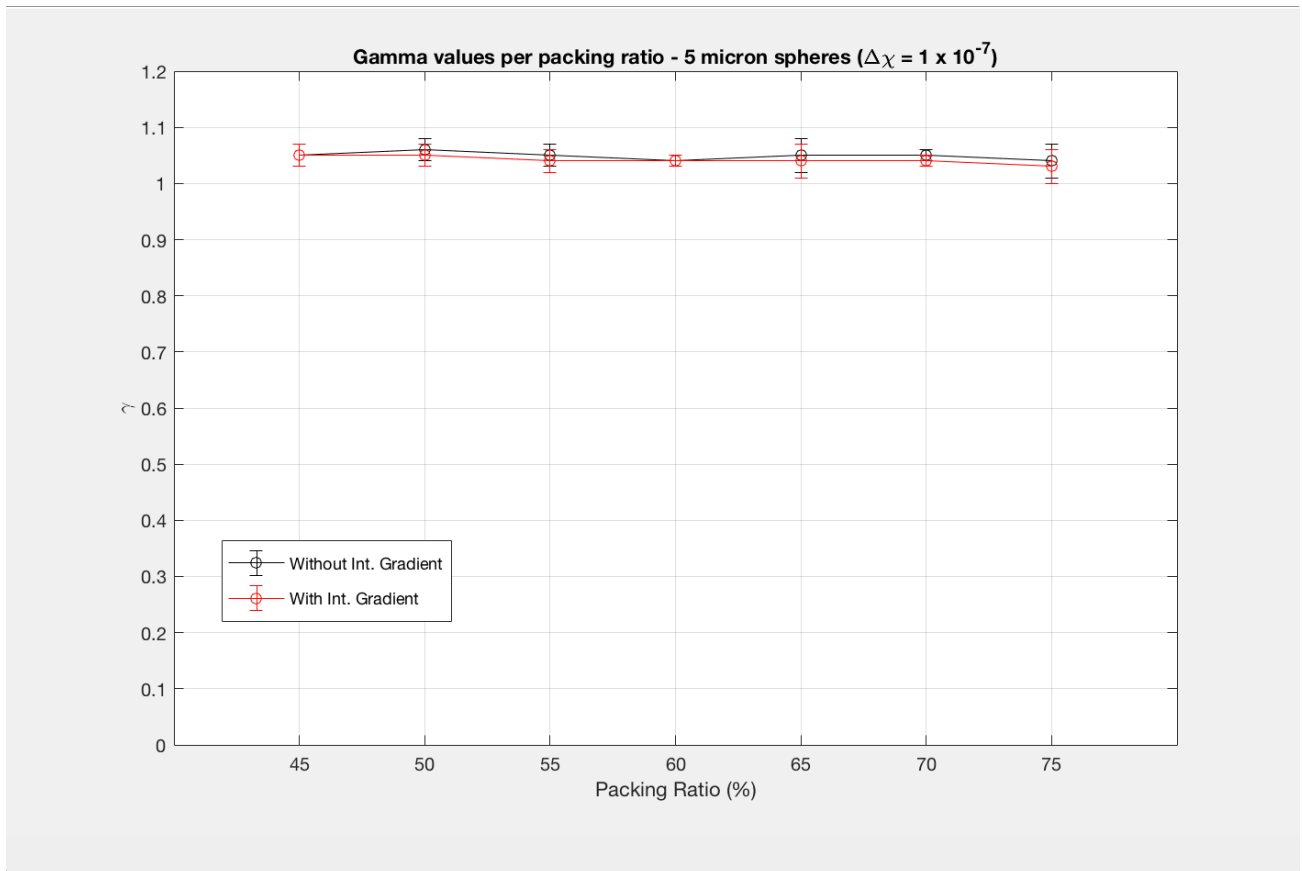


Figure 20: Parameter Gamma for 5-micron spheres

For 10-micron spheres, the parameter remains basically leveled between 1 and 1.1. The spread between values with and without internal gradient computation seems to grow (from 3 to 11 percentage points) with increasing packing (figure 21).

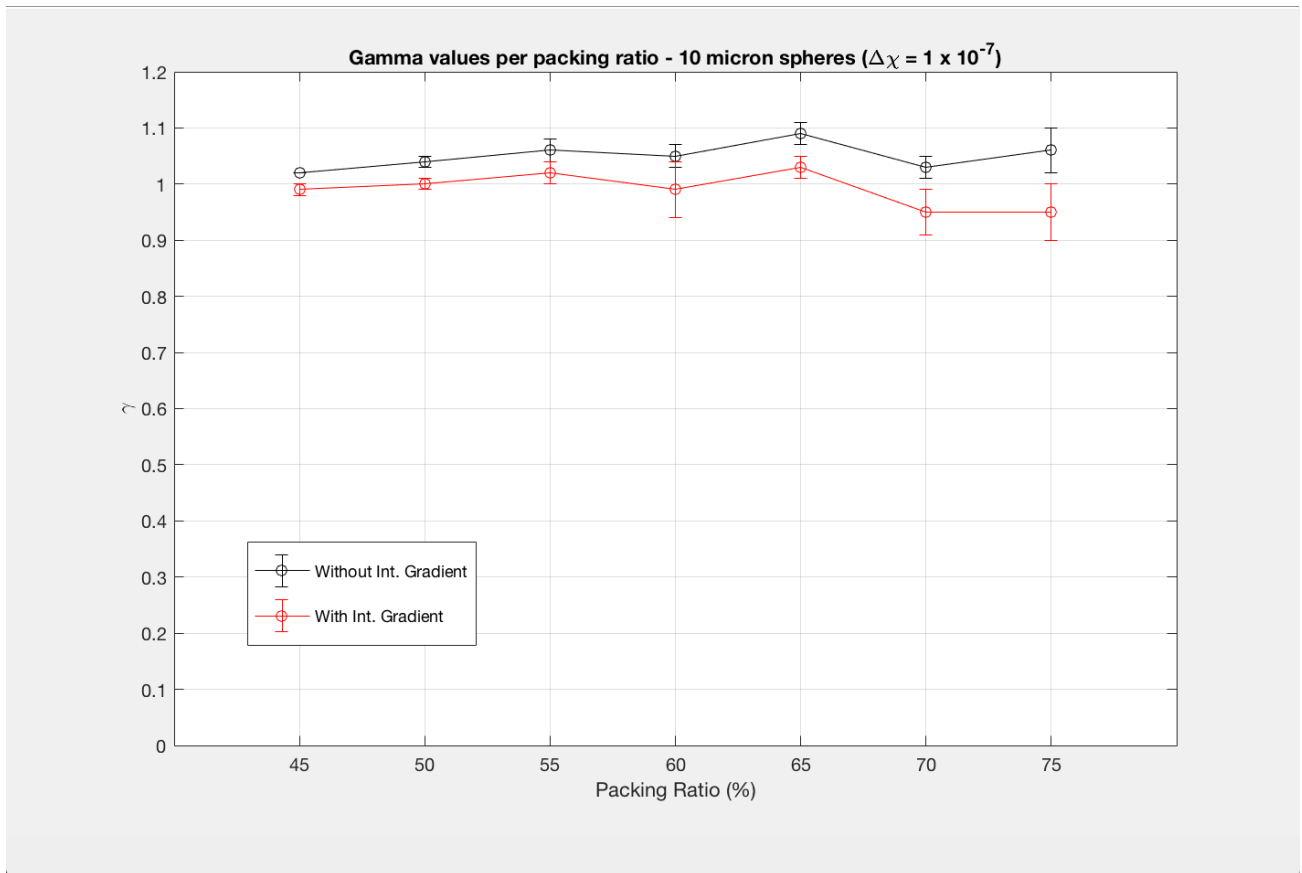


Figure 21: Parameter Gamma for 10-micron spheres

3) D

The parameter D is what we can term the model's generalized diffusion coefficient. Here two remarks can be made and they are valid for both sphere diameters. First, note that the parameter is barely affected by the presence of internal gradients (figures 22 and 23). Second, D decreases monotonically with increasing packing and has higher values overall in configurations of 10-micron spheres. The parameter seems to behave exactly as expected: it is higher in regions with larger pores and smaller in regions with smaller pores.

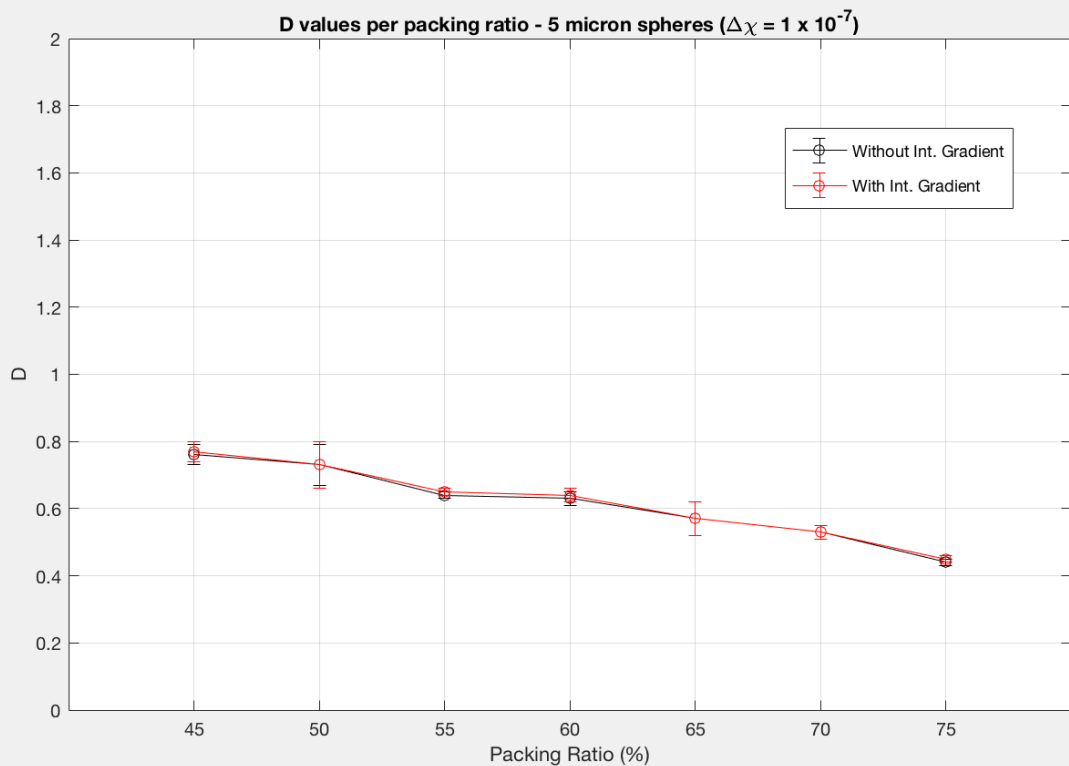


Figure 22: Parameter D for 5-micron spheres

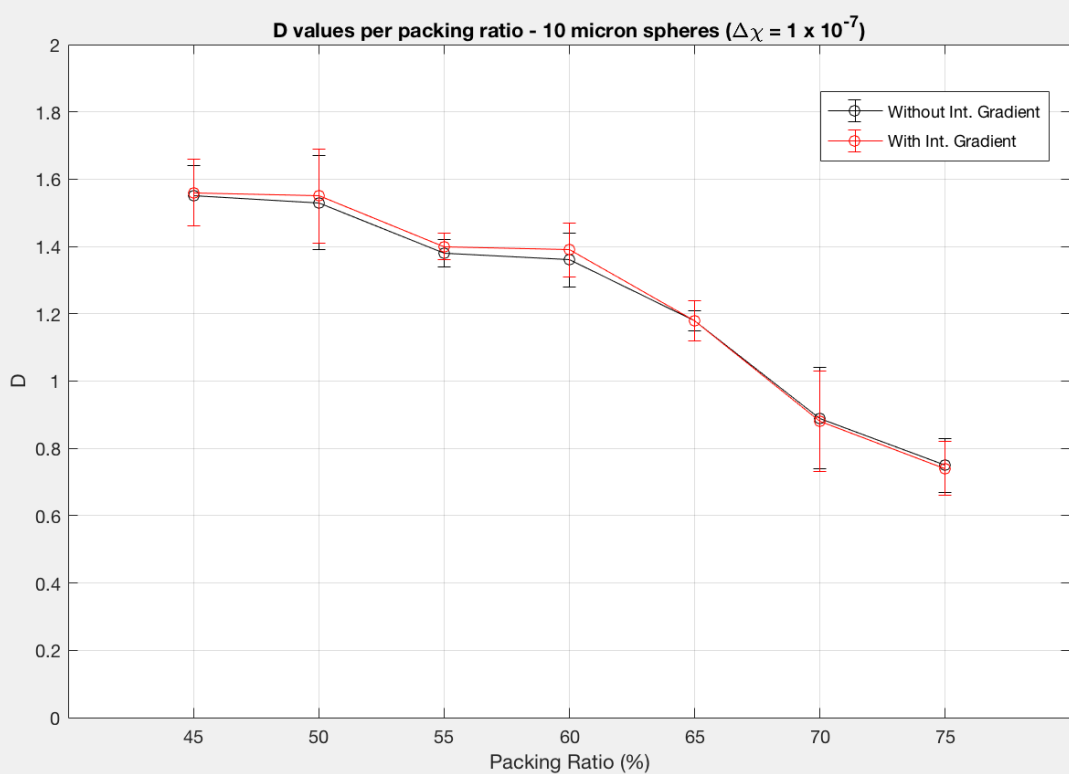


Figure 23: Parameter D for 10-micron spheres

4) RATIO ALPHA/GAMMA

Since in the most general case the diffusive properties of the process studied depend on α/γ (cf. subsection 1.4.3, eq. 1.54)¹⁶ and not on alpha or gamma individually, it is worthwhile to extend the analysis to the ratio¹⁷.

For 5-micron spheres, alpha/gamma displays a flat profile (more often in the range 1.1 - 1.2) in all packing configurations (although a gradual decrease in packings above 60% cannot be ruled out). The values obtained with and without the contribution of internal gradients show again almost no difference (figure 24).

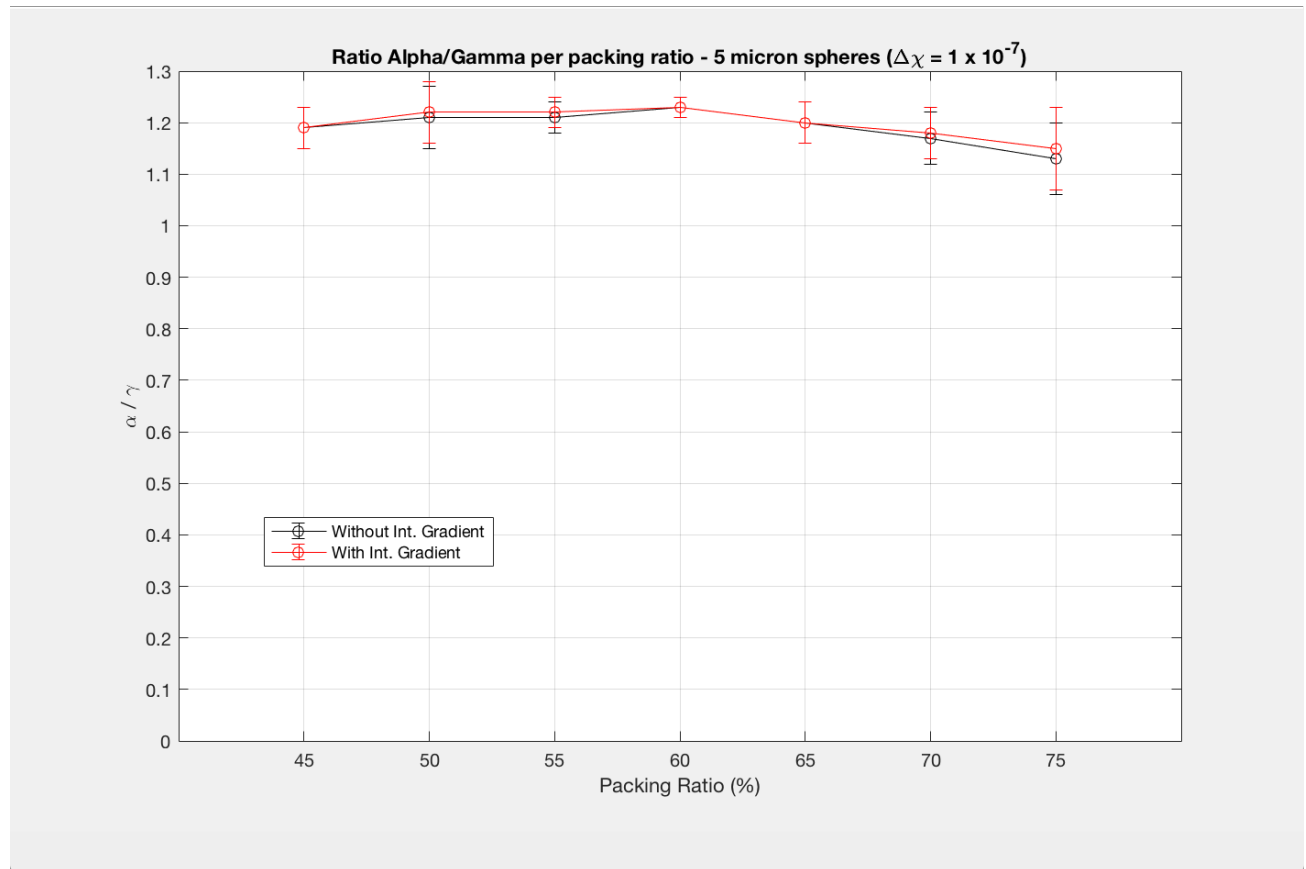


Figure 24: Ratio alpha/gamma for 5-micron spheres

According to the commentary to eq. 1.54 (subsection 1.4.3), the fact that 5-micron spheres present values of alpha and gamma everywhere greater than one (figures 18 and 20 above) means that the underlying process we are observing is normal (or Brownian) diffusion (figure 25).

¹⁶ Recall that $\gamma = \mu/2$.

¹⁷ To my knowledge this is the first time that such an analysis is carried out.

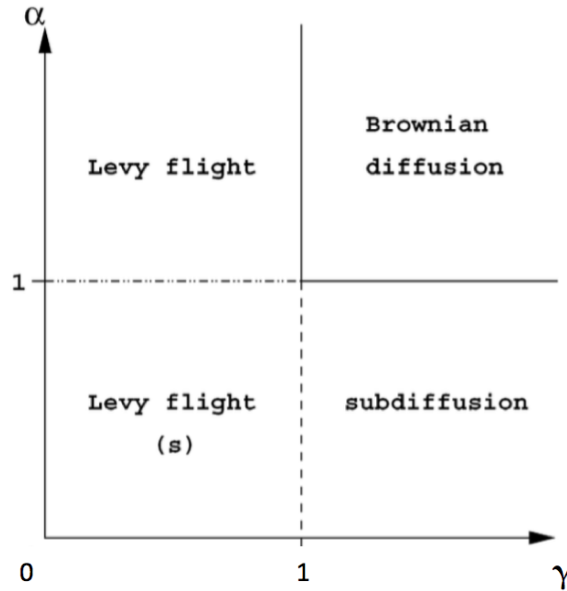


Figure 25: Phase diagram characterizing the four domains which can be distinguished according to diverging or finite characteristic waiting time and jump length variance (adapted from (2)).

It means that the pores created by packings of 5-micron spheres are perhaps so small, that the statistics of water diffusion is not affected by the variation of packing ratio in the range 45 - 75%. Diffusion in all studied configurations of 5-micron spheres should be described by Gaussian statistics, the only difference being the rate of the process, i.e., the magnitude of the diffusion coefficient. In fact, as seen on figure 22 above, there is a decrease in D with increasing packing.

For 10-micron spheres, α/γ displays a distinctive profile, which resembles closely that of α , that is, a gradual decrease in the 45 - 60% range and an accelerated decrease in the 65 - 75% range, with a discontinuity on 65%. If we recall that γ is practically flat (figure 21 above), it is likely that the parameter α dominates and determines the process' general form.

Moreover, if we observe the values without internal gradient computation (black line on figure 26 below) and recall that 10-micron spheres have $\alpha \geq 1$ only on 45 e 50%, $\gamma \geq 1$ everywhere and $\alpha/\gamma < 1$ everywhere but on 45%, we can conclude that the underlying process is subdiffusive in the range 55 - 75% and normal on 45 e 50%.

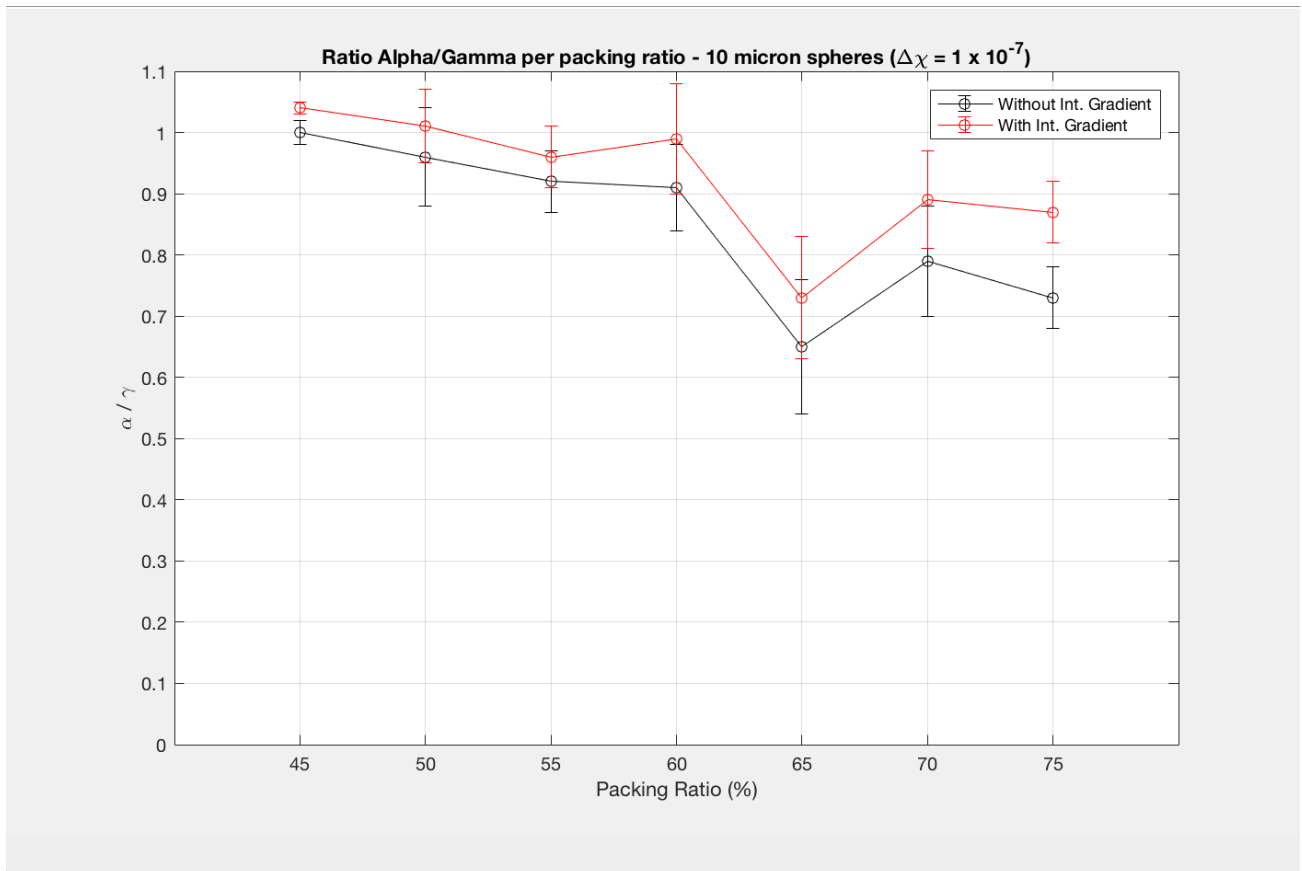


Figure 26: Ratio alpha/gamma for 10-micron spheres

Turning now our attention to the values calculated with internal gradients (red line on figure 26), we observe that the contribution of internal gradients tends to raise the ratio alpha/gamma, the spread being greatest in the densest packings. Also, recalling that the values of the respective parameters alpha and gamma are smaller than one on the packings 60, 70 and 75%, we observe that on these packings the diffusive dynamics would be defined, in the words of Metzler and Klafter (2), as a non-Markovian Lévy flight dominated by localisation (or waiting) events. Finally, on 45% something curious happens. Since only on this packing ratio $\alpha > 1$ and $\gamma < 1$, we observe that a superdiffusive process takes place. Since without the contribution from internal gradients the process is rather normal on 45%, this superdifusivity is a sort of artifact produced by the internal gradients. Thus, using the words of the University of Rome NMR Group (12), the process here can be named a 'pseudo-superdiffusion'.

4.3.3 Stretched-Exponential results and comments

Table 4.5: Parameters for 5-micron-spheres

GAMMA		
Packing (%)	Without Int. Grad.	With Int. Grad.
75	1.13 ± 0.03	1.11 ± 0.04
70	1.13 ± 0.02	1.11 ± 0.03
65	1.08 ± 0.02	1.07 ± 0.02
60	1.12 ± 0.02	1.10 ± 0.02
55	1.11 ± 0.05	1.10 ± 0.05
50	1.02 ± 0.07	1.01 ± 0.07
45	1.07 ± 0.04	1.06 ± 0.03

D (10e-9 m^2s^-1)		
Packing (%)	Without Int. Grad.	With Int. Grad.
75	0.46 ± 0.01	0.46 ± 0.01
70	0.54 ± 0.03	0.54 ± 0.03
65	0.57 ± 0.05	0.57 ± 0.05
60	0.64 ± 0.02	0.65 ± 0.02
55	0.65 ± 0.02	0.65 ± 0.02
50	0.71 ± 0.03	0.71 ± 0.03
45	0.77 ± 0.03	0.77 ± 0.03

Table 4.6: Parameters for 10-micron-spheres

GAMMA		
Packing (%)	Without Int. Grad.	With Int. Grad.
75	0.89 ± 0.06	0.82 ± 0.05
70	0.89 ± 0.09	0.85 ± 0.09
65	0.91 ± 0.06	0.86 ± 0.06
60	1.02 ± 0.05	0.97 ± 0.06
55	1.03 ± 0.02	1.00 ± 0.03
50	1.03 ± 0.05	1.00 ± 0.04
45	1.03 ± 0.02	1.00 ± 0.02

D (10e-9 m^2s^-1)		
Packing (%)	Without Int. Grad.	With Int. Grad.
75	0.66 ± 0.09	0.67 ± 0.08
70	0.79 ± 0.18	0.81 ± 0.18
65	1.01 ± 0.11	1.03 ± 0.12
60	1.33 ± 0.11	1.37 ± 0.11
55	1.36 ± 0.07	1.38 ± 0.06
50	1.52 ± 0.18	1.55 ± 0.17
45	1.56 ± 0.10	1.58 ± 0.10

Next, I highlight some relevant points about the results.

1) GAMMA

For 5-micron spheres, gamma displays a flat profile throughout the packing configurations (mostly between 1 and 1.15). There is a small spread (between 1 and 2 percentage points) between values obtained with and without the contribution of internal gradients, thereby showing that the effect of internal gradients was minimal (figure 27).

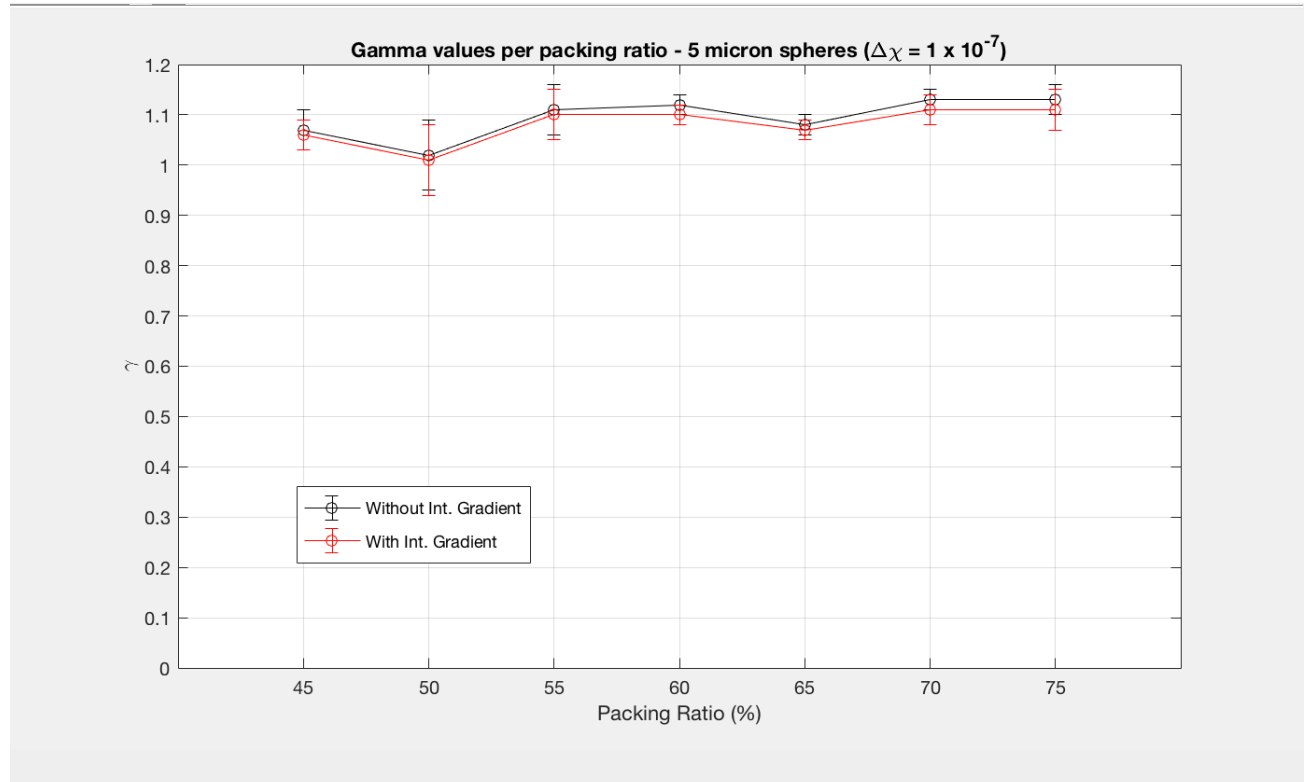


Figure 27: Parameter Gamma for 5-micron spheres

For 10-micron spheres, however, gamma displays a markedly different profile. There seems to be two distinct regions with an inflection point between 60 and 65%. In the first region (packing range 45 - 60%) the values of gamma are very close to unity. In the second region (packings 65 - 75%) values are clearly below 1. The spread between values with and without the internal gradient contribution increases slightly with increasing packing (from 3 to 7 percentage points) (figure 28).

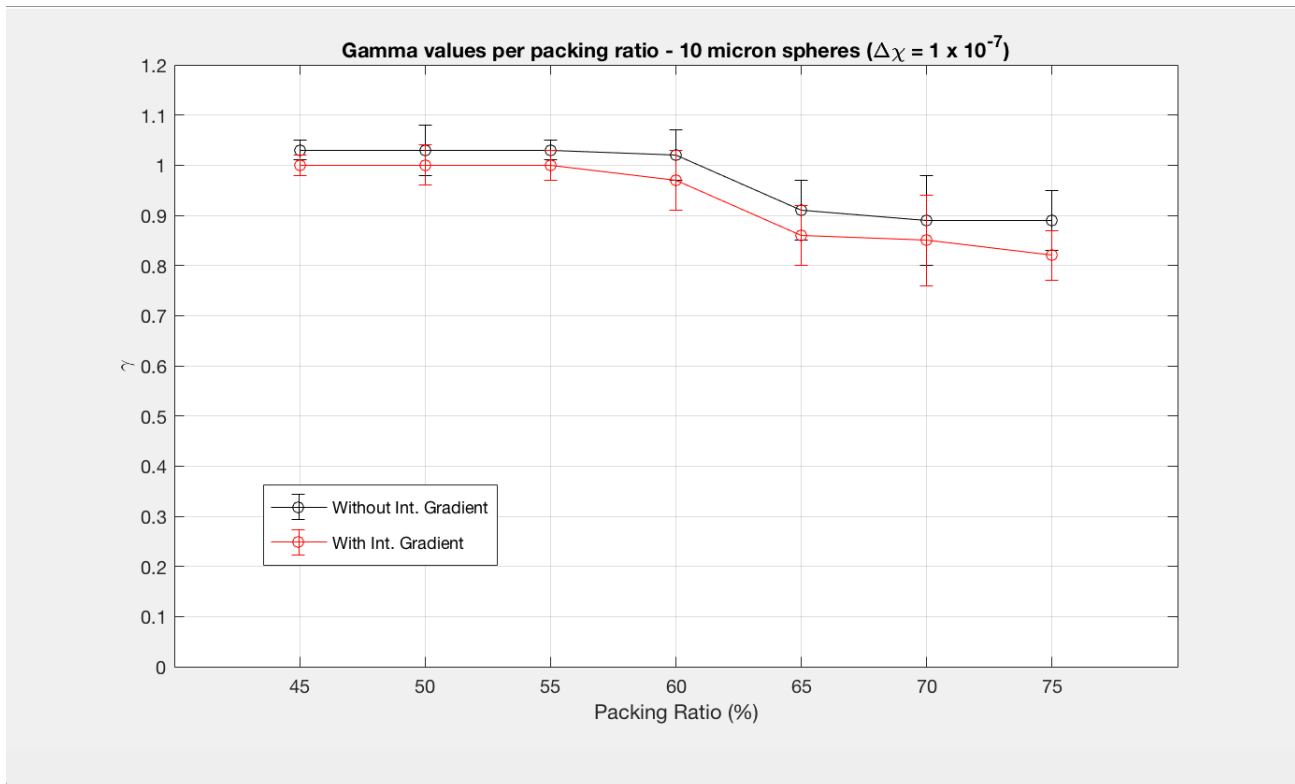


Figure 28: Parameter Gamma for 10-micron spheres

2) D

Two remarks can be made about the parameter D and they are valid for both sphere diameters. First, the parameter barely "feels" the presence of internal gradients. Second, D decreases monotonically with increasing packing and has higher values overall in configurations of 10-micron spheres. Thus, as in the case of Mittag-Leffler's analog parameter (see 4.3.2), D seems to correspond quite well to the underlying lenght scale: it is higher in regions with larger pores and smaller in regions with smaller pores (figures 29 and 30).

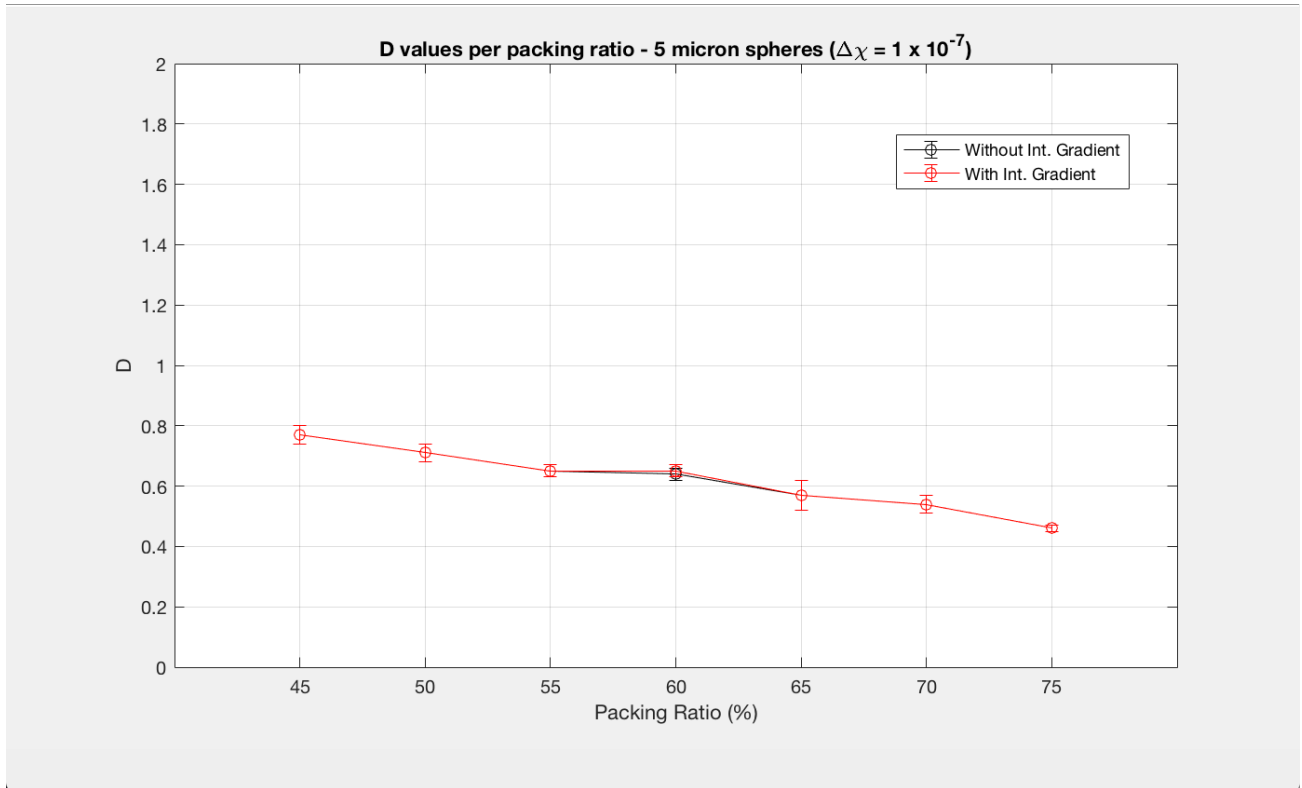


Figure 29: Parameter D for 5-micron spheres

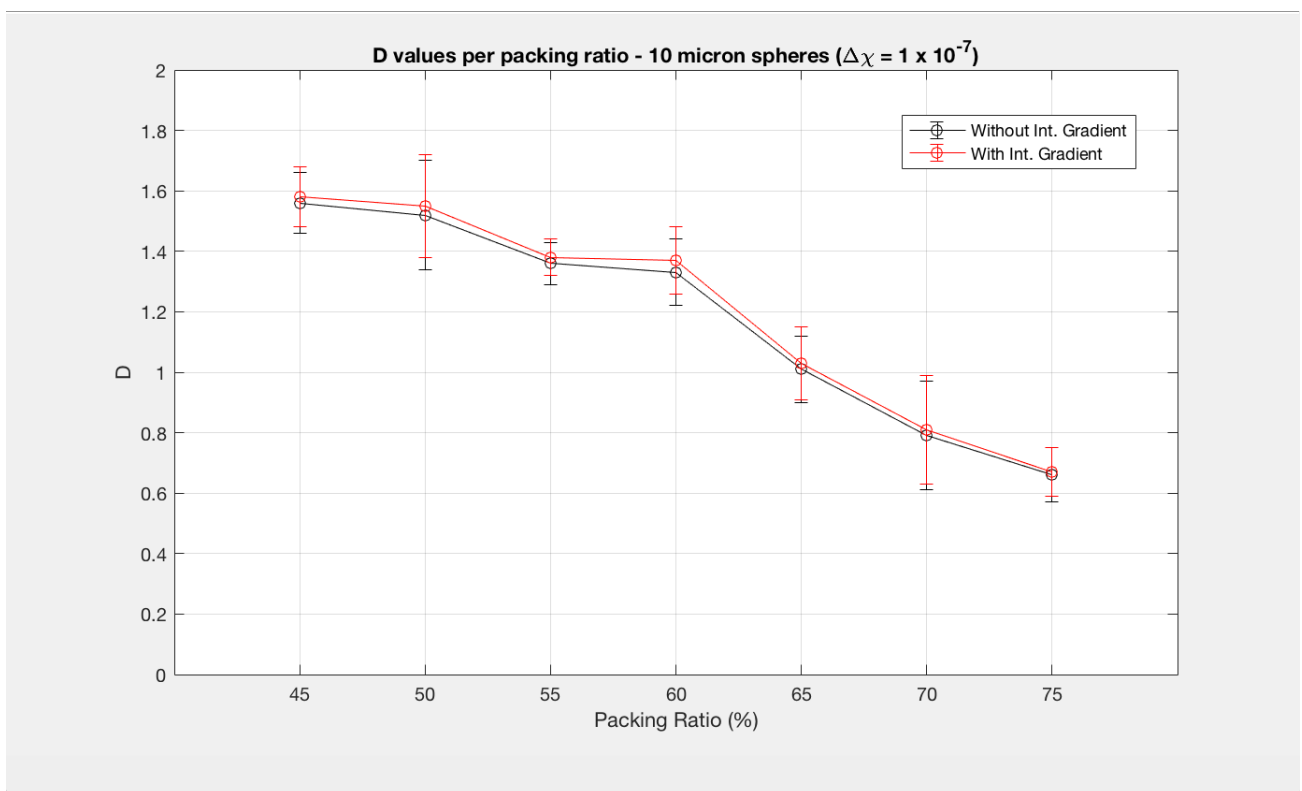


Figure 30: Parameter D for 10-micron spheres

4.3.4 Conclusions and model comparison

The data collected using either model shows that, for the case of 10-micron spheres, the diffusive dynamics changes abruptly somewhere between the packing ratios 60 and 65%. In particular, if we recall the analysis of the Mittag-Leffler results (4.3.2), we observe two regimes: one normal or slightly subdiffusive in the range 45 - 60% and another one markedly subdiffusive in the range 65 - 75%. The Stretched Exponential model data also highlights the fact that there are two regimes, but its interpretation has to be more cautious as I will try to show presently.

The Stretched Exponential model has one parameter less (α). Of the remaining parameters, D is clearly correlated to its Mittag-Leffler analog (D also), as we shall see shortly. γ however neither correlates well with Mittag-Leffler's γ nor assumes the functions of ML's α and γ together. The fact is that under the light of the CTRW's theory the Stretched Exponential is a valid approximation whenever $\alpha \sim 1$, an assumption made in (12) as we saw on subsection 4.2.1. However, particularly in the case of 10-micron spheres, the condition does not hold, as alpha displays values consistently below unity and, what is more, deviates dramatically from anything close to a flat profile. The consequence is that if we were to judge solely on the basis of the Stretched Exponential parameter γ , we would have to conclude that, for the 10-micron spheres and the packings 65 - 75%, the process is superdiffusive, since, in this range, $\gamma < 1$ (figure 28), and thus $\frac{\alpha}{\gamma} = \frac{1}{\gamma} > 1$, a result that would be highly questionable.

At this point one could ask: "How was it possible that what was subdiffusive in one model (Mittag-Leffler) has turned to be superdiffusive in the other (Stretched Exponential)?" The answer to this perplexity lies on the behavior of the parameter D . As I commented above, the D 's are clearly correlated in the two models. As a matter of fact they are practically identical for 5-micron spheres. In the following table the values of D in the two models are compared (figure 31):

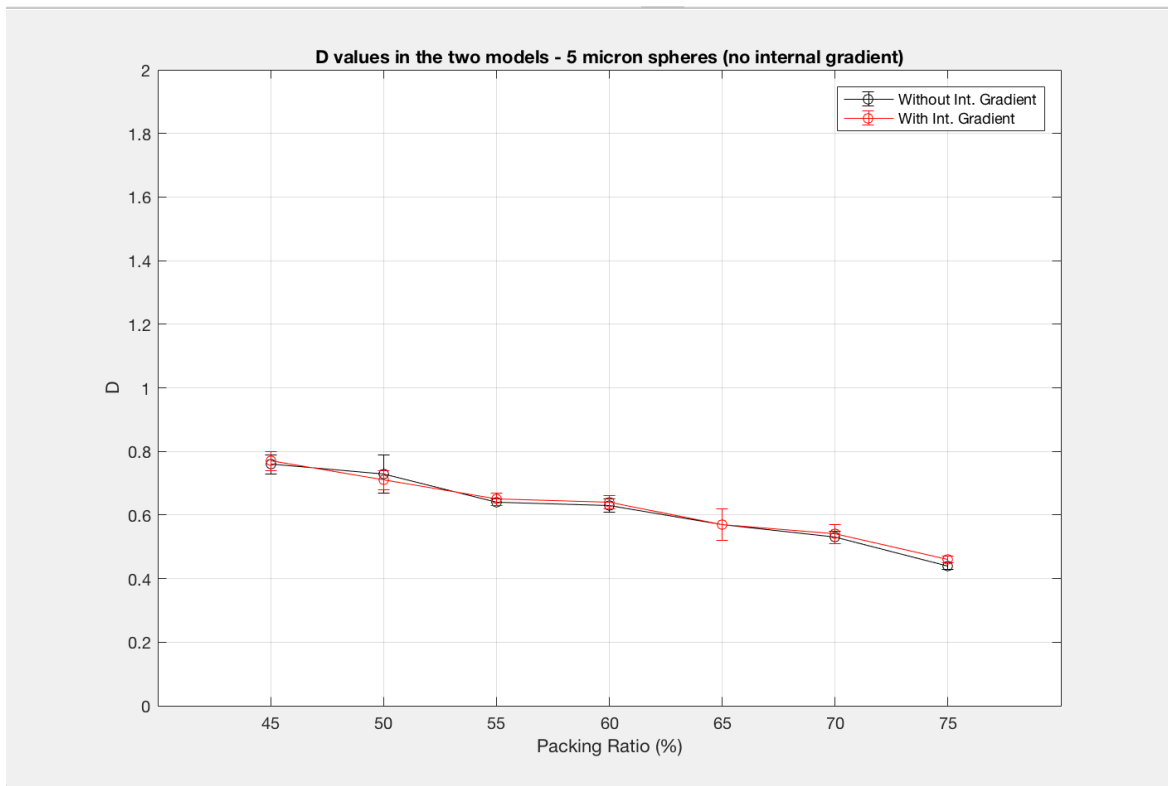


Figure 31: Comparison between D values found in the two models (5-micron spheres).

A similar comparison between the values of the 10-micron spheres shows a striking fact. The coefficient in principle assumes again equal or almost equal values on the lowest packing ratios. On the densest packings, however, the two series differ wildly, the Stretched Exponential values being clearly lower (figure 32).

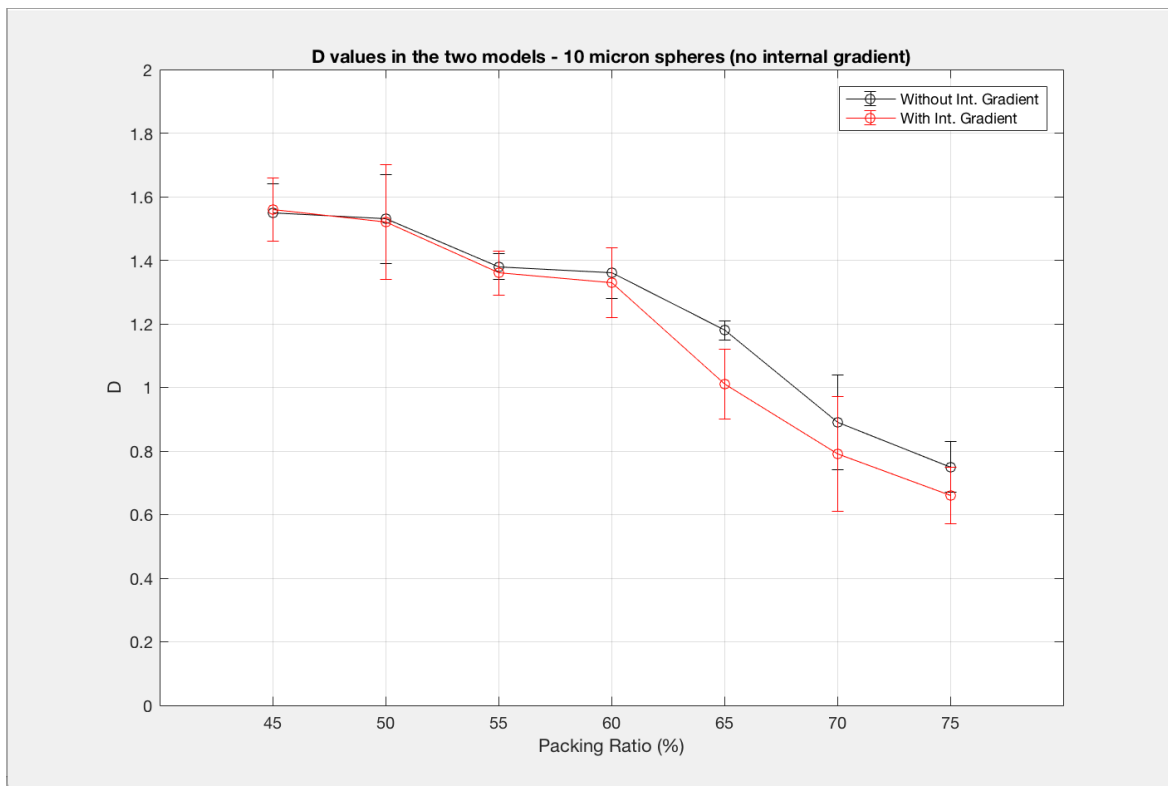


Figure 32: Comparison between D values found in the two models (10-micron spheres).

To sum up, the values of D in the Stretched Exponential model follow closely those of the Mittag-Leffler model whenever diffusion is normal, as is the case of 5-micron spheres (where $\alpha > 1$) or the case of 10-micron spheres in the least dense packings (where $\alpha \sim 1$). When the process becomes conspicuously subdiffusive, with α values clearly departing from unity, the two series of D values differ.

To answer the question posed above, the function of Mittag-Leffler - ML parameter α seems to be "absorbed" in the Stretched Exponential - SE model partly by γ , partly by D. And while the analysis of γ alone (in the SE model) seemed to indicate that the process becomes superdiffusive in the 60 - 75% range, the analysis of D shows that it seems to drop too much (compared to its ML analog) in the same range. One parameter compensates the other and the process is definitely not superdiffusive.

The fact that a model (the Stretched Exponential) behaves badly whenever a necessary assumption (namely, $\alpha \sim 1$) does not hold is a truism. Anyway, we could still take practical advantage from the model, for the commented deviation in the values of D could in principle convey structural information about the medium.

To conclude, we turn our attention once more to the fact that the 10-micron spheres' simulations evidence the existence of two different regimes, with a subdiffusive tendency becoming accelerated somewhere between packings 60 and 65% (first paragraph of this subsection). This phenomenon has been commented at least once in the literature. In (25) it is argued that the parameter regulating anomalous diffusion (here α/γ) can provide "a quantitative characterization of structural disorder and structural transition in heterogeneous systems". In particular, it was observed precisely that, with increasing packing, there is an accelerated tendency towards subdiffusion upon crossing the stress percolation threshold at circa 62%¹⁸. The present simulations no doubt confirm the sensibility of DW-NMR parameters to this structural transition. However, I must point out that the phenomenon was here observed only on configurations of 10-micron spheres, the 5-micron configurations having remained entirely inside the normal diffusion range. This would mean that the ability of the anomalous diffusion parameter α/γ to detect structural transition depends on the scale of the medium. As a corollary, in order to identify and quantify structural disorder in media characterized by different length scales, different diffusing species (slower or faster than water) may be necessary.

¹⁸ The theoretical value according to (25) is circa 64%.

Chapter 5

Application: detecting demyelination in white matter tracts

This thesis aimed at the creation of a program for the simulation of NMR experiments (chapter 3) and its use in the study of systems investigated by University of Rome NMR's researchers in order to deepen the understanding of their results (chapter 4). The present chapter describes a third goal: to use the simulation apparatus to investigate a possible application of magnetic resonance imaging in the diagnosis of demyelinating diseases.

Due to its non-invasiveness and high versatility MRI has had an enormous impact on biomedical research and medical diagnosis. As a matter of fact, MRI has been chosen as the primary laboratorial diagnostic method in some cases. Current research aims in part at trying to identify new potential biomarkers for a number of conditions, e.g., demyelinating diseases. Demyelination is a process by which axons - the elongated extensions of neuron cells responsible for conducting the action potential to other constituents of the nervous system - lose their myelin sheath, i.e., the lipid-constituted outer layer which protects the axon's integrity and guarantees signal transmission's efficiency.

The present chapter concerns simulations that were devised to check whether some DW-MRI parameter can be used as a biomarker of early demyelination. In order to accomplish this, I created three-dimensional models, both of healthy axons and of axons undergoing a demyelinating process. However, there are many types of demyelinating diseases, each with specific characteristics and each attacking different portions of the nervous system. Moreover, there is a fair amount of variation in axonal form and dimension, particularly between the central nervous system - CNS and the peripheral nervous system - PNS, but also between neighboring regions on the same organ. In order to be realistic and to aspire to be of any utility, the present model had to be as specific as possible. For that reason I chose to emulate the characteristics of a real pathology - Multiple Sclerosis, the most common demyelinating disease. Thus the first part of my work concerned reviewing the literature about Multiple Sclerosis in order to identify the best candidates for modeling among the areas affected by the condition.

Having identified that area, a realistic model was created and DW-MRI simulations were run in it, including healthy, lightly demyelinated and heavy demyelinated conditions. The results of these simulations were then fitted by either of the two models treated in this thesis (see Chapter 4) to provide us with the relevant DW-MRI parameters (α , γ and D).

Once the parameters were obtained, k-means clustering analysis were performed in order to investigate whether any of the parameters, either alone or in conjunction, could be potential biomarkers. At least one strong candidate was identified.

5.1 Multiple Sclerosis

Multiple Sclerosis - MS, meaning "many scars" (from latin *sclerae*), is an inflammatory disorder of the central nervous system characterized by multifocal lesions or 'plaques' in both white matter and gray matter. These lesions form in areas undergoing demyelination of axonal tracts and consist mostly of dead nerve cells, myelin debris, macrophages and lymphocytes. The symptoms, consequent on the axonal injury and loss caused by demyelination, may include sensory deficit, overwhelming fatigue, loss of vision in one eye, trouble with coordination and even psychiatric problems.

As far as pathogenesis is concerned, even though it is not yet clear what triggers the condition, there is substantial evidence supporting the hypothesis that MS is an autoimmune disease (26), that is, one in which the immune system attacks the body's own tissues. Supporting this hypothesis is the fact that an inflammatory process caused by T cells is observed. T cells are a kind of lymphocyte - a type of white blood cell from the immune system. After entering the brain due to disruptions in the blood-brain barrier, the T cells interpret myelin as a foreign body and attack it.

Magnetic resonance imaging is the most important paraclinical test for the diagnosis of multiple sclerosis (27). Conventional MRI technique can reveal MS lesions early in the disease course (even before clinical diagnosis). They appear as multifocal spots of increased signal on T2-weighted sequences and are located primarily in periventricular areas. There are also quantified MRI methods that try to assess myelin integrity on microscopic level, although they do not belong to clinical routine practice. Of these methods, the most important is magnetization transfer imaging - MT, which tries to assess myelin content by exploring variations in the measured contrast between tissues associated with protons in bulk water pools and those associated with protons bound to myelin's macromolecules (26). However, there are no established protocols enabling the use of advanced MRI techniques, including MT imaging but also DW imaging and many others, in the diagnosis of MS. The macroscopic identification of plaques through conventional MRI remains the only standardized MRI method, and one that forms the basis of the McDonald criteria, the most commonly used method of diagnosis.

Multiple Sclerosis has no cure. Treatments usually aim at improving function after an attack or reducing the number of relapses. Typical therapies include the administration of intravenous corticosteroids for the relief of symptoms during attacks and the use of beta-interferon, an anti-inflammatory regulatory cytokine which inhibits T-cell proliferation. The latter is known as a type of disease-modifying agent, which is approved for use with the relapsing forms of MS only.

Since it has been established that proper treatment at an early stage aimed at reducing disease activity can delay disease progression and improve longer-term outcomes (28, 26), new methods for the early diagnosis and long-term follow-up of multiple sclerosis are naturally welcome.

5.2 Model for the axons and the demyelination process

As stated in the introduction, if the present simulations were to be of any utility, they had to be as realistic as possible. In order to achieve higher realism, I chose to construct a detailed model of a real pathological condition. Multiple sclerosis was thus chosen due to its importance as the most common demyelinating disease.

5.2.1 Preliminaries

Multiple Sclerosis is a pathology affecting the myelin protection of nerve cells in the brain and in the spinal cord. The natural next step in my work thus concerned the delimitation of a proper region of interest - ROI to be modelled. A good candidate for ROI had to meet three preconditions:

1) **Potential for use in diagnosis.** Thus it had to be a region commonly affected by the disease preferably in its earlier stages;

2) **Availability of metrics.** There should be scientific data available concerning relevant ROI metrics, mainly the axonal diameter distribution and the axonal density.

3) **Potential for NMR detection.** That is, the DW-MRI parameters that we are employing should be sensitive to morphological alterations (i.e. demyelination) occurring in the ROI. In particular, we know that axons' diameters in the CNS are considerably smaller than those in the PNS. Our aim was to find an area in the brain where axons were large enough so to ensure that their alterations could be 'felt' by the DW-MRI parameters.

All three conditions are fulfilled by the corpus callosum. The corpus callosum - CC (latin for 'tough body') is the largest white matter structure in the brain. It is a flat bundle of commissural fibers that connects the two cerebral hemispheres and enables information exchange between them (figure 33).

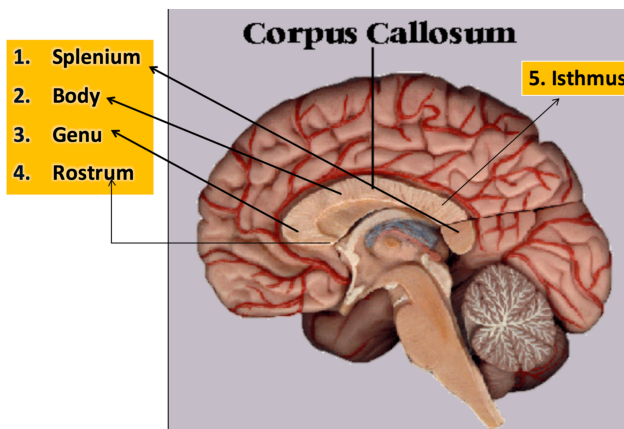


Figure 33: Main subdivisions of the Corpus Callosum (reproduced from (29)).

As far as potential for use in the diagnosis is concerned, identification of corpus callosum lesions is already part of the the brain MRI protocol in medical practice, the sagittal FLAIR sequence being the standard one for the CC (figure 34):

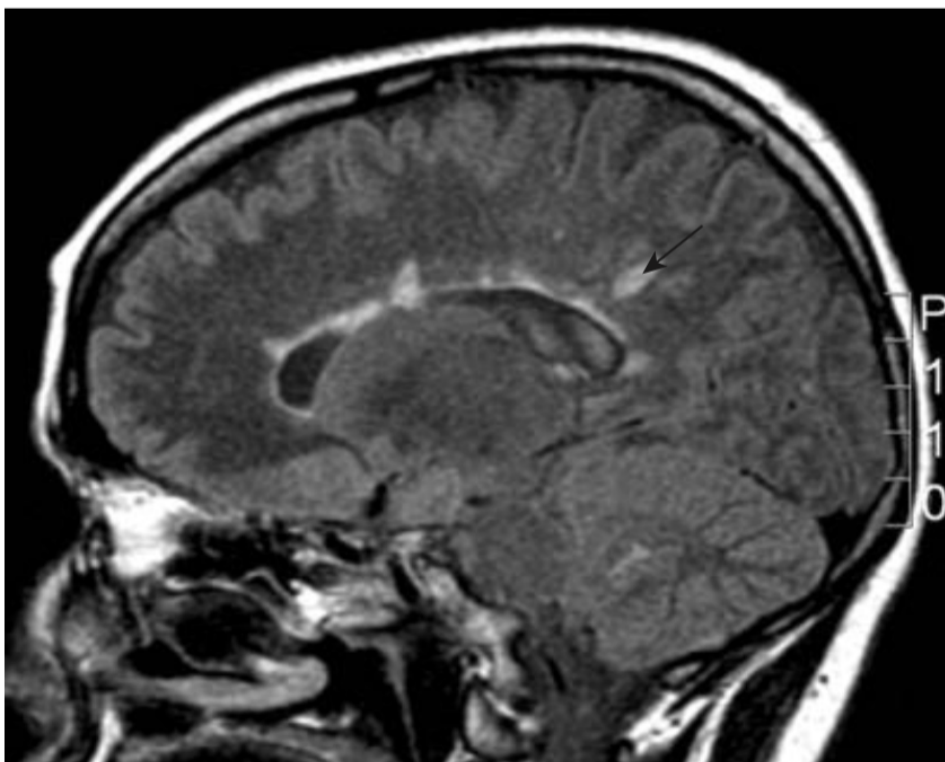


Figure 34: Sagittal FLAIR brain image showing typical multiple sclerosis "T2" lesions. Classic MS lesions include ovoid-shaped, corpus callosum and flame-shaped Dawson Fingers (arrow). (Reproduced from (27)).

Anthony Traboulsee and David Li (reference 27, Chapter 9) mention the findings of a study conducted with patients with a number of white matter diseases. Corpus callosal lesions were seen in 93% of 42 patients with established MS and only in 2% of 127 patients with white matter disease due to other causes. The findings highlight the high sensitivity and specificity of the CC lesions for the diagnosis of MS. The authors are categorical: "The common MRI appearance is multiple white matter lesions with periventricular predominance; it would be unusual if this region was spared in MS." (27)

Concerning the second necessary precondition of our ROI, namely, the availability of metrical data, it is also met by the corpus callosum. Indeed, there is a wealth of information available concerning corpus callosum metrics. The standard reference is (30), which I used to ascertain axonal diameter distribution. The corpus callosum is traditionally divided in eight parts (figure 35):

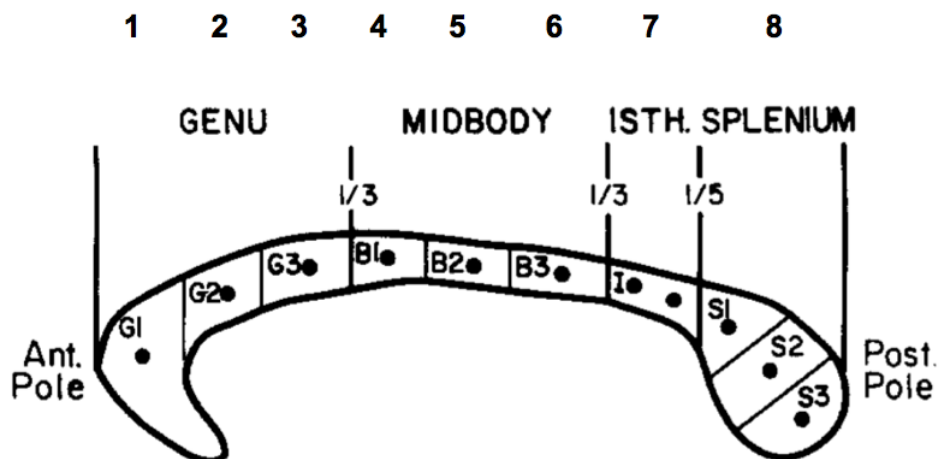


Figure 35: The 8 subdivisions of the corpus callosum (adapted from (30)).

In the paper (30) Dr. Francisco Aboitiz and colleagues provide comprehensive histological data from ex-vivo human brains. The data for the axonal diameter distribution, crucial for my work, was condensed in the following tables, concerning the main subdivisions of the corpus callosum (figure 36):

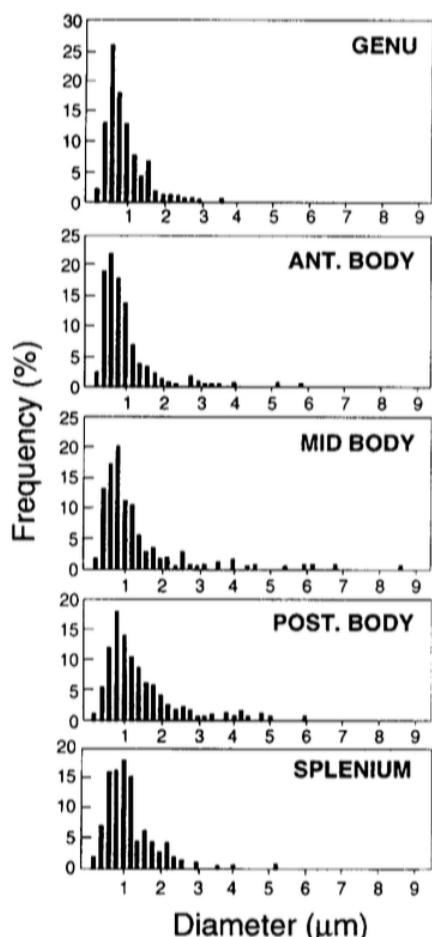


Figure 36: Histogram of axon size frequencies in different regions of the corpus callosum. 'Posterior body' corresponds to regions 6 and 7 from figure 35 (reproduced from (30)).

As for the third precondition - potential for NMR detection - we observe that two of the corpus callosum regions, namely, the posterior body and the mid body, are the subdivisions whose mean axonal diameter is highest (see figure 36).

In particular I chose the subdivision that Dr. Aboitiz and colleagues call 'posterior body' as my ROI. The posterior body corresponds to subdivisions 6 and 7 of the corpus callosum (figure 35), that is, the posterior midbody (B3) and the isthmus.

5.2.2 Modelling axons

Having decided on the best ROI, I began the construction of the computer model. The model consists of a cubic volume containing 256 parallel axons (figure 37).

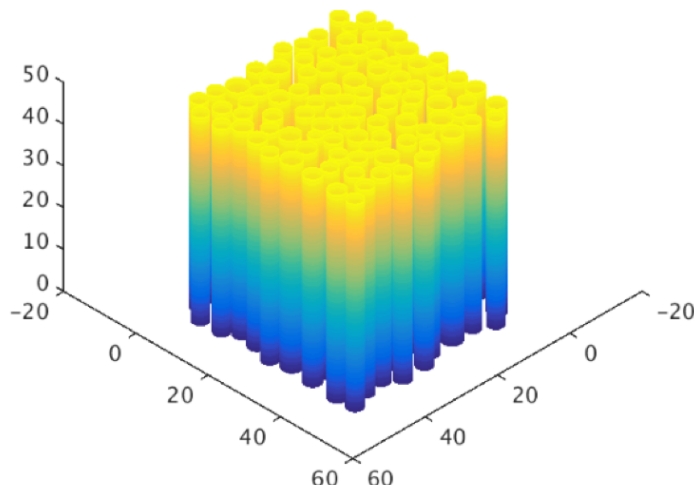


Figure 37: schematic representation of the 3-D random packing of axons (this is a mere illustration, not a true output of the program) (reproduced from (11)).

The axons were modelled as coaxial cylinders, whose internal diameter refers to the axonal diameter and the external diameter refers to total fiber (i.e. axon + myelin sheath) diameter (figure 38). The cylinders' axes lie along the direction Z. As far as the X-Y plane is concerned, the cylinders are randomly disposed.

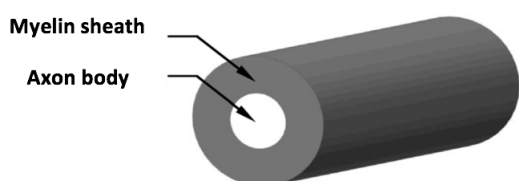


Figure 38: Axonal model (mere illustration, not true output of the program) (adapted from (31)).

In order to construct the simulation space, first I needed to define three metrical characteristics of the sample: the axons' diameters, the axons' concentration and the thickness of their myelin sheath.

a) **Diameters.** As we saw on 5.2.1, the corpus callosum's posterior body was chosen to be the ROI. Since the reference (30) contains ex-vivo measures of the axonal diameter distribution for the ROI (figure 36), I used the article's data to determine for the 256 axons to be modelled the respective quantities of fibers with a given diameter (see table 5.1 below).

b) **Concentration.** Concentration of axonal fibers in the CNS often range between 70 - 80%. I decided to use 80%, the estimate reported in (32).

c) **Myelin sheath dimension.** A parameter called g-ratio quantifies the myelin sheath's relative thickness. It is defined as the ratio between the axon diameter and the total fiber (axon + myelin) diameter. Therefore, an elevated g-ratio, i.e. closer to unity, indicates a thinner myelin sheath. Typical g-ratios range around 0.65. Anyway, I made an effort to determine specific values for the region of interest. There was, however, great variation, with values ranging from 0.60 to 0.74 (33, 34). I decided to use the value 0.74, the choice being the most cautious. Indeed, being in the upper limit, this value guarantees that we are using the thinnest possible myelin configuration in the simulations, that is, one whose alterations are presumed to be harder to detect. If the NMR parameters prove sensitive to such a configuration, we can expect that they will perform even better in configurations with lower g-ratios, i.e., thicker myelin sheaths.

Having determined these three metrical properties, I arrived at the final composition of the axonal bundles. The following table lists the values I used for the simulations. On column 1 are listed the fiber diameters and on column 2 the individual counts out of the 256-element sample. I recall that this distribution is based on the exact distribution reported in (30). I remark that the diameters listed refer to total fiber diameters, i.e., including the myelin sheath (table 5.1).

In order to create the spaces, I implemented a subroutine of the Geometry block (see Chapter 3) called "Axons". The subroutine takes as input the degree of myelination in the sample (the value 1 corresponding to healthy axons). In each run the subroutine creates a simulation space with 256 axons randomly disposed and in the degree of myelination intended (more on this on the next subsection).

Table 5.1: Number of axons per given diameter

Fiber Diameter (μm)	Count
0.27	3
0.54	13
0.81	29
1.08	44
1.35	35
1.62	26
1.89	21
2.16	15
2.43	14
2.70	10
2.97	6
3.24	5
3.51	6
3.78	4
4.05	2
4.32	2
4.59	3
5.14	3
5.41	2
5.68	4
5.95	2
6.49	3
6.76	2
8.11	2
Total	256

In the following, as was the case with the simulated spheres, the simulation space was digitalized, i.e., numerical values were attributed to each of the $256 \times 256 \times 256$ cells in which the simulation space was partitioned. The value '0' was attributed to cells whose center lay outside the fibers. The cells classified as '0' were the only ones available for the random walk trajectories. Thus, we already touch upon a very important trait of the simulations: they concern **diffusion only in the extra-axonal space**. No trajectory was

allowed inside the fiber's body (either the axonal or the myelin part) and thus no signal was computed for intra-axonal regions. Resuming the explanation about digitalization, the remaining regions - the axon body and the myelin - were attributed the values '2' and '1' respectively. Both regions, as we explained, are forbidden regions for random walk trajectories. The reason for attributing different values to them is to enable the program to quantify total myelination in the sample. This feature, as we will see shortly, will be useful when creating samples with demyelination in different degrees.

Later we will run NMR simulated experiments on the samples. In total 60 samples, among healthy and demyelinated, were generated for the simulations, each one consisting of a new, randomic disposition. Below we can see two different samples created by the program. Remark that these are true program outputs (the images are transverse sections, figure 39):

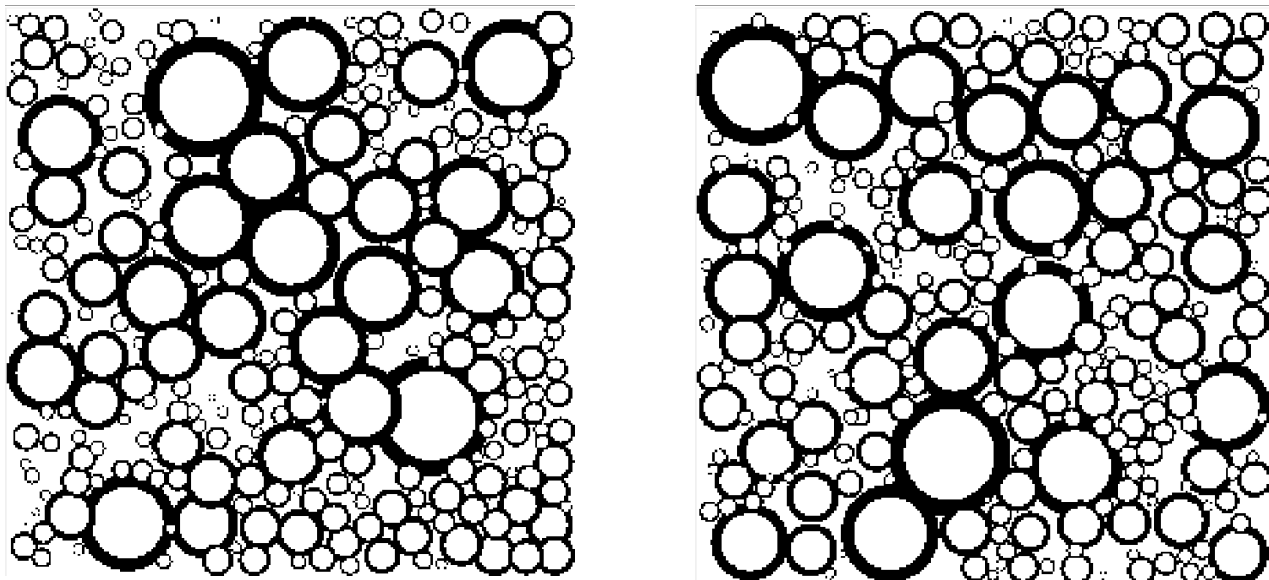


Figure 39: two true program outputs. Each depicts a sample space with 256 randomly packed axons whose diameters were drawn from the empirical distribution of table 5.1. The myelin sheaths are the black circles separating intra- and extra-axonal spaces.

5.2.3 Modelling demyelination

The program outputs showed on the previous subsection correspond to samples of healthy axons, i.e., those in which the myelin sheath is intact. Each of the 256 axons created for one simulation space display a complete myelin sheath, in the same g-ratio (0.74) albeit the fibers naturally differ in diameter. As an example, below we see a longitudinal section of one of the axons created for a healthy sample. The myelin sheath is the black 'coat'. We cannot visualize any distinction in this image between the axon body (inside the myelin) and the extra-axonal space for both are in white color. However, as stated in the precedent

subsection, the two regions are recognized by the program and treated accordingly. Remark that the image corresponds to a true program output (figure 40):

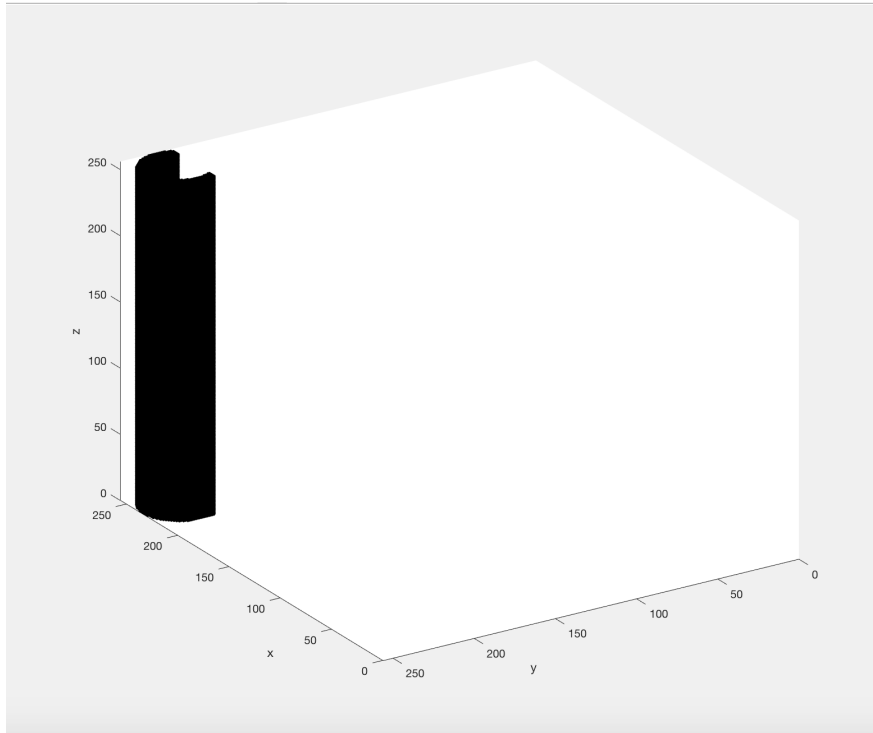


Figure 40: Healthy axon in longitudinal section for better visualization (not an illustration, true output).

In order to run NMR simulations and compare the results from healthy and non-healthy axons, it was necessary to create also demyelinated samples. So I implemented a script (called "Demyelinate") to 'demyelinate' the axons created in the previous step. This script was incorporated into the subroutine "Axons" and was called whenever the input parameter "degree of myelination" was less than one. For instance, suppose the entered parameter has been 0.7. This means we are requiring the subroutine to create a simulation space whose axons display a level of myelination of 70%, or else, they have lost 30% of their myelin sheath. The subroutine first creates a healthy simulation space. Then, it calls the script "Demyelinate" so that it removes 30% of the myelin content of the entire simulation space. The script "removes" myelin content by changing the value of simulation space cells. Thus, a cell located in a myelin region receives originally the value '1' (see previous subsection). If it is to be removed, its value is changed to '0'. In this manner, it becomes part of the extra-axonal space and so it is considered to be an accessible space for the creation of trajectories by the Random Walk block.

The script "Demyelinate" tries to emulate the real inflammatory process which is presumably the cause of demyelination in multiple sclerosis. The model has the following characteristics:

1) all fibers in the sample are attacked but to different degrees, the degree of demyelination (in our example, 30%) referring to the sum of all myelinated cells in a simulation space;

2) the choice of points to be attacked is random but subject to preferred directions as discriminated on 3 and 4 below.

Since the script simulates an attack of the immunological system on the myelin sheath, two further characteristics of the simulated attack are:

3) it is mainly external, that is, it generally proceeds from the outer part of the myelin inwards; and

4) it is focal. It means that there are main spots from which damage is spread. As a matter of fact, it would not be realistic if the points of attack were evenly dispersed along the fibers.

In the following I display examples of the program's output. In each one we see a specimen isolated from a 256-axon sample. The images are three-dimensional but black-and-white. Thus, in order to improve visualization, I opted to include only part of the axons, i.e., a longitudinal section. Again, I remark that these are not mere illustrations, but true outputs of the program, as used in the simulations. Note how demyelination, albeit random in principle, has focal, or main points of attack (figures 41-45).

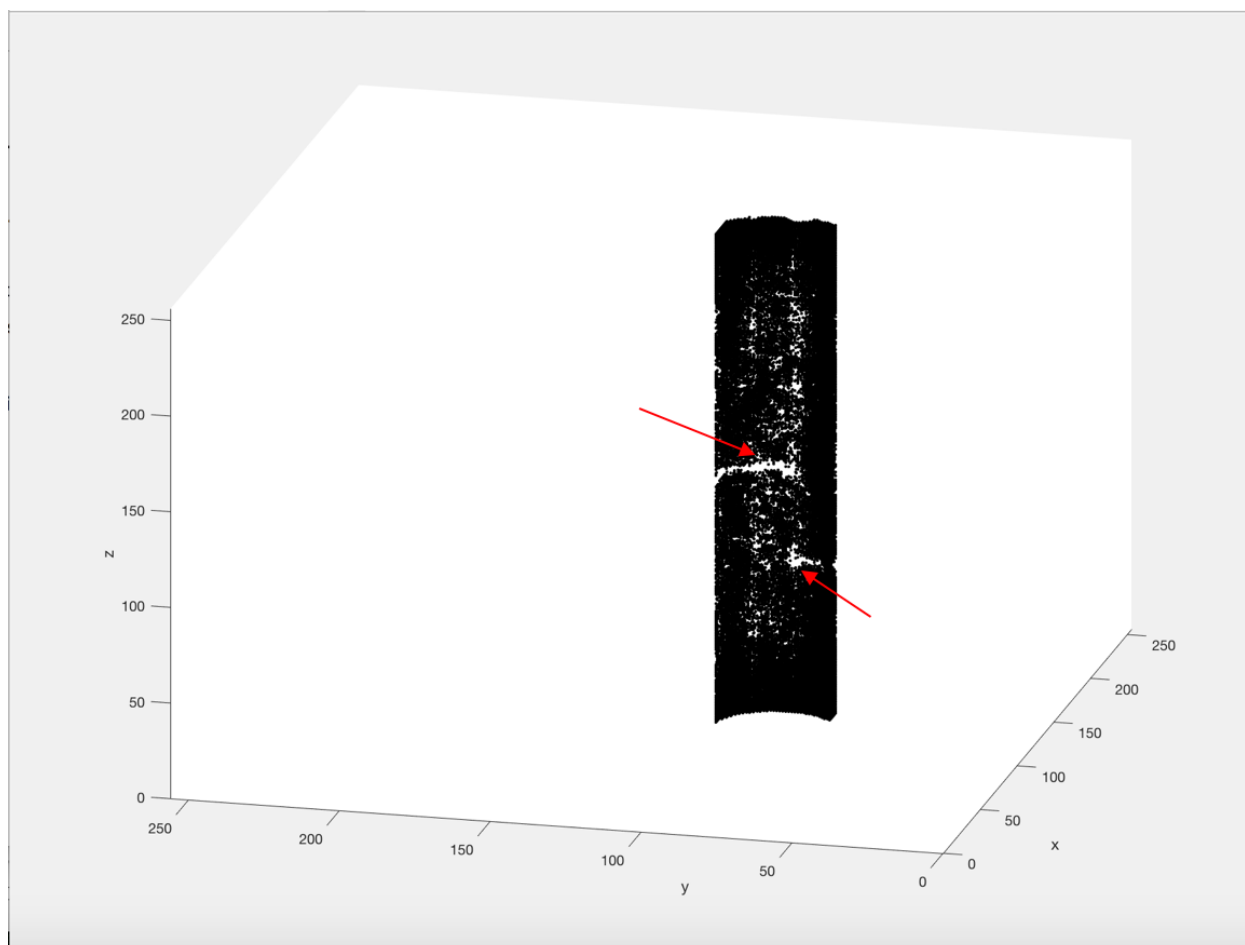


Figure 41: Longitudinal section of demyelinated axon. Arrows show 'inflammation' focal spots.

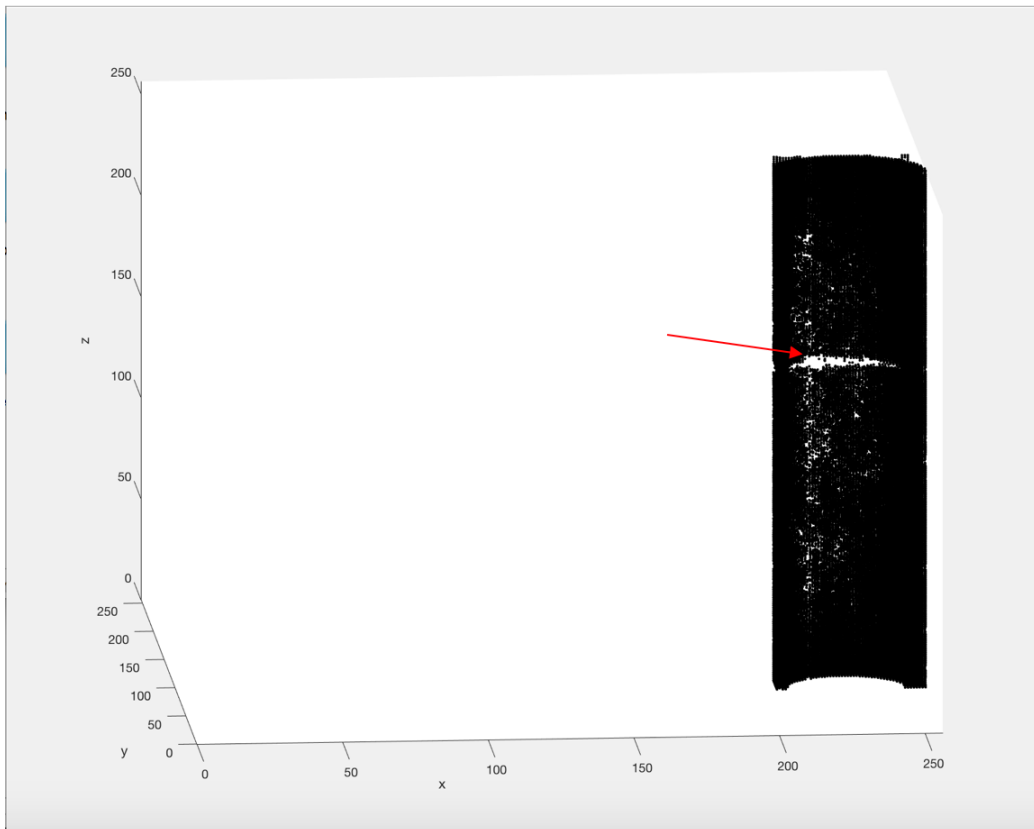


Figure 42: Longitudinal section of demyelinated axon. Arrow shows main 'inflammation' spot.

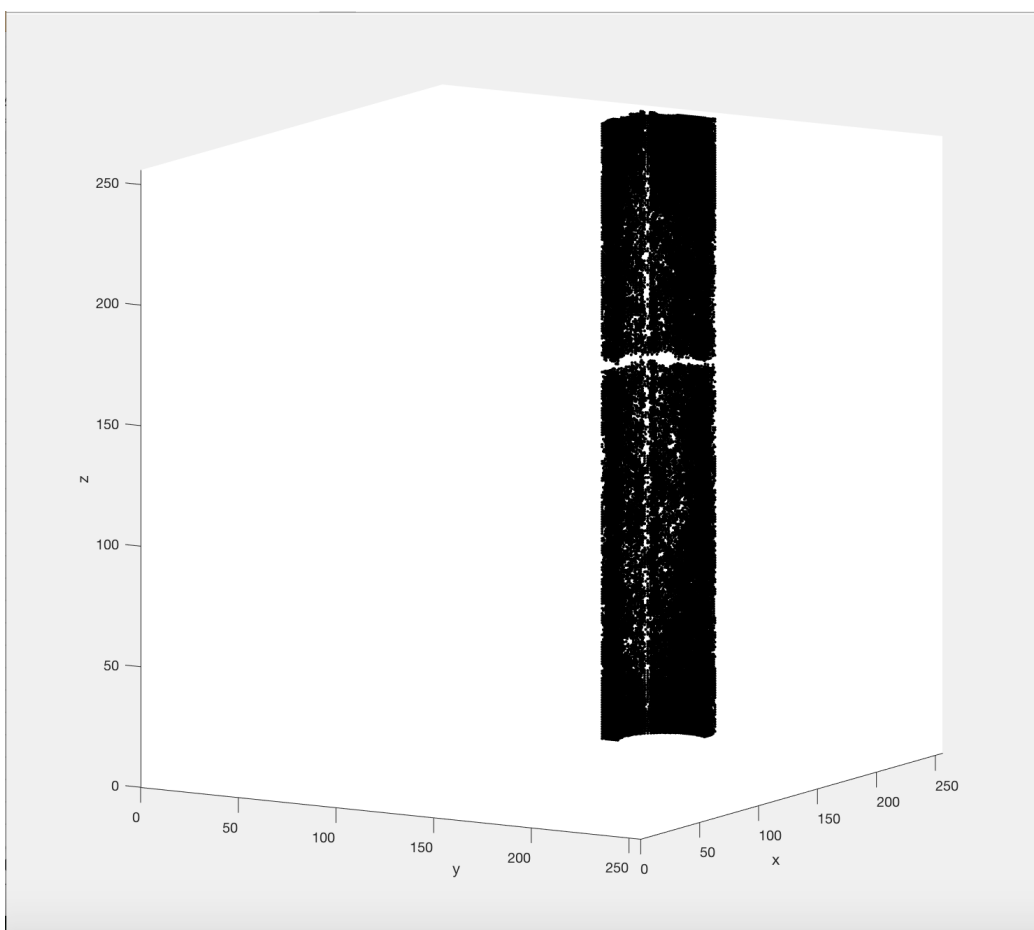


Figure 43: Longitudinal section of demyelinated axon.

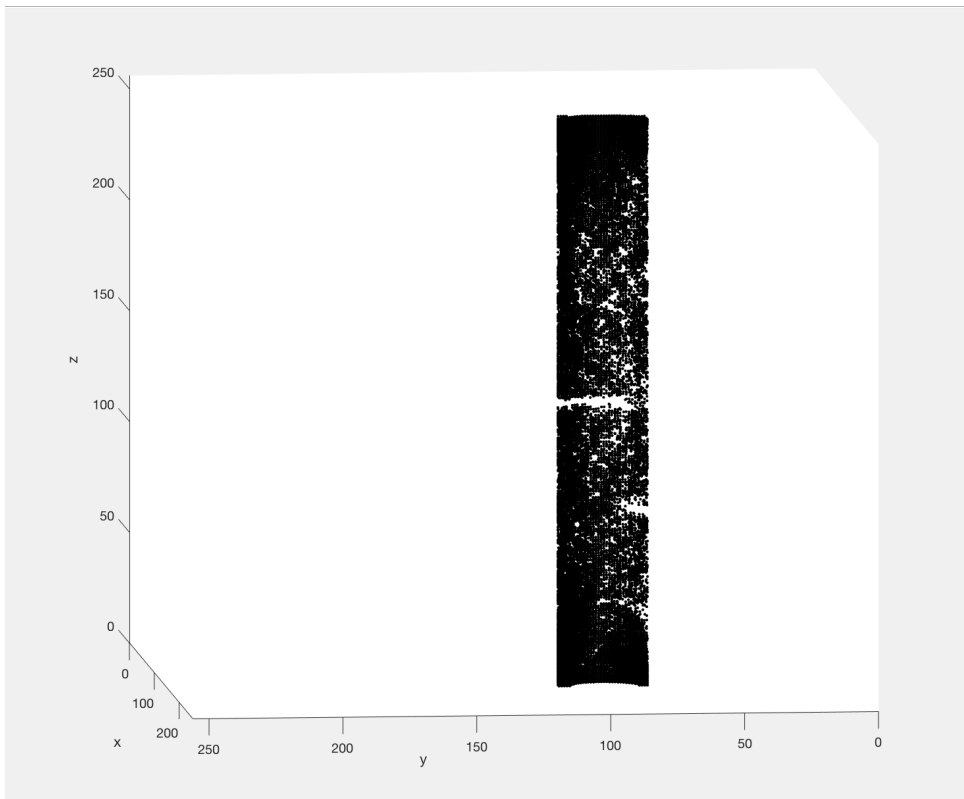


Figure 44: Longitudinal section of demyelinated axon.

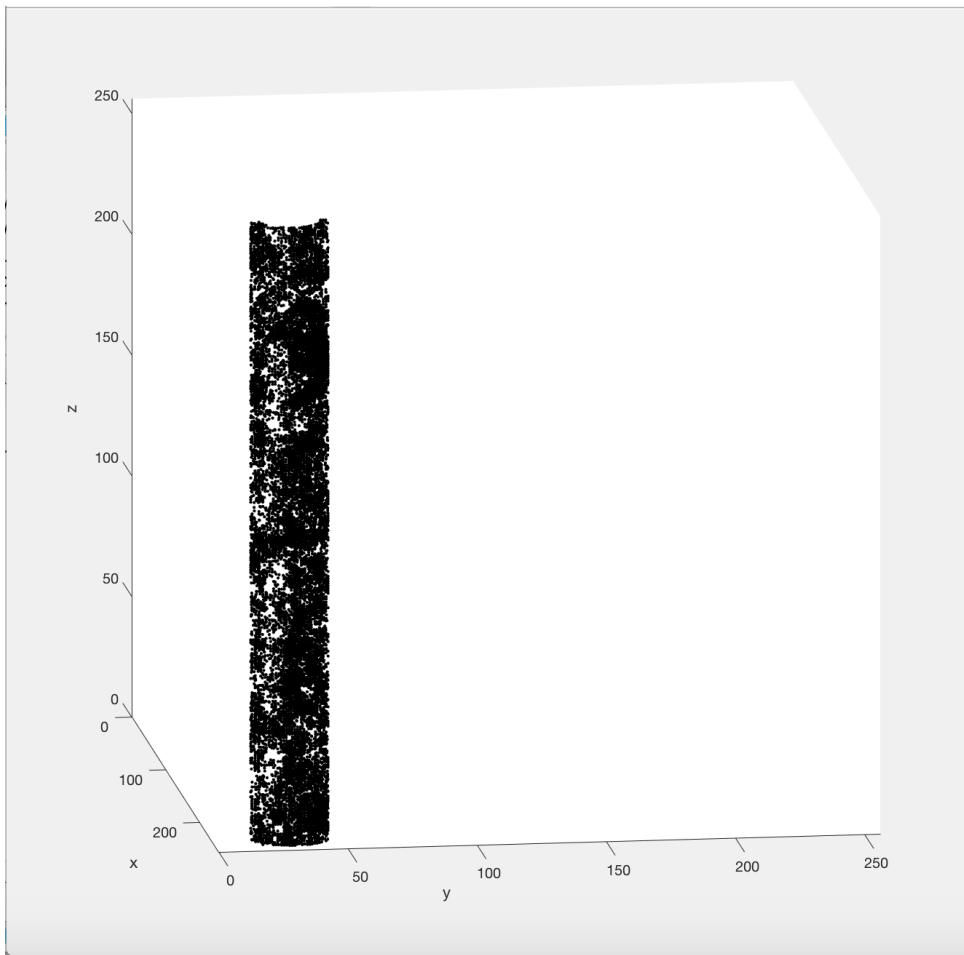


Figure 45: Longitudinal section of heavily demyelinated axon (like the figures above, this is not an illustration, but a true program output).

5.3 NMR simulations and results

5.3.1 Simulation setup

Using the routines described on the previous section, a total of 60 simulation spaces, each containing 256 randomly packed axons, were created: 20 healthy, 20 30% demyelinated and 20 60% demyelinated (that is, with total myelin loss of 0, 30 and 60%, respectively). In the following, the Random Walk block (Chapter 3) created trajectories and the Signal Calculation block calculated signal decay.

As far as the creation of trajectories is concerned, there is not much to be added to the explanations given on 3.1.2. The main point to be stressed here is that trajectories were allowed only on extra-axonal spaces. Regions affected by demyelination became *ipso facto* part of the extra-axonal space. The axons' bodies, however, **even when fully devoid of their myelin coating**, continued to be areas forbidden to random walk trajectories. This corresponds to the hypothesis of perfect impermeability of the axonal membrane, a hypothesis which, while being an obvious approximation for the sake of our simulations, is not far removed from the biophysics of neuron cells. In this regard I mention the high values of anisotropy found in demyelinated axons and reported in (35)¹⁹.

The NMR simulations, by its turn, had the following characteristics:

- a) One NMR simulated experiment was performed on each of the 60 simulation spaces. In each one, signal decay was computed for 1.000 trajectories.
- b) A PGSE sequence with NMR parameters $\Delta/\delta = 80/4.4$ ms, $B_0 = 9.4$ T and gradient applied on direction Y.
- c) 15 b-values were used (100, 500, 1.000, 1.500, 2.000, 3.000, 4.000, 5.000, 6.000, 7.000, 8.000, 9.000, 10.000, 11.000 and 12.000 s/mm²) and again the gradient is the only quantity in the b-value to be varied (diffusion time is kept constant).
- d) For the sake of reducing total simulation time, no internal gradient computation was performed. In any case, the extreme smallness of the axonal simulation spaces, the results of the simulations with the smaller spheres (5-micron, see Chapter 4), the fact that susceptibility difference between water and myelin is probably less than 0.1 ppm²⁰ and the results of some tests I ran all suggest that the simulations with axons would present no or

¹⁹ "Anisotropic water diffusion in neural fibers must not be regarded as myelin specific. Axonal membranes play a major role since, as we will see below, the other potential contributors (neurofibrils, fast axonal transport, susceptibility) to anisotropy are not significant." (see 35, p. 442)

²⁰ Relevant values found in the literature are 0(-0.1) ppm (36), -0.089 and -0.068 ppm (37) and -0.08 ± 0.01 ppm (38).

almost no difference between experiments with and without internal gradients.

e) The Mittag-Leffler parameters D , α and γ were obtained after the fitting routine described on 4.1.1 and the Stretched Exponential parameters D and γ were obtained after the fitting routine described on 4.1.2.

5.3.2 Results

In the following I present the two series of results - one for the Mittag-Leffler fit and the other for the Stretched Exponential fit.

a) Table 5.2: Mittag-Leffler results

Simulation number	Alpha	D	Gamma	Type
1	1.08	0.04	0.88	Healthy
2	0.51	0.12	1.05	Healthy
3	1.42	0.03	0.91	Healthy
4	0.03	0.04	0.69	Healthy
5	0.03	0.00	0.97	Healthy
6	1.06	0.13	0.86	Healthy
7	0.30	0.06	1.00	Healthy
8	0.09	0.03	0.82	Healthy
9	0.36	0.10	1.01	Healthy
10	1.08	0.07	0.95	Healthy
11	0.15	0.04	1.02	Healthy
12	0.48	0.06	1.03	Healthy
13	0.15	0.04	0.92	Healthy
14	1.48	0.07	0.80	Healthy
15	0.20	0.07	0.88	Healthy
16	0.03	0.04	0.83	Healthy
17	0.06	0.02	1.07	Healthy
18	0.01	0.13	0.91	Healthy
19	0.07	0.02	0.98	Healthy
20	0.79	0.08	1.05	Healthy
21	0.96	0.40	1.04	30%

Simulation number	Alpha	D	Gamma	Type
22	0.14	0.31	1.04	30%
23	1.01	0.20	0.88	30%
24	0.88	0.24	1.02	30%
25	0.76	0.28	0.97	30%
26	0.86	0.31	0.98	30%
27	0.84	0.17	0.87	30%
28	0.09	0.32	1.02	30%
29	0.79	0.27	1.03	30%
30	0.63	0.23	1.10	30%
31	1.01	0.25	0.93	30%
32	0.42	0.22	1.10	30%
33	0.33	0.27	1.05	30%
34	0.31	0.24	1.11	30%
35	0.83	0.33	1.08	30%
36	0.84	0.21	0.95	30%
37	0.73	0.30	1.09	30%
38	0.67	0.25	0.99	30%
39	0.86	0.26	1.01	30%
40	0.93	0.12	0.85	30%
41	0.87	0.51	1.13	60%
42	1.08	0.47	0.98	60%
43	0.96	0.48	1.12	60%
44	1.05	0.49	1.09	60%
45	1.00	0.50	1.09	60%
46	0.90	0.55	1.14	60%
47	1.13	0.45	1.01	60%
48	1.05	0.52	1.07	60%
49	1.00	0.58	1.05	60%
50	1.00	0.53	1.04	60%
51	1.04	0.61	1.15	60%
52	0.86	0.56	1.15	60%
53	0.92	0.59	1.16	60%
54	0.93	0.54	1.13	60%
55	1.13	0.52	1.01	60%

Simulation number	Alpha	D	Gamma	Type
56	1.04	0.55	1.12	60%
57	0.86	0.54	1.08	60%
58	0.67	0.52	1.19	60%
59	0.98	0.47	1.00	60%
60	0.90	0.55	1.10	60%

b) Table 5.3: Stretched-Exponential results

Simulation number	D	Gamma	Type
1	0.04	0.89	Healthy
2	0.10	0.88	Healthy
3	0.03	0.95	Healthy
4	0.03	0.60	Healthy
5	0.00	0.96	Healthy
6	0.13	0.88	Healthy
7	0.05	0.88	Healthy
8	0.03	0.73	Healthy
9	0.08	0.85	Healthy
10	0.07	0.97	Healthy
11	0.03	0.92	Healthy
12	0.06	0.92	Healthy
13	0.03	0.83	Healthy
14	0.06	0.87	Healthy
15	0.05	0.76	Healthy
16	0.03	0.73	Healthy
17	0.02	1.01	Healthy
18	0.07	0.72	Healthy
19	0.01	0.93	Healthy
20	0.07	0.99	Healthy
21	0.39	0.98	30%
22	0.19	0.72	30%
23	0.20	0.89	30%

Simulation number	D	Gamma	Type
24	0.23	0.94	30%
25	0.24	0.81	30%
26	0.28	0.86	30%
27	0.16	0.80	30%
28	0.19	0.71	30%
29	0.24	0.88	30%
30	0.19	0.88	30%
31	0.25	0.93	30%
32	0.16	0.83	30%
33	0.18	0.76	30%
34	0.17	0.80	30%
35	0.30	0.93	30%
36	0.19	0.85	30%
37	0.26	0.88	30%
38	0.21	0.80	30%
39	0.24	0.90	30%
40	0.12	0.82	30%
41	0.48	0.97	60%
42	0.48	1.06	60%
43	0.48	1.07	60%
44	0.50	1.11	60%
45	0.51	1.09	60%
46	0.53	1.04	60%
47	0.47	1.09	60%
48	0.52	1.09	60%
49	0.57	1.02	60%
50	0.52	1.02	60%
51	0.61	1.15	60%
52	0.52	0.99	60%
53	0.57	1.06	60%
54	0.52	1.03	60%
55	0.54	1.12	60%
56	0.55	1.12	60%
57	0.50	0.92	60%

Simulation number	D	Gamma	Type
58	0.43	0.86	60%
59	0.46	0.97	60%
60	0.52	0.98	60%

5.4 k-means clustering analysis

Having obtained NMR data for all 60 sample spaces, I performed a k-means clustering analysis on the relevant parameters (D and γ). K-means clustering is a type of unsupervised machine learning algorithm, which is used for unlabeled data. The algorithm tries to identify natural groups, or clusters, in the data. The total number of observations is partitioned into k mutually exclusive clusters and each observation is assigned to the cluster with the nearest mean (or median). The algorithm's outputs are the labels for the observations and the centroids of the k clusters. The analysis undertaken here took inspiration from a similar analysis found in (24).

The analysis is divided in two main sections. On the first one, the groups of healthy and 60% demyelinated axons were compared. On the second one, the groups of healthy and 30% demyelinated axons. In both cases, k-means clustering analyses were performed for the parameters D and γ independently and for the two-dimensional clustering (D, γ) ²¹ (both for the Mittag-Leffler model parameters and for the Stretched Exponential model parameters). The parameter alpha was excluded from the analyses for visual inspection of the plotted data showed no clustering pattern. In every case the parameter k was set to 2 so that the algorithm should identify two clusters. Next, we would compare the program's output labels to the true classification of our observations in order to evaluate the discriminating ability of each parameter or combination of parameters, i.e., (D) , (γ) and (D, γ) .

Three indicators were computed for the evaluation: sensitivity, specificity and accuracy. These are traditional measures of diagnostic accuracy. Sensitivity refers to the ability of the biomarker to identify subjects with the disease. It is defined as the proportion of subjects diagnosed with the disease in a total group of subjects with the disease. Specificity, a complementary test to sensitivity, refers to the ability of the biomarker to identify subjects without the disease. It is defined as the proportion of subjects with negative test in a total group of subjects without the disease. Finally, accuracy, or diagnostic effectiveness, is defined as the proportion of correctly classified subjects (that is, either health subjects who have received a negative result or subjects with the disease who have received a positive result) among all subjects tested (39).

5.4.1 Groups of healthy and 60%-demyelinated axons: results

The parameters obtained with the Stretched Exponential model were the first to be analyzed. A first, exploratory analysis suffices to indicate that the parameter D potentially

²¹ I used MATLAB's built-in function kmeans for the analyses.

has a good discriminating capacity. In fact, on figure 46 below the 60 observations are plotted on a $D \times \gamma$ axis and discriminated by the color: the blue points correspond to the parameters obtained in healthy samples, the yellow ones to the 30%-demyelinated samples and the red ones to the 60%-demyelinated samples. As can be seen, the three types of samples seem to correspond neatly to three regions of D : low D 's corresponding to healthy samples, medium D 's to 30% samples and high D 's to 60% samples. As for the parameter Gamma, there also seems to be a correlation, even if to a lesser degree, with higher values of Gamma corresponding to a higher degree of demyelination.

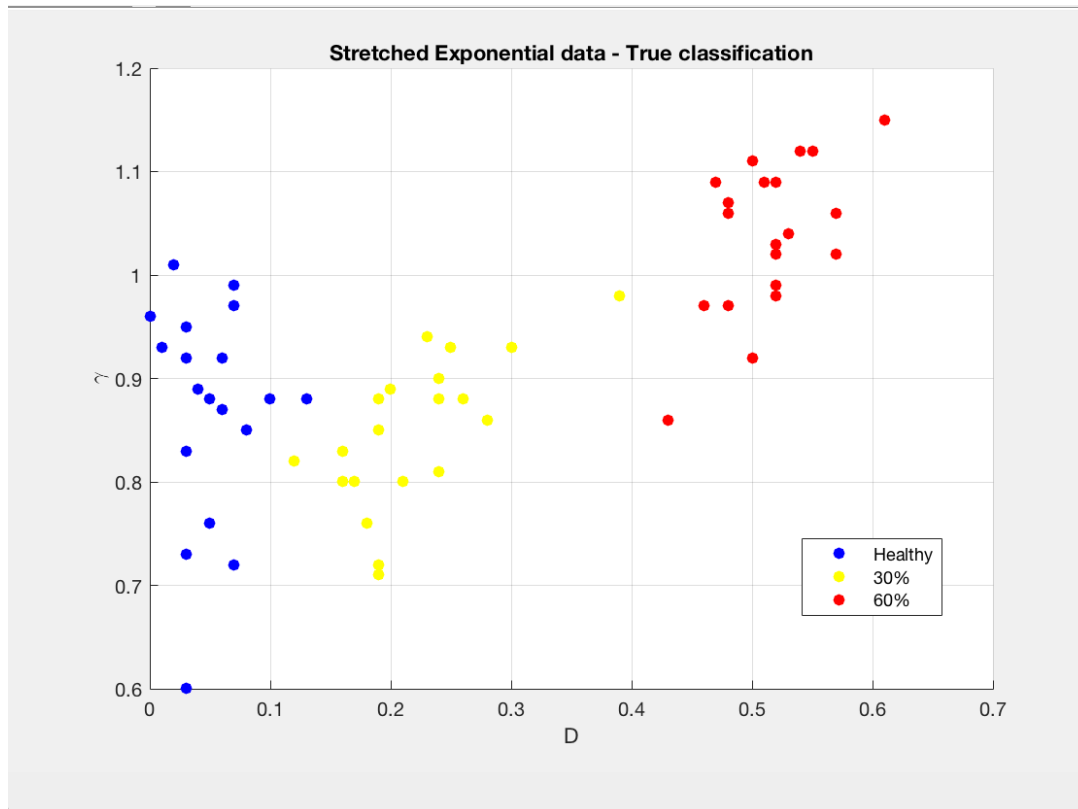


Figure 46: Plot of Stretched Exponential parameters. Coloring indicates true classification.

I observe that the above plot was conceived only for the purpose of an exploratory analysis. The detailed analysis, as explained on this section's introduction, involves the discrimination between only two groups at a time, that is, either healthy - 30% or healthy - 60%.

A similar exploratory analysis was done for the parameters of the Mittag-Leffler model. In this case this preliminary step suggested that no further analysis needed to be carried out concerning the parameter α . In fact, as can be seen on figure 47 below, there seems to be almost no correspondence between α and the degree of myelination.

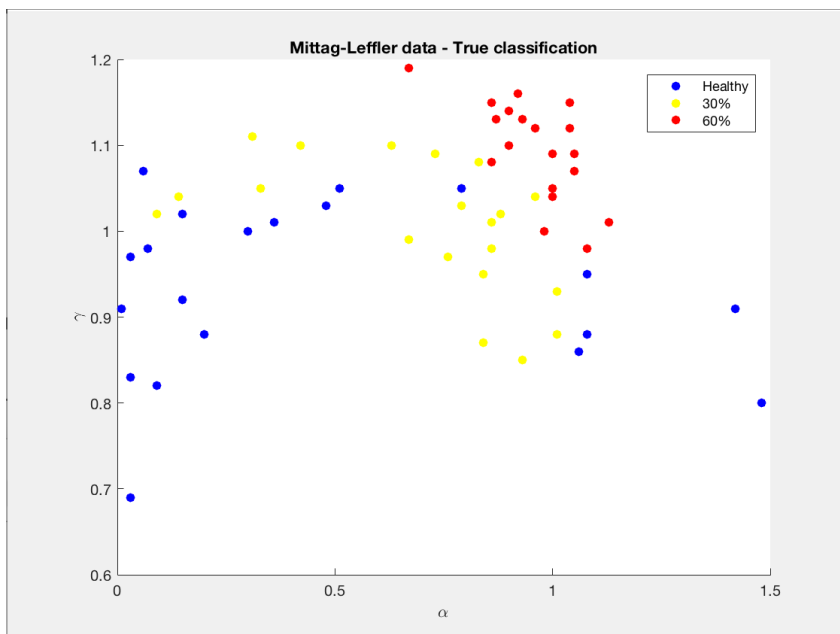


Figure 47: Plot of Mittag-Leffler parameters. Coloring indicates true classification

In the following, for the k-means cluster analysis properly, only the parameters from the groups healthy and 60% were selected to be examined. As reported on the introduction, analyses were carried out for the parameters D , γ and for the combination (D, γ) (both from the Mittag-Leffler model - ML and the Stretched Exponential model - STR). For each of the three kinds of predictors the two clusters identified by the algorithm were compared to the real classification and the indicators of diagnostic accuracy were computed. In the following table I list the results. My comments follow.

Table 5.4: Results of the analysis Healthy x 60% demyelinated

Biomarker	Model	Sensitivity	Specificity	Accuracy
D	ML	1.00	1.00	1.00
	STR	1.00	1.00	1.00
GAMMA	ML	1.00	0.55	0.78
	STR	0.90	0.75	0.83
D + GAMMA	ML	1.00	1.00	1.00
	STR	1.00	1.00	1.00

As we can see, both D and the combination (D, γ) , obtained by either model, attained perfect accuracy as measured by the three indicators. As for the Gamma used in isolation, the Stretched Exponential parameter scored better than the Mittag-Leffler one, at least on two indicators: specificity and accuracy.

In order to corroborate this analysis, I calculated for each parameter and each of the two groups (healthy and non-healthy) the respective mean and sample standard derivation. The difference between the healthy and non-healthy groups, especially regarding parameter D, is appreciable. In addition, for each parameter I submitted the two groups to a nonparametric Mann-Whitney-Wilcoxon U-test with significance set at $p < 0.05$. All p-values obtained are $< O(10^{-5})$ (tables 5.5 and 5.6).

Table 5.5: Mean, standard deviation and p-value for the Stretched Exponential model parameters

	D	GAMMA
Healthy	0.05 ± 0.03	0.86 ± 0.11
60%	0.51 ± 0.04	1.04 ± 0.07
p-value	6.18E-08	3.65E-06

Table 5.6: Mean, standard deviation and p-value for the Mittag-Leffler model parameters

	D	GAMMA
Healthy	0.06 ± 0.04	0.93 ± 0.10
60%	0.53 ± 0.04	1.09 ± 0.06
p-value	6.44E-08	4.76E-06

5.4.2 Groups of healthy and 30%-demyelinated axons: results

A similar analysis was performed with healthy and 30% demyelinated samples. The aim is to determine whether the good indicators revealed by the previous analysis could provide a still earlier diagnosis. As could be expected, the parameters here fared overall worse. In the case of the stretched Exponential Gamma, in particular, the high p-value found in the nonparametric Mann-Whitney-Wilcoxon U-test does not allow us to exclude the

hypothesis of no correspondence between the parameter and the degree of myelination²² (value in red on table 5.8). In any case, for completeness, the results for all combinations are presented below.

Table 5.7: Results of the analysis Healthy x 30% demyelinated

Biomarker	Model	Sensitivity	Specificity	Accuracy
D	ML	0.95	1.00	0.98
	STR	0.95	1.00	0.98
GAMMA	ML	0.75	0.55	0.65
	STR	0.55	0.30	0.43
D + GAMMA	ML	0.85	1.00	0.93
	STR	0.65	1.00	0.83

Table 5.8: Mean, standard deviation and p-value for the Stretched Exponential model parameters

	D	GAMMA
Healthy	0.05 ± 0.03	0.86 ± 0.11
30%	0.22 ± 0.06	0.85 ± 0.07
p-value	7.30E-08	0.35

²² To be more rigorous, Mann-Whitney-Wilcoxon tests the null hypothesis that data in two groups are samples from continuous distributions with equal medians.

Table 5.9: Mean, standard deviation and p-value for the Mittag-Leffler model parameters

	D	GAMMA
Healthy	0.06 ± 0.04	0.93 ± 0.10
30%	0.26 ± 0.06	1.01 ± 0.08
p-value	9.44E-08	0.02

Again, the parameter D attains very high scores in the three indicators of diagnostic accuracy. It is interesting to note that the parameter D's obtained by the Mittag-Leffler model and by the Stretched Exponential model fared exactly equal. To a lesser extent, the combination (D, γ) also attained high indicators.

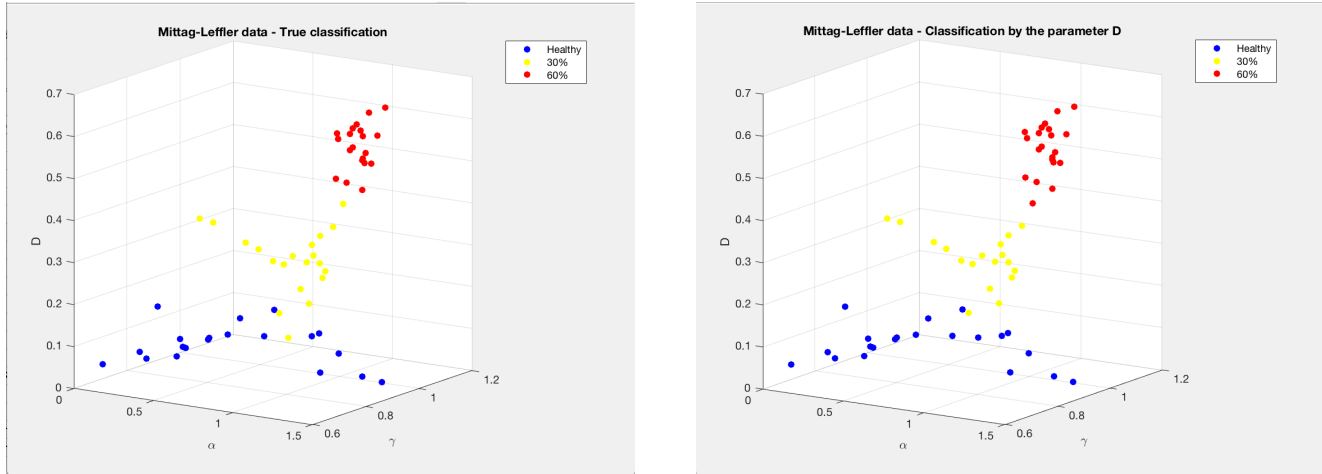
5.4.3 Conclusions and limitations

The results suggest that the parameter D obtained either from the Mittag-Leffler model or from the Stretched Exponential model can be used as a quantitative biomarker of the degree of myelination.

The parameter γ and the combination of parameters (D, γ) attained high indicators in all tests, particularly those concerning healthy x 60% demyelinated groups. The high p-values found for gamma in the comparison of healthy and 30% groups using the Stretched Exponential model, however, suggest that, at least for these groups, more thorough simulations/experiments are needed before we can ascertain the sensibility of the parameters (γ , (D, γ)). In any case, Gamma showed a good performance in the comparison between healthy and 60% groups, which means that the parameter can be a quantitative biomarker that is sensible to higher degrees of demyelination.

As a final illustration, I make reference to the two graphs below (figures 48a and 48b), where the Mittag-Leffler parameters are plotted. On the left the colors refer to the samples' true classification as to the degree of myelination; on the right the colors are based on the

classification by parameter D²³. The almost perfect match between the two images demonstrates qualitatively the parameter's potential to be a biomarker of demyelination.



Figures 48a and 48b: Comparison between true classification (48a, left) and classification by parameter D(48b, right)

The main limitation of the present study is the fact that the NMR signal was calculated only for the extra-axonal space. This presupposes that signal contribution from the extra-axonal and intra-axonal pools can be experimentally separable, an assumption which may not hold in practice. Another limitation lies on the natural uncertainty of some of the model parameters like the g-ratio or the axonal concentration. Small variations in these parameters could potentially alter the present results. A final (and certainly not the last) limitation is the small quantity of samples used.

²³ Note that the figure on the right was based on a classification using 3-clusters, here included for illustration purposes only. The results reported in this chapter use always two clusters (healthy/non-healthy) and are in fact even better.

Chapter 6

Conclusions

In this thesis, a Matlab program to simulate water diffusion inside arbitrary geometries and to calculate the corresponding signal acquired by nuclear magnetic resonance (NMR) was developed. The program includes as a special feature a routine for the computation of internal magnetic gradients due to differences of magnetic susceptibility between water and surrounding tissue. The execution of validation tests and comparison with experimental data showed that the program is able to simulate real physical systems. The program was used to simulate two kinds of systems: mono-dispersed spheres and white matter axonal tracts.

As far as the first group of simulations is concerned (mono-dispersed spheres), the results show that the anomaly of the space parameter (i.e., $\gamma < 1$) is in practice completely caused by internal gradients. These in turn are due to magnetic susceptibility differences between water and the surrounding media. This conclusion is in full agreement with the experimental evidence reported by the University of Rome NMR group (12).

A second conclusion is that the internal gradients also have the effect of increasing the spread in the values of gamma among the different configurations with equal packing, thus enabling us to better discriminate between different configurations.

A third conclusion was the confirmation of a finding by the University of Rome NMR group (25), namely, that the parameter regulating anomalous diffusion can identify structural disorder and structural transition in a heterogeneous system. A specific finding of the present study is that this ability is likely to be dependent on the scale of the medium.

A fourth conclusion, this one drawn from both groups of simulations, concerns the 'physicality' of the generalized diffusion coefficient (D) of either the Mittag-Leffler or the Stretched Exponential models. By 'physicality' I mean that all simulations have suggested that this coefficient conveys reliable information about the physical medium under study and, for that reason, it is readily comparable with the analogous mono-exponential diffusion coefficient. The results of chapter 5 represent an impressive evidence for the present conclusion.

A fifth, and final, conclusion is drawn from chapter 5. There I described a meticulously built model for a white matter tract, either healthy or subject to an arbitrary degree of demyelination. After running NMR simulations in samples created after that model and performing clustering analysis on the results, I concluded that there are grounds to believe that the the generalized diffusion coefficient (D) of either model (and, to a lesser extent, also the parameter Gamma) can be used as a biomarker for demyelination.

Bibliography

- (1) V. Méndez, D. Campos, F. Bartumeus, *Stochastic Foundations in Movement Ecology: Anomalous Diffusion, Front Propagation and Random Searches*, Springer-Verlag Berlin, Heidelberg, 2014.
- (2) R. Metzler, J. Klafter, *The Random Walk's Guide to Anomalous Diffusion: a Fractional Dynamics Approach*, Physics Reports 339, 1-77, 2000.
- (3) C. Ingo, R. Magin, L. Colon-Perez, W. Triplett, T. Mareci, *On Random Walks and Entropy in Diffusion-Weighted Magnetic Resonance Imaging Studies of Neural Tissue*, Magnetic Resonance in Medicine 71, 617–627, 2014.
- (4) S. Mori, J.-D. Tournier, *Introduction to Diffusion Tensor Imaging and Higher Order Models*, Elsevier, Oxford, second edition, 2014.
- (5) P. Callaghan, *Principles of Nuclear Magnetic Resonance Microscopy*, Clarendon Press, Oxford University Press, 1991.
- (6) E. L. Hahn, Spin Echoes, Physical Review 80, 4, 580-594, 1950.
- (7) H. Y. Carr, E. M. Purcell, Effects of Diffusion on Free Precession in Nuclear Magnetic Resonance Experiments, Physical Review 94, 3, 630-638, 1954.
- (8) E. O. Stejskal, J. E. Tanner, *Spin Diffusion Measurements: Spin Echoes in the Presence of a Time-Dependent Field Gradient*, The Journal of Chemical Physics 42,1, 288-292, 1965.
- (9) P. Callaghan, *Translational Dynamics & Magnetic Resonance: Principles of Pulsed Gradient Spin Echo NMR*, Clarendon Press, Oxford University Press, 2011.
- (10) W. S. Price, *NMR Studies of Translational Motion*, Cambridge University Press, 2009.
- (11) G. Genovese, *Simulations of molecular diffusion on heterogeneous systems to optimize nuclear magnetic resonance experiments in human tissues*, Master of Science in Physics thesis, University of Rome La Sapienza, Rome, 2016.
- (12) M. Palombo, A. Gabrielli, S. de Santis, C. Cametti, G. Ruocco, S. Capuani, *Spatio-temporal anomalous diffusion in heterogeneous media by nuclear magnetic resonance*, The Journal of Chemical Physics 135,3: 034504, 2011.
- (13) K. W. Desmond, E. R. Weeks, *Random close packing of disks and spheres in confined geometries*, American Physical Society, 76th Annual Meeting of the Southeastern Section of APS, 2009.

- (14) D. P. Bentz, E. J. Garboczi, *Percolation of phases in a three-dimensional cement paste microstructure model*, Cement and Concrete Research 21, 325-344, 1991.
- (15) L. Burtseva, B. Valdez Salas, F. Werner, V. Petranovskii, *Packing of monosized spheres in a cylindrical container: models and approaches*, Revista Mexicana de Física 61, 20-27, 2015.
- (16) M. P. Allen, D. J. Tildesley, *Computer Simulation of Liquids*, Clarendon Press, Oxford, 1991.
- (17) B. Balinov, B. Jönsson, P. Linse, O. Söderman, *The NMR self-diffusion method applied to restricted diffusion: simulation of echo attenuation from molecules in spheres and between planes*, Journal of Magnetic Resonance A 104, 17-25, 1993.
- (18) A. P. Pathak, B. D. Ward, K. M. Schmainda, *A novel technique for modeling susceptibility-based contrast mechanisms for arbitrary microvascular geometries: The finite perturber method*, NeuroImage 40, 1130-1143, 2008.
- (19) A. P. Pathak, B. D. Ward, A. G. Hudetz, K. M. Schmainda, *A novel technique for estimating the susceptibility-induced MR signal for arbitrary microvascular geometries: The Finite Perturber Method*, ISMRM, 10th Annual Mtg, 1331, Honolulu, 2002.
- (20) J. Langley, W. Liu, E. K. Jordan, J. A. Frank, Q. Zhao, *Quantification of SPIO Nanoparticles in vivo Using the Finite Perturber Method*, Magn. Reson. Med. 65-5, 1461-1469, 2011.
- (21) N. B. Semmineh, J. Xu, J. L. Boxerman, G. W. Delaney, P. W. Cleary, J. C. Gore, C. C. Quarles, *An Efficient Computational Approach to Characterize DSC-MRI Signals Arising from Three-Dimensional Heterogeneous Tissue Structures*, PLoS ONE 9(1): e84764. doi:10.1371/journal.pone.0084764, 2014.
- (22) I. Podlubny, *Mittag-Leffler function*, available online: <<https://www.mathworks.com/matlabcentral/fileexchange/8738-mittag-leffler-function?requestedDomain=true>>, accessed in October 2017.
- (23) D. S. Grebenkov, H. T. Nguyen, J.-R. Li, *A fast random walk algorithm for computing diffusion-weighted NMR signals in multi-scale porous media: A feasibility study for a Menger sponge*, Microporous and Mesoporous Materials 178, 56-59, 2013.
- (24) M. M. Karaman, Y. Sui, H. Wang, R. L. Magin, Y. Li, X. J. Zhou, *Differentiating Low- and High-Grade Pediatric Brain Tumors Using a Continuous-Time Random-Walk Diffusion Model at High b-Values*, Magnetic Resonance in Medicine 76(4), 1149-57, 2016.
- (25) M. Palombo, A. Gabrielli, V. D. P. Servedio, G. Ruocco, S. Capuani, *Structural disorder and anomalous diffusion in random packing of spheres*, Scientific Reports 3, 2631, 2013.

- (26) P. M. Matthews, F. Roncaroli, A. Waldman, M. P. Sormani, N. de Stefano, G. Giovannoni, R. Reynolds, *A practical review of the neuropathology and neuroimaging of multiple sclerosis*, Pract Neurol 16, 279-287, 2016.
- (27) M. S. Freedman (editor), *Multiple Sclerosis and Demyelinating Diseases*, Advances in Neurology, vol. 98, Lippincott Williams & Wilkins, Philadelphia, 2006.
- (28) M. S. Freedman, *Long-term follow-up of clinical trials of multiple sclerosis therapies*, Neurology 76(1), S26-S34, 2011.
- (29) M. Alhalabi, Corpus callosum Anomalies, available online: <https://www.slideshare.net/MarwanAlhalabi/corpus-callosum-anomalies-62947741?from_action=save>, accessed in January 2018.
- (30) F. Aboitz, A. B. Scheibel, R. S. Fisher, E. Zaidel, *Fiber composition of the human corpus callosum*, Brain Research 598, 143-153, 1992.
- (31) L. Cao, F. Y. Lu, Y. Lin, X. Wen, *Study on energy output efficiency of mild detonating fuse in cylinder tube structure*, Materials and Design 92, 690-700, 2016.
- (32) C. Nicholson, E. Syková, *Extracellular space structure revealed by diffusion analysis*, Trends Neurosci. 21, 207-215, 1998.
- (33) N. Stikov et al., *Quantitative analysis of the myelin g-ratio from electron microscopy images of the macaque corpus callosum*, Data Brief 4, 368-373, 2015.
- (34) N. Stikov et al., *In vivo histology of the myelin g-ratio with magnetic resonance imaging*, NeuroImage 118, 397-405, 2015.
- (35) C. Beaulieu, *The Basis of anisotropic water diffusion in the nervous system: a technical review*, NMR in Biomedicine 15, 435-455, 2002.
- (36) C. Liu, W. Li, K. A. Tong, K. W. Yeom, S. Kuzminski, *Susceptibility-Weighted Imaging and Quantitative Susceptibility Mapping in the Brain*, J Magn Reson Imaging 42(1), 23-41, 2015.
- (37) J. Lee, K. Shmueli, B.-T. Kang, B. Yao, M. Fukunaga, P. van Gelderen, S. Palumbo, F. Bosetti, A. C. Silva, J. H. Duyn, *The contribution of myelin to magnetic susceptibility-weighted contrasts in high-field MRI of the brain*, Neuroimage 59(4), 3967-3975, 2012.
- (38) W. C. Chen, S. Foxley, K. L. Miller, *Detecting microstructural properties of white matter based on compartmentalization of magnetic susceptibility*, Neuroimage 70, 1-9, 2013.

- (39) A.-M. Šimundić, *Measures of Diagnostic Accuracy: Basic Definitions*, EJIFCC 19(4), 203-211, 2009.